Radio Frequency Characterization of Superconductors for Particle Accelerators

DISSERTATION

zur Erlangung des Grades eines Doktors

der Naturwissenschaften

vorgelegt von

Dipl.-Phys. Raphael Kleindienst

eingereicht bei der Naturwissenschaftlich-Technischen Fakultät

der Universität Siegen

Siegen 2017

Gedruckt auf alterungsbeständigem holz- und säurefreiem Papier

Betreuer und erster Gutachter
Prof. Dr. Jens Knobloch
Universität Siegen

Zweiter Gutachter
Dr. habil. Claire Antoine
CEA Saclay

Tag der mündlichen Prüfung
28. September 2017

Abstract

Superconducting RF cavities are used in modern particle accelerators to supply large accelerating gradients to high current beams at moderate power requirements. The material used for these cavities is of key importance, as power consumption and maximum accelerating gradient are determined by the material properties surface resistance and critical RF-field.

Currently, bulk niobium is used as the cavity material of choice - compound superconductors such as Nb_3Sn, NbN and MgB_2 have greater theoretical potential however. Experiments to test the relevant superconducting material properties for small flat samples are in high demand by the community, as coating entire cavities is difficult and expensive. Furthermore being able to test the RF properties as a function of field, temperature, frequency and ambient magnetic field is important from a theoretical perspective.

Within this work, the design, production and commissioning of an optimized Quadrupole Resonator is presented. A detailed characterization is shown for two niobium samples, demonstrating the measurement capabilities of the setup. Measurements at higher RF fields than previously achieved in comparable experiments are used to test two non-linear models describing the field dependent surface resistance.

Zusammenfassung

Supraleitende Hohlraumresonatoren (auch Kavitäten genannt) werden in Hochstrom - Teilchenbeschleunigern eingesetzt, um hohe Beschleunigungsgradienten bei moderatem Energieverbrauch zu erzeugen. Das Material aus welchem diese Resonatoren hergestellt werden ist von entscheidender Bedeutung, da der Energiebedarf von dem Oberflächenwiderstand und die erreichbare Höchstspannung von dem kritischen Feld des Materials abhängt.

Derzeit werden supraleitende Hohlraumresonatren aus Niob hergestellt. Andere Supraleiter wie Nb_3Sn, NbN und MgB_2 haben von den supraleitenden Kenngrössen her ein höheres Potential, welches mit den derzeitigen Dünnschichttechniken noch nicht realisiert werden kann. Um diese Entwicklung zu Begleiten bietet sich eine Bestimmung der supraleitenden Hochfrequenzeigenschaften mittels kompakter Proben an, welche gegenüber der Messung mit Kavitäten den Vorteil besitzt, dass die Beschichtung weniger zeit- und kostenintensiv ist. Zudem eignet sich die Vermessung des Oberflächenwiderstandes als Funktion von Hochfrequenzfeld, Temperatur, Frequenz und statischem Magnetfeld, um verschiedene Verlustmodelle zu prüfen.

In dieser Arbeit werden die Planung, Herstellung und Inbetriebnahme eines Quadrupol Resonators vorgestellt. Es folgt eine umfangreiche Charakterisierung von zwei Niob Proben mit unterschiedlicher Oberflächenbehandlung. Das letzte Kapitel widmet sich dem feldabhängigen Oberflächenwiderstand, welcher bei hohen Feldstärken bis 110 mT gemessen werden konnte.

Acknowledgements

First I would like to thank Jens Knobloch for being a great advisor during my thesis, engaging in much discussion and for taking me up in a the great working environment of the SRF institute at Helmholtz-Zentrum-Berlin. Thank you also to Claire Antoine for agreeing to review this thesis and travelling to Siegen for the defense.

Great thanks to Oliver Kugeler for the supervision of this work, always giving guidance and help while keeping the day to day work enjoyable. Many hours were spent in the lab with Sebastian Keckert preparing and performing the measurements, thank you for that. Thanks also to Julia Köszegi for being such a good office mate throughout.

I would also like to thank the other physicists, current and former, of the SRF group, in particular Axel Neumann for advice on many aspects of simulating and testing SRF cavities as well Andrew Burrill for help with the cavity production and preparation. Thank you also to Adolfo Velez, Pablo Echevarria and Vasim Khan for many lunch breaks spent together in good spirits.

From the engineering team I would like to thank Sascha Klauke for helping with setting up the data acquisition - thanks to Michael Schuster for support from the vacuum group and to Jan Ullrich for help around the clean room. From the cyrogenic group I would like to thank Dirk Pflückhahn and Stefan Rotterdam.

Thanks also to the colleagues from CERN, Sarah Aull and Tobias Junginger, for sharing lots of information on the Quadrupole Resonator and letting me join in on a measurement campaign.

From Jefferson Laboratory, I would like to thank Tom Powers for performing the first RF test of the Quadrupole Resonator and Steve Castagnola for help and organization of the surface treatments.

This work was partly funded through EuCARD-2 under Capacities 7th Framework Programme, Grant Agreement 312453.

Contents

Chapter 1

Introduction

Particle accelerators are used to create high energy beams of charged particles, typically electrons or protons. They have many applications, ranging from fundamental physics experiments to cancer treatment to food preservation.

Within physics, the most famous accelerator is also the largest: the Large Hadron Collider. Built in a 27 km long tunnel on the CERN site near Geneva, it was used to collide protons with a center of mass energy of 7 TeV, leading to the discovery of the Higgs Boson in 2012 [1].

For a different class of experiments, one accelerates electrons without the intent to collide them with a target, but as a means of creating brilliant synchrotron radiation. Compared to x-ray tubes, the photon intensity achieved with synchrotron light sources is many orders of magnitude higher, the wavelength of the light is highly tunable and time resolved measurements are possible down to the femtosecond range. One of the largest accelerator projects currently being commissioned is the X-FEL, the European X-Ray Free Electron Laser. Electrons are first accelerated to 15 GeV with a 1.7 km long linear accelerator containing over 900 superconducting cavities. Coherent light in the X-ray regime is created in subsequent undulators of 100-200 m length, with an average brilliance of above $10^{25}\ \frac{\text{photons}}{\text{s}\cdot\text{mm}^2\cdot\text{mrad}^2}$, around 100 times higher than the previous record set by the SACLA Free Electron Laser [2]. The scale of these projects show that any improvement to the basic components of particle accelerators will have great effects on the feasibility and budget of these large endeavours.

Superconducting radiofrequency (SRF) cavities are geometrically optimized hollow chambers that can very efficiently create and sustain electric fields of several 10 MV/m. Compared to normal conducting copper cavities they have around six orders of magnitude lower surface losses at a typical operating of temperature of $T = 1.8$ K, which translates to around three orders less of required wall plug power. The losses in an SRF cavity are proportional to the surface resistance of the material. The surface resistance is composed

of a strongly temperature dependent contribution (the BCS surface resistance) and a temperature independent residual resistance.

Currently, superconducting cavities are made of bulk niobium. Alternative superconductors such as Nb_3Sn, NbN and MgB_2 have the potential of significantly reducing the surface losses and of maintaining higher RF fields. The lower surface resistance translates directly into a reduced power consumption during operation and large cost savings (in the order of many millions of euros for large scale projects) due to the smaller required cryoplant. Increasing the peak accelerating field allows one to reduce the overall size of the machine, again leading to a greatly reduced total cost. Much research concerning the deposition techniques and surface preparation methods of these composite superconductors is still required before these materials are expected to surpass bulk niobium. As coating entire cavities is difficult and expensive, experiments that can perform RF tests on flat samples are in high demand by the community.

Fundamental research on the loss mechanisms of superconductors exposed to an RF field also remain highly relevant. The dependency of the surface resistance on the applied electromagnetic RF field is not fully understood. The ability to measure the superconducting properties over a wide range of input parameters (temperature, RF field, frequency) is crucial in this respect. A deeper understanding of the residual resistance, currently considered to be dominated by trapped magnetic flux, is also desired.

Structure of the Thesis

In Chapter 2 an introduction is given on RF cavities, reviewing basic concepts and terminology. The concept of superconductivity is introduced with a focus on the surface impedance and critical fields. Towards the end of the chapter, the performance of state of the art niobium cavities is discussed and the potential improvement by alternative superconductors is shown. This leads directly into Chapter 3, in which different experiments for testing the superconducting properties (specifically the surface resistance) of flat samples are introduced. The measurement principle of a Quadrupole Resonator, pioneered at CERN, is explained and the comparative advantages of such a system are highlighted.

In Chapter 4, the RF design of the new Quadrupole Resonator built at Helmholtz-Zentrum-Berlin is presented. The modes and field of an ideal four-way transmission line are analyzed. Starting with the CERN Quadrupole Resonator as a baseline, the effect of changing the geometric parameters of the resonator on the relevant figures of merit are simulated. The final result of the geometric optimization is presented and compared to the baseline model.

Chapter 5 deals with the production of the Quadrupole Resonator (in itself a bulk niobium cavity). The mechanical model is presented, together with a discussion on the necessary mechanical tolerances. The second part of the chapter deals with the surface treatments which are required to ensure high fields and low losses in niobium cavities. The motivation behind the most important treatments are given. As these processes have been optimized mainly for elliptical cavities, the adaptations necessary for applying them to the Quadrupole Resonator are also discussed.

Chapter 6 details the experimental setup. The Quadrupole Resonator was the first cavity to be tested in a new helium bath cryostat constructed at HZB. The layout of the RF system and the phased-lock loop is shown, as is the thermometry system required for the surface resistance measurement.

The commissioning phase is subject of Chapter 7. It deals with all the issues needed to be dealt with before stable measurements at high fields were possible. The susceptibility of the Quadrupole Resonator to microphonics limited the measurement capabilities of the system during the first test runs. Furthermore, the field limiting mechanisms found most commonly in superconducting cavities - field emission, superconducting quench and multipacting, are introduced and their impact on the operation of the Quadrupole Resonator is discussed.

In Chapter 8, measurement results are presented for two niobium samples, made of material of the same nominal purity but with a different surface treatment history. Measuring the surface resistance as a function of temperature can be used to determine the superconducting energy gap and the electron mean free path of the material. The statistical method of bootstrapping is used to give confidence intervals for these parameters with some unexpected results. Penetration depth and critical fields measurements for both samples are shown, as is a measurement dealing with the losses caused by trapped magnetic flux.

Chapter 9 deals with field dependent surface resistance and shows the measurements acquired at high surface fields. The chapter starts with a discussion of the approximation error that occurs when the surface resistance is calculated from quality factor data using a constant geometry factor. It was found that this error can be substantial - up to 30% for cavities with an inhomogeneous magnetic field distribution. A method for eliminating this error is introduced and applied to simulated and measurement data. Two models predicting a field dependent surface resistance are then introduced and fit to measured data.

In the final Chapter 10, a summary of the main results given, together with ideas for future measurements.

Chapter 2

Superconducting Radiofrequency Cavities

In this chapter, the fundamentals of radiofrequency (RF) cavities and superconductivity will be introduced. Results from current state of the art niobium cavities will be shown and compared with the potential of some alternative superconductors.

2.1 Radiofrequency Cavities

As magnetic fields do no work on charged particles, strong electric fields are required for their acceleration. Older accelerator types such as the Van de Graaff generator create electrostatic fields that provide voltages of up to $5-10\,\mathrm{MV}$ typically [3]. The drawback with electrostatic accelerators, is that the voltage can only be used a single time for acceleration and that the accelerating gradient is discharge limited to around $3\,\mathrm{MV/m}$ in air. Modern high energy accelerators generally rely on time varying electromagnetic fields contained in RF cavities. These have the advantage that higher accelerating gradients are possible and that cavities can be used repeatedly for acceleration, as is done in an synchrotron.

2.1.1 Cavity Fundamentals

In this section, an overview of RF cavities is given together with discussion on some of the figures of merits which are used to compare them. A more detailed introduction with the mathematical derivations is found in [4].

RF Cavities are resonant structures, in which electromagnetic (EM) waves are continuously reflected by a highly conducting surface. If the input RF frequency matches one of the resonance frequencies of the cavity, one can achieve very high fields with moderate input power. The electromagnetic fields inside a cavity, can be calculated using the wave

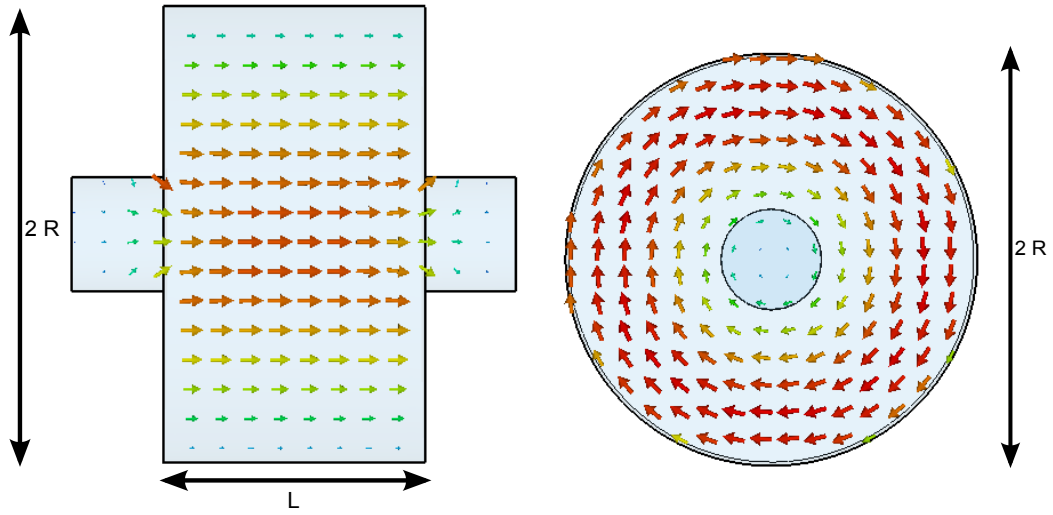

Figure 2.1: Electric and magnetic fields distribution of the TM010 mode for a simple pillbox cavity with beam tubes. On the beam axis, the electric field has its maximum, whereas the magnetic field vanishes, making it a useful mode for acceleration.

equation:

$$\nabla^2 - \frac{1}{c^2}\frac{\partial}{\partial t^2}\{\boldsymbol{E}, \boldsymbol{H}\} = 0 \tag{2.1}$$

where the solutions obtained in 2.1 have to fulfill the boundary conditions for highly conducting surfaces:

$$\hat{\boldsymbol{n}} \times \boldsymbol{E} = 0 \quad \text{and} \quad \hat{\boldsymbol{n}} \cdot \boldsymbol{H} = 0 \tag{2.2}$$

One can differentiate between two kinds of modes. For transverse electric (TE) modes, the electric field has no longitudinal component $E_Z = 0$. Conversely, transverse magnetic (TM) modes have $H_Z = 0$. As we require a longitudinal electric field to accelerate particles, we will consider only the TM modes henceforth.

Figure 2.1 shows the electric and magnetic fields for a simple pillbox cavity with beamtubes. Without beamtubes, analytical solutions to Equation 2.1 exist and allow us to calculate the resonance frequency and field pattern for all possible modes. To classify TM modes, one uses three indices m,n,p that refer to the number of half-wave patterns of E_Z in ϕ, ρ and z direction. The mode shown is the TM_{010} mode, as it is constant azimuthally and along the z-axis. The resonance frequency of the TM_{010} mode of a pillbox cavity is given by equation:

$$f_{010} = \frac{2.405 \cdot c}{2\pi R} \tag{2.3}$$

For a frequency of 1 GHz this comes out to a radius of around 11 cm. Optimized cavities with elliptical profiles have no analytical equation for calculating the resonance frequency, but Equation 2.3 can be used as a estimate.

To calculate the accelerating voltage of a cavity, one takes the line integral of of the electrical field across the cavity:

$$V_C = TT \cdot \int_0^L dz E_z \tag{2.4}$$

The voltage has to be corrected for by a transit time factor (TT) which takes into account that during the time the particle bunch takes to pass through the cavity, the phase of the fields will change and the maximum acceleration reduced. For a pillbox cavity, the transit time factor is $2/\pi$. To compare cavity performances, one normalizes the accelerating voltage by the cavity length L, defining the accelerating gradient $E_{acc} = {}^{V_C}/_{L}$.

2.1.2 Cavity Figures of Merit

Several figures of merit exist, which are commonly used to compare how suitable a cavity is for accelerating particles. The first one is the quality factor, which is an expression for how well a cavity stores electromagnetic energy:

$$Q_0 = \frac{\omega U}{P_{\text{Dis}}} \tag{2.5}$$

where $U = \frac{1}{2}\int_V \mu |H|^2 dV$ is the stored energy in the cavity, and P_{Dis} is the power dissipated in the cavity walls by the RF field. The dissipated power can be calculated with:

$$P_{\text{Dis}} = \frac{1}{2}\int_{\text{Surf}} R_S |H|^2 dA \tag{2.6}$$

where R_S is the surface resistance, the real part of the complex surface impedance.[1] The surface impedance Z_S describes the response of a metal to an applied EM field:

$$Z_S = R_S + iX_S = \frac{E_x(0)}{H_y(0)} \tag{2.7}$$

where it is assumed that the metal occupies the half-space $z > 0$. For a normal conducting metal, the surface impedance is given by:

$$Z_S = (1+i)\frac{1}{\sigma\delta} \tag{2.8}$$

[1] A detailed introduction to the surface impedance is given in Appendix A

where σ is the electrical conductivity and δ is the skin depth, given by:

$$\delta = \sqrt{\frac{2}{\mu_0 \omega \sigma}} \tag{2.9}$$

The skin depth is the decay length with which an RF field will penetrate into the conductor. Copper is the metal used for most normal conducting cavities, with a conductivity of $\sigma = 5.9 \cdot 10^7\,\mathrm{S/m}$. At a typical RF frequency of 1 GHz, this corresponds to a skin depth of $\sim 2\mu$m and a surface resistance (and reactance) of 8 mΩ.

Note that due to the expression for dissipated power, the quality factor has a term determined by the material and one determined by the geometry of the cavity. To separate these contributions a geometry factor G is introduced:

$$G = \frac{\mu_0 \omega \int_{Vol} |H|^2 dV}{\int_{\mathrm{Surf}} |H|^2 dA} = Q_0 \cdot R_S \tag{2.10}$$

For a pillbox cavity, the geometry factor is 257 Ω. The next figure of merit that is introduced is the shunt impedance, which relates the power dissipated in the cavity walls to the accelerating voltage:

$$R_{\mathrm{sh}} = \frac{V_C^2}{P_{\mathrm{Dis}}} \tag{2.11}$$

For efficiency reasons, one wants to maximize the shunt resistance. For comparing cavities with different geometries, one regularly normalizes the shunt impedance with the quality factor, with ${}^{R_{sh}}/_{Q_0}$ being independent of material and frequency. The dissipated power required to obtain a desired accelerating voltage V_{acc} can thus be calculated with:

$$P_{\mathrm{Dis}} = \frac{V_{acc}^2}{{}^{R_{\mathrm{sh}}}/_{Q_0} \cdot G} \cdot R_S \tag{2.12}$$

The last figures of merit introduced at this point are the field ratios ${}^{E_{\mathrm{pk}}}/_{E_{\mathrm{acc}}}$ and ${}^{B_{\mathrm{pk}}}/_{E_{\mathrm{acc}}}$, where E_{pk} and B_{pk} refer to the peak electric and magnetic field on the cavity walls. These terms are important, as the field levels attainable in a cavity can be limited by either field due to processes discussed in Section 7.2.

An overview over the cavity figures of merit is given for an ideal pillbox cavity and a standard TESLA cavity in Table 2.1. The TESLA cavity (TeV-Energy Superconducting Linear Accelerator [5]) refers to a commonly used cavity shape used in projects such as XFEL.

	Pillbox	TESLA
Geometry Factor	257 Ω	270 Ω
R/Q (per cell)	196 Ω	115 Ω
E_{pk}/E_{acc}	1.6	2.0
B_{pk}/E_{acc}	4.7 mT/(MV/m)	4.2 mT/(MV/m)

Table 2.1: Cavity figures of merit for an ideal pillbox cavity [4] and a TESLA cavity [5].

2.1.3 Normal and Superconducting Cavities

New accelerator projects face many choices concerning the RF cavity section. The biggest decision concerns the choice of whether to use normal or superconducting material. The choice has great implications as it leads to changes in the RF frequency and system, the necessity for a cryogenic plant as well as different auxiliary system.

The main difference between normal and superconducting cavities is the power dissipated in cavity walls due to the RF field. At 1 GHz, copper has a surface resistance of around 8 mΩ. This is compared to 10 nΩ, a typical value achieved in superconducting niobium cavities.

The six orders of magnitude that one gains in surface resistance, are offset in part by the Carnot efficiency, given by Equation 2.13. Modern superconducting systems are operated at $T_{\text{Cold}} = 2\,\text{K}$ and cooled by a cryoplant operating at $T_{\text{warm}} = 300\,\text{K}$, leading to a Carnot efficiency η of only 0.6%.

$$\eta = \frac{T_{Cold}}{T_{Warm} - T_{Cold}} \tag{2.13}$$

To the carnot efficiency one must furthermore multiply the techical efficiency of the refrigerator, which is typically around 20 – 30%. Due to this, static losses of superconducting cavities caused by heat conduction and radiation can be a major contribution to the required plug power.

Normal and superconducting cavities don't only differ in material but also in the typical size and shape. This is in part due to the different frequency scaling laws for normal- and superconducting surface resistance $R_{\text{S,NC}} \propto \sqrt{f}$ and $R_{\text{S,NC}} \propto f^2$. Normal conducting structures proposed for the high energy machines would be run at over 10 GHz [6]. At these high frequencies and thus small apertures, a very high accelerating gradient is possible, but the current is limited due to wakefields and alignment tolerances become very tight.

For superconducting cavities, a tradeoff between surface losses and cavity sizes has resulted in 1.3 GHz become the standard frequency, with a cell length of around 11 – 12 cm. Due to the larger aperture, less higher order modes are excited by the beam, allowing for

higher currents. A detailed discussion comparing normal and superconducting cavities is found in [7].

2.2 Superconductivity

In 1911, Kamerlingh Onnes discovered that the resistivity of mercury would vanish when immersed in liquid helium [8]. Since then, 52 further elements have been discovered with this property, which emerges below a material dependent critical temperature T_C [9]. Apart from the vanishing DC resistance, the most salient feature of superconductors is the expulsion of magnetic flux as the material is cooled through the superconducting transition. This is referred to as Meissner Effect and shown in Figure 2.2. The Meissner effect, together with the discontinuity of the heat capacity, show that the material undergoes a phase transition when cooled below T_C and that superconductors are different from perfect conductors.

Superconductivity today finds many applications. The commercially most advanced usage is in medical diagnostics, where Magnetic Resonance Imaging (MRI) systems use superconducting magnets to create fields of magnetic fields 1-2 Tesla. Emerging applications include high power transmission lines and magnetically levitated trains, which are already being tested in several countries [10].

For the remaining chapter, we will return to superconductivity within the context of RF cavities. Two models describing superconductivity will be introduced, with special attention being given to the surface impedance derived in either case. We will then turn our attention to the different critical fields, which limit the peak magnetic field up to which superconductivity is maintained field, determining the maximum achievable accelerating gradient.

2.2.1 Two-fluid model

An early phenomenological model of superconductivity is the two fluid model [11]. It postulates, that two types of charge carries exist, a normal conducting component with density n_N and a superconducting component with density n_S. The superconducting charge carriers move through the lattice without any friction and thus zero DC resistance, but on account of their mass, have inertia. The equation of motion for a superconducting electron of mass m and charge e in an RF electric field with angular frequency ω is:

$$\begin{aligned} m\frac{dv}{dt} &= -eE_0e^{i\omega t} \\ v &= i\frac{e}{m\omega}E_0e^{i\omega t} \end{aligned} \tag{2.14}$$

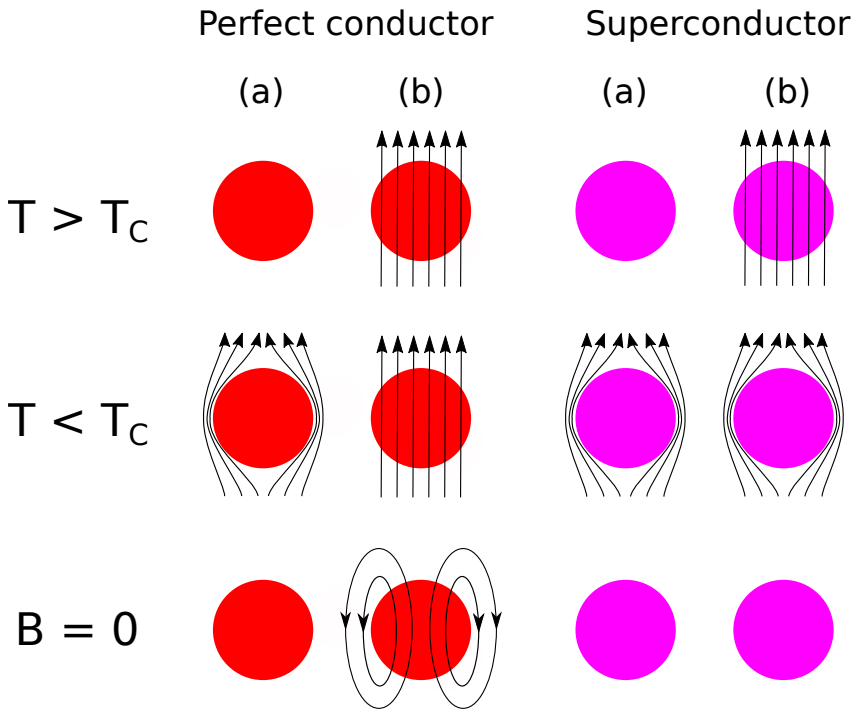

Figure 2.2: Contrast in magnetic flux expulsion between a hypothetical perfect conductor (for $T < T_C$) and a superconductor. Only the superconductor expels magnetic flux present before cooling through the transition temperature (case (b)).

We can calculate the current density J carried by n superconducting electrons to be:

$$J = n \cdot q \cdot v = i\frac{n_s e^2}{m\omega} E_0 e^{i\omega t} = i\sigma_S E \tag{2.15}$$

with the superconducting conductivity being defined as $\sigma_S = \frac{n_s e^2}{m\omega}$. The total conductivity of our superconductor is given by $\sigma = \sigma_N - i\sigma_S$. In this expression, $\sigma_N = \frac{n_N e^2 \tau}{m}$ is the normal conducting conductivity as derived from the Drude model, with τ being the mean free time between electron collisions. Substituting the modified σ into Equation 2.9, one arrives at:

$$\delta_S = \sqrt{\frac{2}{\mu_0\omega(\sigma_N - i\sigma_S)}} = \sqrt{\frac{1}{\mu_0\omega\sigma_S}}(1 + i\frac{\sigma_N}{2\sigma_S}) \tag{2.16}$$

where we assumed that $\sigma_S \gg \sigma_N$, which is justified for temperatures $T << T_C$. The decay length with which the RF field will penetrate into the superconductor is called the London penetration depth and is given by:

$$\lambda_L^2 = \frac{1}{\mu_0\omega\sigma_S} = \frac{m}{\mu_0 n_S e^2} \tag{2.17}$$

Note that λ_L is independent of frequency and is thus also the decay length for static fields. The value of λ_L is on the order of tens of nm for typical superconductors in contrast to several μm for the skin depth for typical normal conductors. From λ_L and the total conductivity σ, we can derive the surface impedance of our superconductor in the two fluid model to be:

$$Z_S = \frac{1}{2}\mu_0^2\omega^2\sigma_N\lambda_L^3 + i\mu_0\omega\lambda_L \tag{2.18}$$

The most important features of the two-fluid surface impedance are;

- The frequency dependence for superconductors is $R_S \propto \omega^2$, unlike the normal conducting case which was $R_S \propto \sqrt{\omega}$
- A higher normal conducting conductivity leads to an increased superconducting surface resistance. In our model this is explained by the normal conducting electrons carrying a larger proportion of the current.

So far, Equation 2.18 makes no statement of the temperature dependence of the surface impedance. The temperature dependence, as well as the microscopic description are hidden away in the density terms n_S and $n_N \propto \sigma_N$. Gorter and Casimir introduced a simple model [11, 12], which assumes $n = n_N + n_S$ and calculated the fractions of normal fluid and superfluid electrons by minimizing the combined free energy , resulting in:

$$\frac{n_N}{n} = \left(\frac{T}{T_C}\right)^4 \qquad , \qquad \frac{n_S}{n} = 1 - \left(\frac{T}{T_C}\right)^4 \tag{2.19}$$

The resulting temperature dependence of the surface resistance is thus:

$$R_S(T) \propto \frac{\left(\frac{T}{T_C}\right)^4}{\sqrt{1 - \left(\frac{T}{T_C}\right)^4}} \tag{2.20}$$

2.2.2 BCS Surface Impedance

The microscopic theory of superconductivity was first described by Bardeen, Cooper and Schrieffer in 1957 [13]. The theory derives from the insight that two electrons in a Fermi gas will form an energetically favourable bound state, if there is even an infinitesimally small attractive interaction between them. The two electrons in this bound state are referred to as Cooper pairs. The origin of the bound state is related to the ion lattice, which nicely fit the experimental data that critical temperature for different isotopes was found to scale with the mass number M as $T_C \propto 1/\sqrt{M}$. An intuitive model is shown in Figure 2.3. A first electron passes through the lattice, distorting it and creating the positive space charge density. A second electron passing through it's wake will now experience an attractive force by the deformed lattice. We can estimate the length scale of this attraction by the time scale of lattice distortion using the Debye frequency ω_D and the Fermi velocity v_F:

$$d = \frac{\tau}{4} \cdot v_F = \frac{\pi}{2\omega_D} \cdot v_F \tag{2.21}$$

Using the literature values for lead ($\omega_D = 2.8 \cdot 10^{13}$ rad/s and $v_F = 1.83 \cdot 10^6$ m/s), we arrive at an interaction distance of around 125 nm. The characteristic length describing the density variations of the superconducting state is called the coherence length, denoted by the symbol ξ, which for lead it is measured to around 100 nm [14].

Considering a single pair of electrons and their behaviour in an attractive potential is not enough however. The BCS wavefunction, which considers all electrons, is derived using the Hamiltonion in the second quantization and consists of a superposition of unoccupied and doubly occupied states (Cooper pairs). Due to the attractive potential, the energy of the occupied states at T=0 are all below the Fermi energy ϵ_F. Similar to the case in semiconductors, we find that there is a energy region in which no states exists. The superconducting energy gap Δ is a critical parameter in describing superconducting phenomenon, it's value at T=0 is given by Equation 2.22:

$$\frac{\Delta(0)}{k_B T_C} = 1.764 \tag{2.22}$$

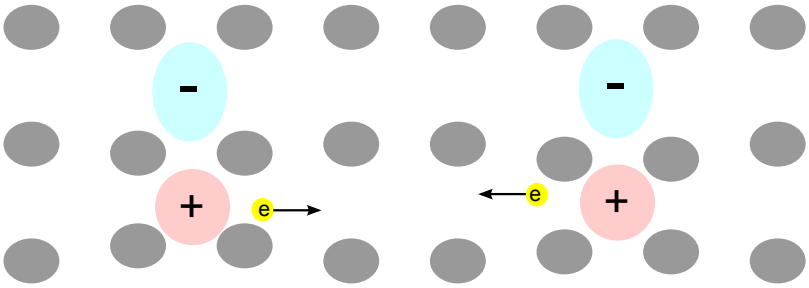

Figure 2.3: Two electrons with opposite momentum moving through the ion lattice. Due to the lattice distortion, a positive space charge is left in the electron wake, acting as an attractive potential on the second electron

As superconductivity breaks down at a critical temperature T_C, the energy gap goes to zero. The energy gap alone however is not enough to explain the ideal conductance of superconductors, as semiconductors also have a band gap. The difference comes from cooper pairs having spin 0, hence being bosons, and thus forming a macroscopic coherent quantum state. As a result, cooper pairs carrying current cannot scatter individually to lower, unoccupied energy states, which is the usual mechanism for dissipation in normal conductors.

From the BCS theory, an expression for the surface resistance of a moderately clean superconductor can be derived:

$$R_{BCS} \cong \frac{\mu_0^2 \omega^2 \lambda^3 \sigma_N \Delta}{k_B T} \ln\left(\frac{2.2 k_B T}{\hbar\omega}\right) \exp -\frac{\Delta}{k_B T} \tag{2.23}$$

One of the main differences of Equation 2.23 compared to the results derived from the two fluid model is the temperature dependence. Due to the energy gap, the amount of (normal conducting) electrons in the conduction band will be suppressed exponentially towards lower temperatures with $e^{-\frac{\Delta}{k_B T}}$.

Another important result is the dependency of the surface resistance on the electron mean free path. The effective penetration depth which goes into Equation 2.23 can be calculated with:

$$\lambda(l) = \lambda_L \sqrt{1 + \frac{\xi_0}{l}} \tag{2.24}$$

where λ_L and ξ_0 are the penetration depth and the coherence length in the clean limit and l is the electron mean free path. An effective coherence length can also be calculated by:

$$\frac{1}{\xi} = \frac{1}{\xi_0} + \frac{1}{l} \tag{2.25}$$

Returning to the expression for the BCS surface resistance, as the normal conducting conductivity scales as $\sigma_N \propto l$ one arrives at:

$$R_S \propto l \cdot \left(1 + \frac{\xi_0}{l}\right)^{3/2} \tag{2.26}$$

We can distinguish between the two extreme cases:

$$\begin{aligned} &\text{Clean limit}: \quad l >> \xi_0 \quad , \quad R_s \propto l \\ &\text{Dirty limit}: \quad l << \xi_0 \quad , \quad R_s \propto \frac{1}{\sqrt{l}} \end{aligned} \tag{2.27}$$

So far we have considered some limiting cases within the BCS theory. In general, the expressions for calculating the penetration depth or the surface resistance involve complicated integrals which need to be solved numerically. A numerical code used for these computation was developed by Halbritter in 1970 [15]. As input, it requires the critical temperature, penetration length, coherence length and mean free path. In Figure 2.4, the surface resistance of niobium is plotted as a function of mean free path for various frequencies. One sees that there is a shallow minimum in resistance for a mean free path which is of the order of the coherence length.

Both the BCS and the two-fluid surface impedance predict a vanishing surface resistance as $T \to 0$. Experimentally one always observes a temperature independent contribution to the surface resistance however, called the residual resistance. The surface resistance is thus given by:

$$R_S = R_{\mathrm{BCS}}(T) + R_{\mathrm{Res}} \tag{2.28}$$

Several mechanisms have been found to contribute to R_{Res}. Adsorbed gases, caused by insufficient evacuation of the cavity before cooldown was found to increase losses [16]. Impurities such as titanium and particulates on the cavity surface can also degrade cavity performance [17]. Furthermore, the presence of hydrogen induced by chemical polishing can cause large anomalous losses due to hydride formation [18].

Currently, for a well prepared niobium cavity, the residual resistance is dominated by the trapped magnetic flux contribution [19, 20], which will be the subject of Section 8.3.

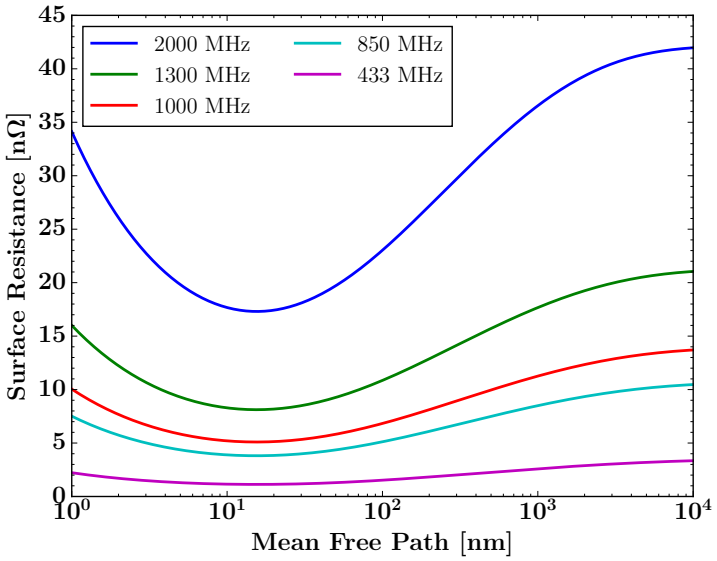

Figure 2.4: BCS Surface Resistance as a function of electron free path for Niobium at various frequencies. The minimum surface resistance is around $l \sim \xi_0/2$. Material parameters used are $\lambda_0 = 36\,\text{nm}$ and $\xi_0 = 39\,\text{nm}$ [21]

.

2.2.3 Critical Fields

In Section 2.2, the Meissner effect was already briefly introduced. The expulsion of magnetic flux below the transition temperature is a defining feature of superconductors.

As the expulsion of magnetic flux increases the free energy by $\mu_0 H^2/2$ per unit volume, the free energy density of the superconducting phase must be reduced for superconductivity to be energetically favourable. The difference in free energy density $f(T, H)$ between the superconducting (f_s) and the normal conducting state (f_n) can be related via the thermodynamic critical field, above which superconductivity breaks down:

$$\mu_0 \frac{H_C^2(T)}{2} = f_n(T, 0) - f_s(T, 0) \tag{2.29}$$

At the superconducting interface, one has the situation that magnetic field entering the superconductor decays with the characteristic length λ, whereas the superconducting density changes over the characteristic length ξ. The ratio of these two values $\kappa = \frac{\lambda}{\xi}$ determine whether or not it is favourable for a normal conducting - superconducting interface to form. One can differentiate between two types of superconductors which have qualitatively different magnetization curves as seen in Figure 2.5. Materials with $\kappa \leq 1/\sqrt{2}$ are named type

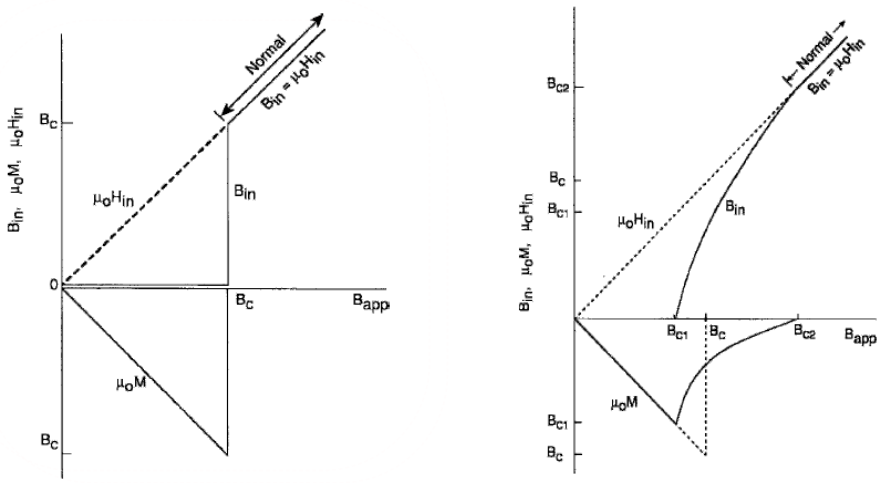

Figure 2.5: Internal magnetic field B_{in} and magnetization M as a function of applied field. For type I superconductors (left), all flux is expelled until H_C. For a type II superconductors (right), normal conducting vortices start penetrating the material above H_{C1}, above H_{C2} the material enters the normal conducting state. Diagram taken from [24].

I superconductors. Below H_C they exist in the Meissner phase, meaning that all magnetic flux is expelled from their bulk.

Type II superconductors with $\kappa > 1/\sqrt{2}$ have two critical fields. Below H_{C1} they are in the Meissner phase and behave just like type I superconductors. Between H_{C1} and H_{C2} however, they enter a mixed state, in which flux vortices enter the bulk of the material, forming a lattice of tubes each carrying a single quantum of flux $\Phi_0 = \frac{hc}{2e} \approx 2 \cdot 10^{-15}$ Wb [22]. Even though superconductors still carry a DC current without losses in this mixed state if the vortices are trapped by a pinning force, it is unsuitable for RF cavities, as the RF field will oscillate the vortices and lead to large amounts of normal conducting dissipation [23].

Is H_{C1} then the ultimate field limit for SRF cavities? Experimentally, the answer is 'no', as niobium cavities have supported peak magnetic fields of around 200 mT without vortex penetration, well above the value for $\mu_0 H_{C1} = 180$ mT [25, 26]. The theoretical explanation of this was provided by Bean and Livingstone in 1964 [27]. Higher fields than H_{C1} can be supported, as an energy barrier prevents flux tubes from entering the superconductor, even though it would be energetically favourable in the bulk. The energy barrier is created by an image vortex outside the superconductor which acts as an attractive force towards the entering vortex. This dependency of the vortex energy on the position inside the superconductor is shown in Figure 2.6. The field level at which this energy barrier is overcome is called the superheating field H_{SH} and is believed to be the fundamental field limit for RF cavities.

The thermodynamical critical field, defined by Equation 2.29, can be calculated using the characteristic lengths λ and ξ:

$$H_C = \frac{\phi_0}{\sqrt{8}\pi\mu_0\lambda\xi} \tag{2.30}$$

Calculating the superheating field is only possible numerically, within the Ginzburg-Landau theory it can be approximated as [28]:

$$H_{sh} = H_C\left(0.64 + \frac{0.54}{\sqrt{\kappa}}\right) \tag{2.31}$$

Calculating H_{C1} analytically is only possible for type II superconductors ($\kappa \gg 1$):

$$H_{C1} = \frac{\phi_0}{4\pi\lambda^2}\ln\kappa + 0.5 \tag{2.32}$$

2.3 Performance of SRF cavities

After decades of research, SRF cavities made from bulk niobium can today consistently achieve quality factors of several 10^{10} at gradients above 30 MV/m. In this chapter, some of the recent bulk niobium results are shown. Alternative superconductors with the potential for significant improvement beyond niobium are introduced as is the concept of superconducting thin films.

2.3.1 State of the art Niobium

Currently, all larger projects under construction that rely on SRF cavities use bulk niobium. The base material used for cavities is high purity niobium sheets, which have been extracted from the niobium ore in a complex procedure involving several steps of electron beam melting, polishing, rolling and annealing. These niobium sheets form half cells by the process of deep drawing, after which they are electron beam welded together to form entire cavities. A good overview over niobium preparation and cavity production is given in [29].

After production, a series of surface treatments is necessary to achieve a high performing cavity. The top $100 - 200\,\mu$m of the material has to be removed due to damages during the sheet rolling by chemical etching. A high temperature bake is typically applied to degas hydrogen and the cavity has to be rinsed to remove particulates from the surface. These steps will be discussed in more detail in Section 5.3, when we will focus on the surface treatments for the Quadrupole Resonator. For larger projects with a high number of cavities, detailed procedures are defined for the cavity preparation [30].

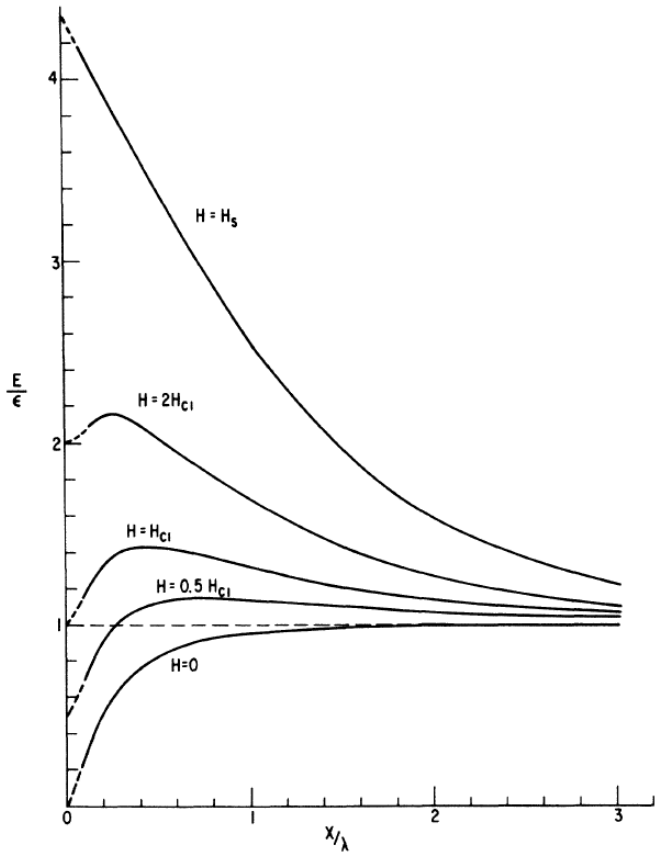

Figure 2.6: Vortex energy depending on its distance from the surface. The case shown is for a type II superconductor with Ginzburg-Landau parameter $\kappa = \frac{\lambda}{\xi} = 10$. The energy E of the vortex is normalized to the energy gap ϵ, the depth x is given as multiples of the penetration depth λ. Note that for a vortex far inside the bulk, an energy barrier exists for leaving the superconductor, at any field $H > 0$. Plot taken from [27]

Cavity performances are typically compared by plotting the quality factor against the accelerating gradient. For bulk niobium cavities following the standard treatments, a plot is shown in Figure 2.7 on the left.

Very interesting results have recently been presented for bulk niobium cavities purposefully contaminated with nitrogen or titanium [31, 32]. In these so called doped cavities, one observes that the quality factor at low fields is increased and rises further up to gradients of around 10 MV/m. While the baseline increase can be explained with a reduced mean free path leading towards the BCS surface resistance optimum as shown in Figure 2.4, the cause of the field dependence is still being debated [33].

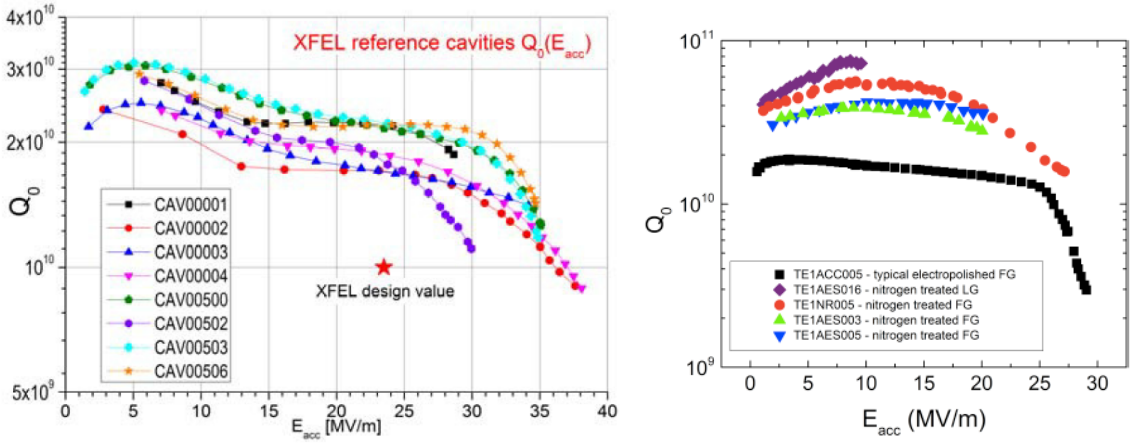

Figure 2.7: Left: Eight cavities treated with standard ILC-treatment for XFEL [34]. Right: Three nitrogen doped cavities compared to standard treatment [31].

2.3.2 Superconducting Thin films

As discussed in Section 2.2.1, an RF field will decay over a characteristic length of λ_L in a superconductor. The RF properties of a superconductor are thus completely determined by the outer layer of thickness $\sim 10\lambda_L$, opening the possibility of growing a superconducting thin film onto a different bulk material. As an example, coating niobium onto a copper cavity has several advantages:

- The thermal conductivity of (high purity) Copper is several orders of magnitude better than niobium at cryogenic temperatures. This may prevent heating from a local defect from quenching the entire cavity.
- The cost for the raw material is much lower for copper

The largest application of niobium copper cavities was for the Large Electron Positron (LEP) upgrade at CERN, finished in 1996 [35, 36]. A total of 176 cavities working at an RF frequency of 352 MHz were added to the already existing normal conducting system. The performance required and achieved by these cavities, a quality factor of over $3 \cdot 10^9$ at an accelerating gradient of 6 MV/m and 4.5 K, is still a benchmark for Nb coated cavities which has not been consistently surpassed up to date.

A further aspect making thin films interest is the potential to increase the ultimate accelerating gradient. It was shown by Abrikosov in 1964, that for a type II superconductor with a thickness $d \ll \lambda$, the first critical field is given by:

$$H_{C1} = \frac{2\phi}{\pi d^2} \ln \frac{d}{\xi} \tag{2.33}$$

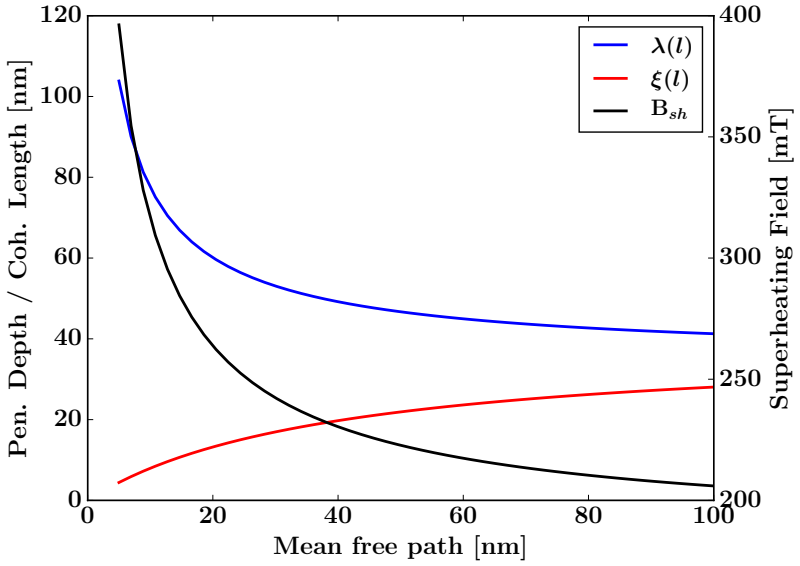

Figure 2.8: Penetration depth, Coherence length and superheating field as a function of electron mean free path for Niobium

This property lead to the proposal to coat cavities with multiple layers of thin superconducting films separated by insulating layers [37].

2.3.3 Alternative Superconductors

Even though niobium is the material of choice for superconducting RF cavities today, other superconductors have the potential for offering better performing cavities. Improvements are possible in both a lower surface resistance and a higher critical field.

Reviewing Equation 2.23, we see that a high normal state resistivity yields a lower BCS surface resistance. Furthermore a large energy gap lowers the fraction of unpaired electrons, pointing towards superconductors with a high T_C, which is also a good property for cryogenic efficiency.

For high fields, a theoretical prediction of how different materials performs is more complicated. First, one cannot be sure whether H_{C1} or H_{sh} is the relevant critical field as one would have to predict whether vortices can enter the bulk prematurely at defects or dislocations. We will assume that the superheating field is the limiting factor. Secondly, as the critical fields are determined by the effective penetration depth and coherence length of a superconductor, the impurity content, determining the mean free path l of the electrons, needs to be included in the calculations. This is shown for the example of Niobium in Figure 2.8.

In Table 2.2, the critical temperature, normal conducting resisitivty, as well as the penetration depth and coherence length in the clean limit are shown for some relevant superconductors. The superheating field is also shown, calculated from Equation 2.31 under the assumption that $l = \xi_0$, which optimizes BCS resistance.

We see, that several superconductors exist with critical temperatures above 15 K which makes efficient cavity operation at 4.2 K a possibility. Nb_3Sn and MgB_2 also appear to have a very high superheating field, making then good candidates for high gradient cavities. High superheating fields are however also possible with NbN or NbTiN fils with a low mean free path.

MgB_2 is the superconductor with the by far highest critical temperature of 39 K. The high critical temperature also suggest a large energy gap, measurements have however shown two distinct superconducting gaps at 2 and 7 meV. This means that MgB_2 is not naturally treated within the BCS framework, making it difficult to compare with the other materials on superconducting parameters alone and calling into question the calculated superheating field.

Summarising, one has several different candidate superconductors with the potential to surpass Niobium when it comes to SRF cavity performance. In Figure 2.9, the power required to operate a 9-cell TESLA cavity at 30 MV/m is shown. The surface resistance for each material was computed with the Halbritter code, using the material data from Table 2.2, assuming $l = \xi_0$ and a residual resistance $R_{Res} = 10\,\text{n}\Omega$. Note that the wall-plug power at 300 K is shown, the Carnot efficiency is thus included in the plot. Not included is the technical efficiency of the cryoplant, which increases with temperature, making alternate materials even more favourable in this aspect. A significant improvement can thus be achieved with respect to power consumption, which leads to massive decrease of the cost of cryogenic infrastructure for large scale projects.

As bulk cavities out of the composite superconductor are not viable, thin film coatings on copper or niobium cavities are the best option. These however need to fulfill many requirements:

- The correct superconducting phase has to be achieved across the entire surface. Small normal conducting inclusions can cause local heating and premature quench.
- The thermal conductivity has to be good enough for the film to not warm up significantly due to RF heating.
- The superconducting film has to be mechanically stable and and not peel off during cooldown or during the surface finishing treatments required to obtain a clean surface

Material	T_C [K]	ρ_N [$\mu\Omega$cm]	λ_L [nm]	ξ_0 [nm]	$\mu_0 H_{SH}$ [mT]
Pb	7.2	3	31.2	96	133
Nb	9.2	2	36	39	225
NbN	16	70	38	35	232
NbTiN	15.8	35	180	5	304
Nb_3Sn	18	20	89	7	431
MgB_2	39	0.1	40	7	1013

Table 2.2: Comparison of the the material properties for several candidate materials for superconducting RF cavities. Material data taken from [40, 41, 14, 21, 42, 43]

- The secondary emission yield should be low (ideally under 1) to avoid multipacting (see Section 7.2.3).
- The residual resistance of the film needs to be comparable to the achieved value of bulk niobium cavities, currently around $5 - 10\,\mathrm{n}\Omega$, as not to offset any gains in BCS surface resistance.

Significant effort has been made for Nb_3Sn, NbN and MgB2 films, producing homogeneous films at the correct critical temperature. RF test have shown however, that these films often suffer from a very high residual resistance. The only films produced with a suitably low R_{Res} has been Nb_3Sn , created by Tin diffusion into bulk niobium [38, 39]. Quality factors of several 10^{10} were reached up to gradients of up to $15\,\mathrm{MV/m}$, making Nb_3Sn almost competitive already with bulk niobium cavities. Lots of potential upside is however still achievable in all materials presented and is thus subject of intense research.

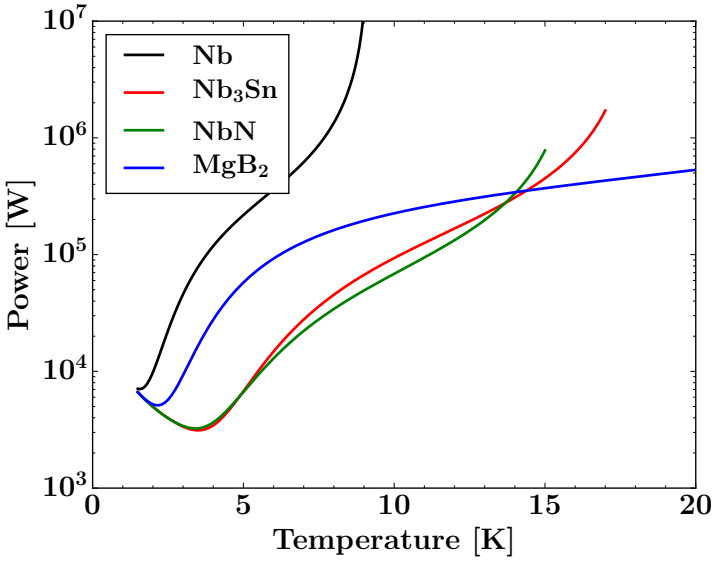

Figure 2.9: Plug power required to run a 9-cell TESLA cavity at 30 MV/m. Surface resistance calculated with the material property from Table 2.2 with $l = \xi_0$ and $R_{Res} = 10\,\mathrm{n\Omega}$. The Carnot efficiency is included into the calculation. On account of the residual resistance, the optimum operating temperature is $T > 0$.

Chapter 3

Characterization of Superconducting Samples

In Chapter 2 we saw that new materials beyond niobium have great theoretical potential for SRF cavities. Thin film deposition techniques for composite superconductors are being tested with encouraging results [44, 45, 39]. As a first step, small flat samples with a diameter of 2 – 3 cm are typically coated and subsequently characterized with respect to their chemical composition and crystallography using techniques such as X-ray spectroscopy and electron microscopy. An RF test at the operating frequency is always required however, if one wants to make statements concerning the suitability of a material for SRF cavities. Testing the RF properties of samples is an ideal intermediate step before coating entire cavities, as it is easier to coat flat surfaces than curved ones. Reduced cost and faster turn over rates are further benefits.

Significant effort has been made by various laboratories to mount experiments which can measure the surface resistance and other relevant properties of superconducting samples. Before introducing some of these setups, it is a good idea to envision the ideal properties such an experiment could have:

- Surface resistance measurements over a wide parameter space: Understanding and testing the theory behind the RF losses of superconductors requires the possibility of varying the input parameter (temperature, frequency, RF field) over a wide range. Cavity tests are limited in this respect, as they are typically performed at temperature below 4.2 K and at a single frequency.

- Small samples: This is particularly important for testing superconducting thin films, as many experimental deposition chambers will only fit small samples. Reduced cost is a further obvious advantage. Apart from the sample size, practical aspects such

as how quickly the sample and it's diagnostics can be mounted and demounted are important in determining the turn around rate of the experiment.

- Control over cooling conditions: Ambient magnetic flux, present during the superconducting conditions, can cause additional RF losses in superconductors. Cooling conditions (temperature gradient and cooling rate) can affect cavity performance and are thus an important subject of inquiry. Another aspect of the cooling dynamics is the diffusion and agglomeration of hydrogen, which can influence the RF surface resistance of a superconductor.

- Further measurements: Other properties of the sample apart from the surface resistance are also of interesting from a SRF cavity perspective. These include thermal conductivity, penetration depth, critical field, transition temperature and residual resistivity ratio (RRR).

As we shall see, there are certain trade-offs when it comes to SRF sample testing experiments. Different laboratories around the world have put together different systems, some of which will be introduced and compared in the following sections.

3.1 TE host cavities

One of the first ideas for testing flat samples, was using a pillbox-like cavity with a demountable end plate as a sample. This approach has gone through several iterations - currently at Cornell, a third generation TE host cavity (the mode used is the TE_{011}) has been commissioned. At 4 GHz, it can apply over 100 mT onto a flat sample of 12.7 cm diameter[46, 47]. A photograph and some of the achieved results are shown in Figure 3.1.

The surface resistance of the sample can be measured by an RF power measurement. Alternatively, the thermometry system on the back side of the sample can be used to measure the local losses. The thermometry system is also useful to locate hot spots and other areas which are potentially interesting for further local measurements.

The advantage of this system are the high fields achievable on the sample and the locally resolved information provided by the thermometry system. The frequency of 4 GHz limits this experiments capabilities of measuring the residual resistance, as the losses will be BCS dominated.

A similar system is also being used at Saclay/Orsay. The sample diameter and frequency are very similar to the Cornell system with 3.88 GHz and 13 cm [48].

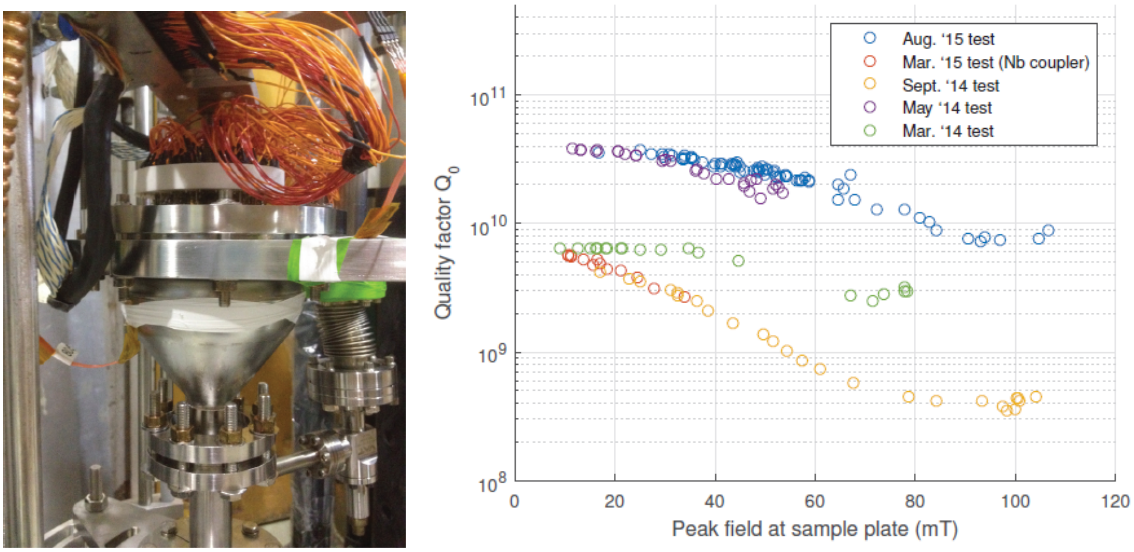

Figure 3.1: Photo and results of the TE host cavity at Cornell [46, 47]. The surface resistance of the sample can be measured in an integral RF measurement. The thermometry system, mounted to the backside of the sample (orange cables), can be used to detect local hot spots. Peak fields of over 100 mT have been reached with this setup

3.2 Sapphire Loaded Cavity

At JLab, a sapphire loaded cavity has been used to characterize 5 cm samples at 7.5 GHz [49, 50]. The sample is mounted on a copper support plate as shown in Figure 3.2 and is thermally decoupled from the rest of the cavity, allowing measurements within the temperature range between 2 and 20 K. Two choke filters prevent the TE_{011} operating mode from leaking out of the cavity. The cavity is loaded with a sapphire rod to decrease the resonance frequency and provides a method of tuning the cavity by adjusting the distance between rod and sample. Losses are measured by calorimetry rather than RF power.

An advantage of this system, is that the sample is directly bonded to its copper support, providing a good thermal contact to the calorimetry system. Furthermore by altering the material of the support structure, the sensitivity of the calorimetry system can be tuned, depending on the expected surface resistance of the sample. Due to the thermally isolated sample, measuring the penetration depth is possible by heating up the sample and measuring the change in resonance frequency.

The disadvantages of this system are once again the high frequency of 7.5 GHz and that fields are limited to values below 20 mT in the publications so far.

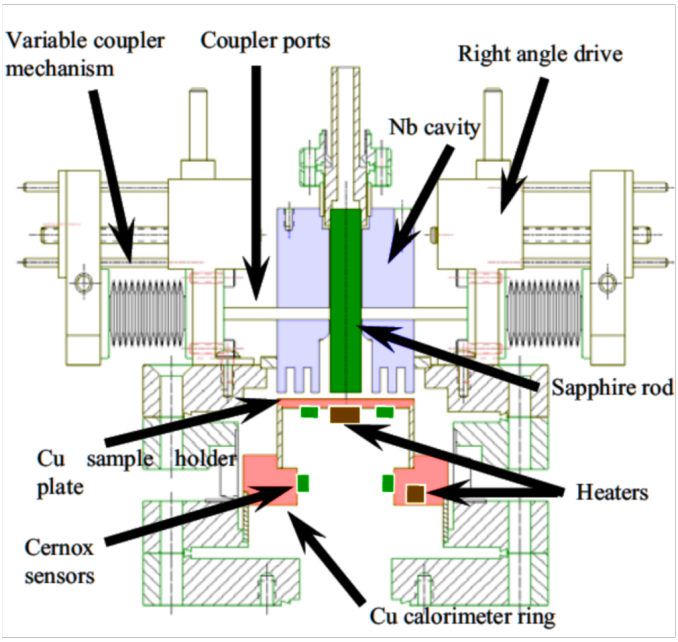

Figure 3.2: Schematic overview of the sapphire loaded cavity at Jefferson Lab [49, 50]

3.3 Hemispherical cavity

At SLAC, two hemispherical cavities, made from copper and niobium, are being used to test flat samples with a diameter of 50.8 mm [51, 52]. A cross section view and some results are shown in Figure 3.3. In this setup, a TE032 mode at 11.4 GHz is excited, which has very high magnetic field on the sample surface, but no electrical field. The peak magnetic field is 2.5 times higher on the sample than on the hemispherical cavity and RF losses on the sample account for 33% of the entire losses, given the same surface resistance.

The surface resistance of the sample is determined by measuring the quality factor of the cavity/sample system and calculating the losses due to the sample by the simulated geometry factor of the sample. With the copper cavity, one is limited in the ability to measure the surface resistance of a superconducting sample, but one can efficiently measure the critical field, by observing at what applied field the Q-curve drops. As copper has no critical field, up to 300 mT of field can be applied to the sample.

In general, this experiment has the advantage that it does not need to be immersed in liquid helium, cooling is provided by a commercially available pulse-tube refrigerator. Turn around time is very fast, with one test cycle being possible in a single day. The main disadvantage of the system is the very high frequency of the system, which makes

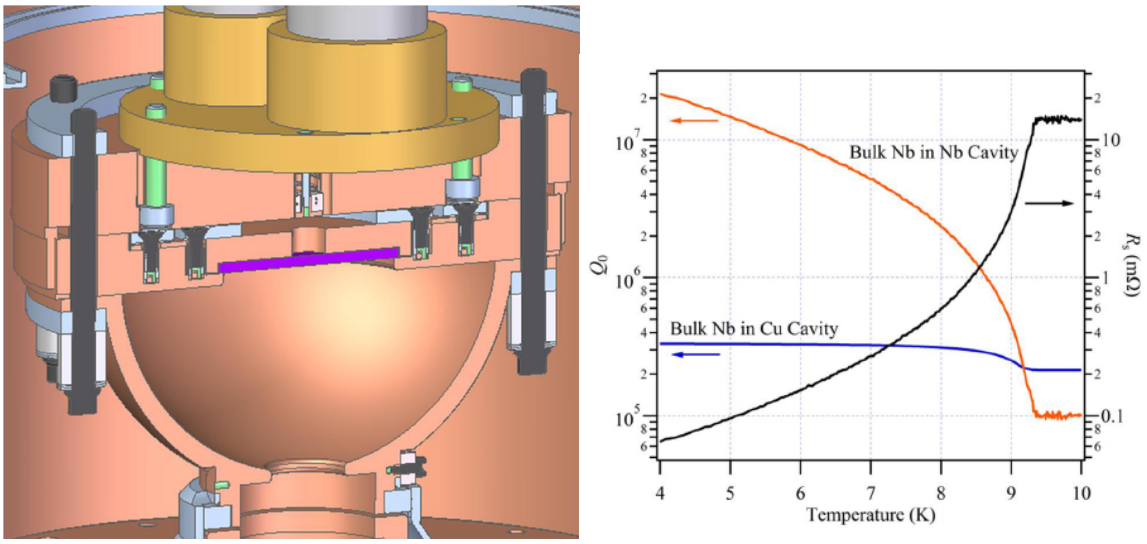

Figure 3.3: Left: Overview of the hemispherical cavity. The RF power is fed into the cavity from the bottom, the sample disk (purple) is held in place by mounting plates clamping it into position. Right: Quality factor of the niobium cavity (orange) and copper cavity (blue), both using a bulk niobium sample. The black line shows the surface resistance of the sample, measured with the niobium cavity.

it impossible to measure the residual resistance of samples, and the comparatively high temperature limit of the refrigerator at 3.6 K.

3.4 Quadrupole Resonator

The Quadrupole Resonator (QPR) was developed at CERN in the late 1990's [53]. Since its upgrade, it can be used to characterize a superconducting sample at 400, 800 and 1200 MHz [54]. Measurements are possible over a wide temperature range with peak magnetic fields reaching up to 60 mT on the 7.5 cm sample. A photo and a representative result is shown in Figure 3.4.

As the core chapters of this thesis consist of the work on a modified Quadrupole Resonator, the main design features and the measurement principle will be introduced in more detail in the subsequent sections.

3.4.1 Design Principle

A cross sectional view of the Quadrupole Resonator is shown in Figure 3.5. Welded to the top-plate of the niobium pillbox-like cavity are four hollow niobium rods, shortened to two current loops a short distance over the sample surface (red). The operational quadrupole

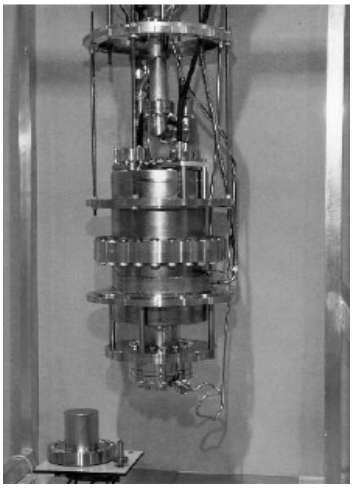

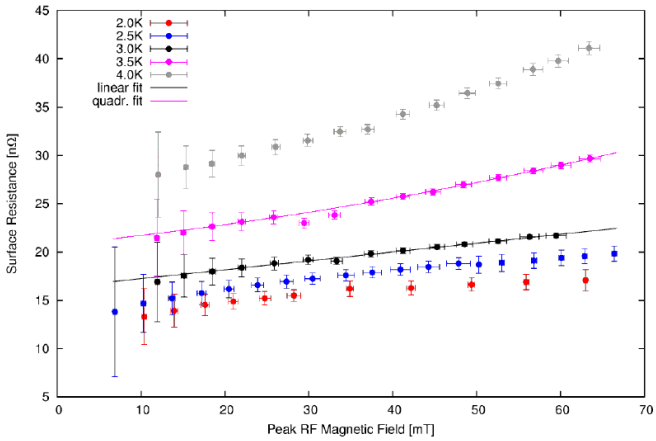

Figure 3.4: Left: Photograph of the CERN Quadrupole Resonator. Right: Surface resistance of a reactor grade niobium sample measured against field for various temperatures [55].

mode is contained around the rods, with the result that the resonance frequency is not determined by the radius of the cavity, but by the length of the current loop. An approximation for the resonance frequency of the fundamental mode is $f \approx \frac{c}{2 \cdot L_{rods}}$.

The connection between the sample and the superconducting resonator is an experimental liability, as it necessarily involves normal conducting components, copper gaskets and stainless steel flanges in this case. Surface magnetic fields need to thus be minimal in these regions. For this purpose, the sample top is welded to a niobium cut off tube which is separated from the resonator by a narrow coaxial gap and strongly attenuates the RF fields of the dipole and quadrupole modes at the critical normal conducting joints. One uses the quadrupole modes for operation, as they have double the cutoff frequency in the coaxial gap and thus a better field attenuation. This issue is discussed in detail ins Section B.3.2. The coaxial gap also decouples sample and resonator thermally. This allows changing the sample temperature freely while keeping the rest of the resonator at the temperature of the helium bath, typically 1.8 K.

The sample disc has a diameter of 75 mm. Threads on the lower side allow mounting a heater and temperature sensors, required for regulating the sample temperature and measuring the RF losses. The sample disc is welded to the niobium tube and then brazed to a double sided stainless steel flange, which isolates the resonator from the outside. Changing the sample thus requires two steps of electron beam welding which, apart from being time consuming and expensive, adds the risk of damaging the superconducting surface.

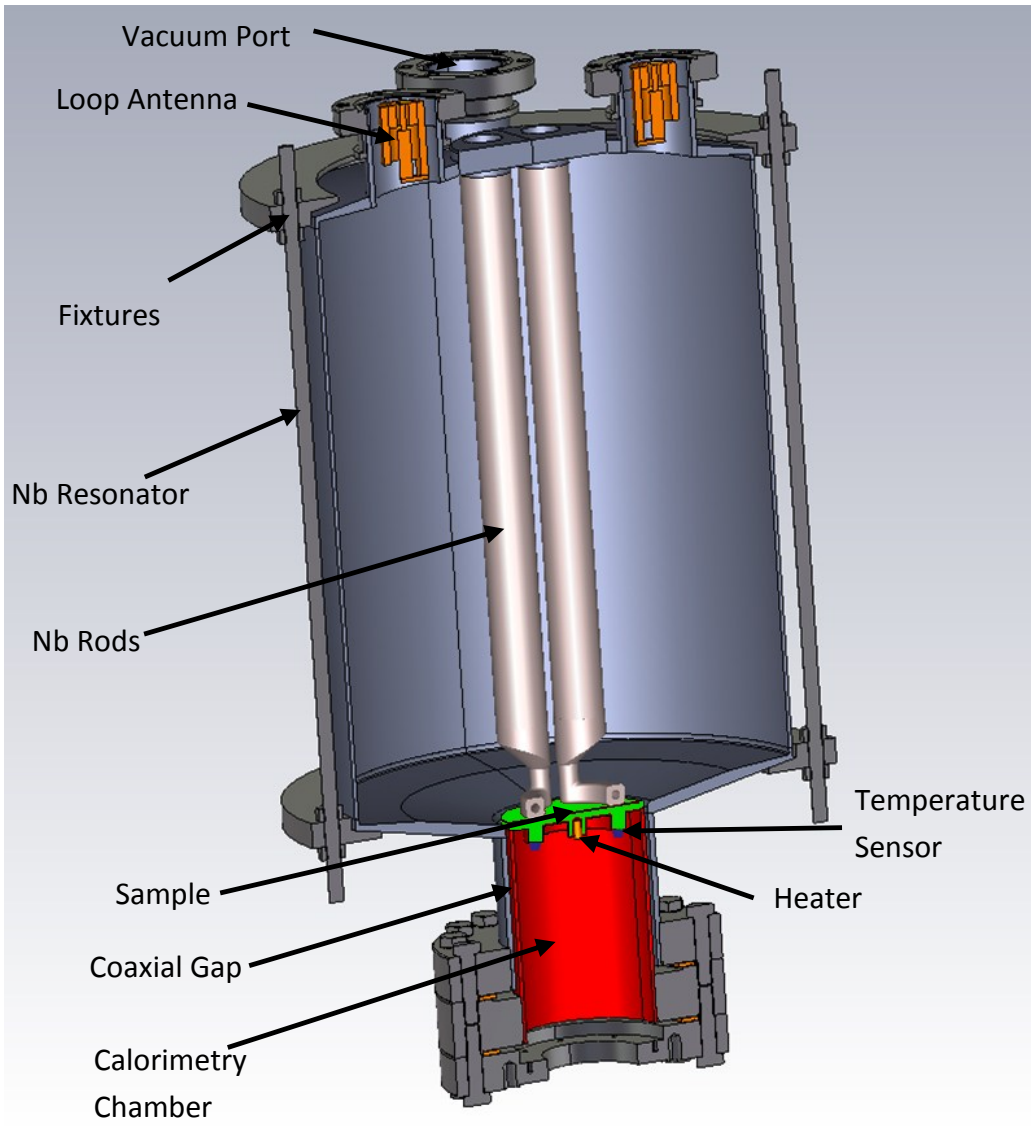

Figure 3.5: Schematic of the QPR. Not included in the diagram are the solenoid and the magnetometer within the thermometry chamber

3.4.2 Calorimetric Measurement Principle

The QPR uses a compensation method to measure the surface resistance of a sample. In a first step, the sample is heated to a desired temperature using a resistive heater operated in a feedback loop with a temperature controller. The necessary heater power P_{DC1} that is required for temperature stabilization is recorded. In the second step, the RF is switched on, resulting in an increased heat load on the sample surface. The temperature controller will decrease the heater power until again steady state conditions have been reached at P_{DC2}. From the difference between the power required to obtain a constant temperature with and

without RF, one can calculate the RF power dissipated in the sample:

$$P_{\mathrm{RF}} = (P_{\mathrm{DC1}} - P_{\mathrm{DC2}}) = \frac{1}{2}\int_{\mathrm{Smpl}} R_S \|H\|^2 dS \tag{3.1}$$

The measurement principle is further illustrated in Figure 3.6. Assuming a constant surface resistance over the sample area, the surface resistance can be calculated by:

$$R_S \approx \frac{2(P_{\mathrm{DC1}} - P_{\mathrm{DC2}})}{\int_{\mathrm{Smpl}} |H|^2 dS} \tag{3.2}$$

where the integral term in the denominator can be expressed as $c \cdot U$, a product of a simulation constant c and the stored energy in the cavity. The stored energy is measured using a weakly coupled field probe, described by:

$$Q_{\mathrm{FP}} = \frac{\omega U}{P_T} \tag{3.3}$$

where P_T is the transmitted power and Q_{FP} is the quality factor of the field probe. The field calibration will be discussed further in Section 6.2.1.

This rather straightforward measurement technique allows us to measure the surface resistance with a sub nΩ and a significantly higher precision compared to RF power measurements. Other superconducting properties, such as critical field, penetration depth and trapped flux sensitivity, can also be studied with the QPR, discussed in Chapter 8.

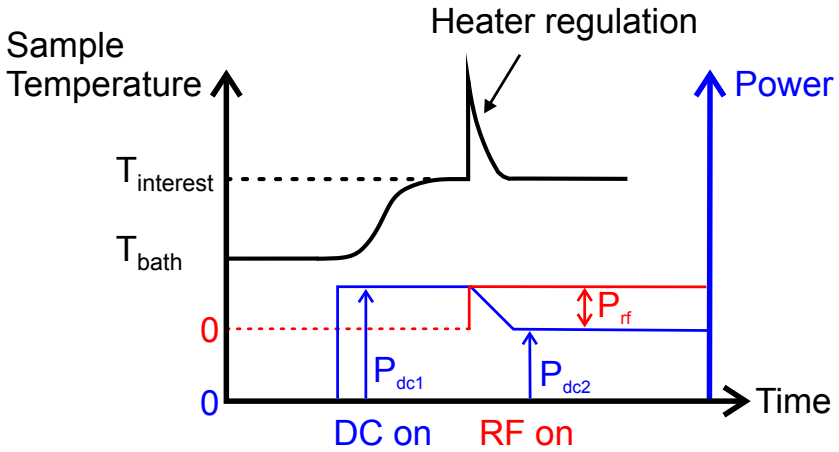

Figure 3.6: Illustration of the RF-DC measurement principle, diagram taken from [55]. The sample is heated to the desired temperature of interest before switching on the RF power. The temperature controller reduces the heater power until the temperature of interest is established. The RF loss is equated to the difference $P_{\mathrm{DC1}} - P_{\mathrm{DC2}}$.

System	Sam ∅ [cm]	Freq [GHz]	Measurement	B_{Sam}[mT]	Temp [K]
TE 011 Cornell	12.7	4.0	RF/Thermometric	105	1.6-4.2
TE 011 Orsay	13	3.88/5.12	RF/Thermometric	25	1.6-4.2
Hemispherical	5.0	11.4	RF Measurement	300	3.6+
Sapphire loaded	5.0	7.5	Calorimetric	20	2+
QPR CERN	7.5	0.4/0.8/1.2	Calorimetric	60	1.8+

Table 3.1: Comparison of surface impedance characterization setups

3.5 Comparison of SRF Sample Testing Experiments

The benchmarks for the different sample testing experiments are summarised in Table 3.1. High peak fields and a wide temperature range are important factors when comparing systems. The higher the frequency, the less sensitive one is to residual resistances and the further one is removed from the actual operating conditions in a superconducting accelerator.

A full comparison between the different systems is not possible in a single table however. The ease with which one can exchange the sample and the turnover time of the entire process - mounting, cooldown, measurement,warm up and demounting are important factor. The hemispherical cavity for instance, has a small and easily demountable sample and requires no liquid helium during cooldown, leading to a very fast turnover time of one day. In comparison, the QPR requires electron beam welding to exchange samples and measurements typically take an entire week.

We see that the systems are tailored for different applications. The high frequency experiments with fast turnover rates are good for studying new thin film deposition techniques, when one wants to quickly scan a large space of deposition parameters. The high frequency systems can never be the ultimate test for the materials however, as the residual resistance cannot be studied at a desirable resolution. This sets apart the Quadrupole Resonator from the other systems - not only does it provide measurements at a frequency typical for SRF cavity, the ability to measure at various frequencies also allows studying frequency sensitive effects such as flux pinning and to probe the superconducting parameters more rigorously.

In the next chapter, the design and production of an improved Quadrupole Resonator, optimized for high field operation, will be presented.

Chapter 4

RF Design of the Quadrupole Resonator

One of the main aims for the HZB Quadrupole Resonator was optimizing the geometry of the niobium rod and loop section to increase the attainable peak magnetic field on the sample while maintaining a high measurement resolution. The RF design of the Quadrupole Resonator is the focus of this chapter. An overview of the electromagnetic modes in the Quadrupole Resonator is given. Figures of merit are defined to compare different geometries after which the influence of various geometric parameters are studied. The resulting design is compared to the baseline model.

4.1 Modes and Field Patterns

Calculating the resonant frequencies and electromagnetic fields of an RF cavity requires solving Maxwell's equations under the appropriate boundary conditions. Combing both curl equations we get:

$$\nabla \times \nabla \times \boldsymbol{E} = \omega^2 \mu \epsilon \boldsymbol{E} \tag{4.1}$$

where ϵ is the complex permittivity given by $\epsilon = \epsilon_r + \frac{\sigma}{i\omega}$, where σ is the conductivity of the material and ω is the frequency. Equation 4.1 is an eigenvalue equation with eigenvalues ω and eigenvectors $\boldsymbol{E}$. Typically, an infinite number of $(\omega, \boldsymbol{E})$ solutions exist, referred to as modes. The boundary conditions are determined by the geometry and the material properties. For all our simulations we treat the surfaces as perfectly conducting.

RF codes such as CST Microwave Studio (MWS) [56] can solve the Maxwell Equations for complex geometries, using mathematical methods such as the Jacobi Davidson Method [57]. This cannot be done generally in the continuous domain, therefore the calculation domain is divided into small discrete cells. For each such finite element, Equation 4.1 needs to be solved. The discretization step is very important for RF simulations and is

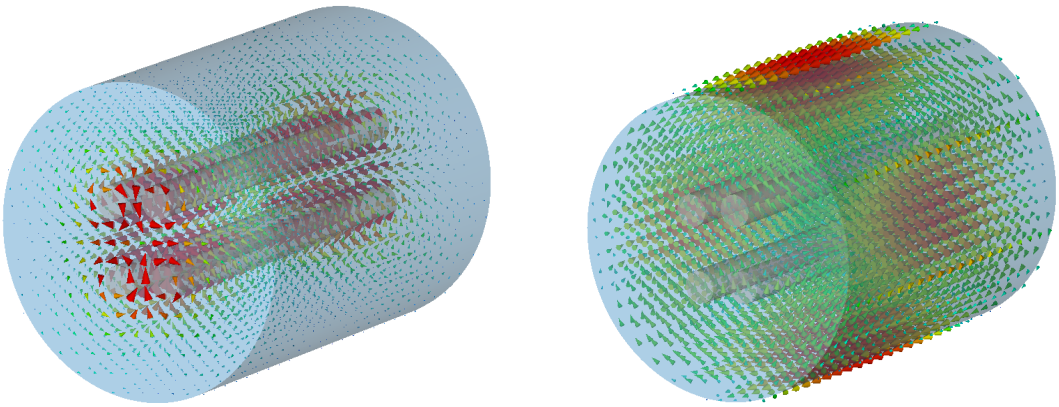

Figure 4.1: Magnetic fields of the TEM_{21} mode (left) and the TE_{211} mode (right) for the simplified geometry. The stored energy is strongly focussed around the rods for the TEM mode. Fields are scaled logarithmically.

referred to as meshing. A too coarse mesh will cause inaccurate results, a too fine mesh will slow down the computation substantially or make it impossible due to excessive memory requirements. Numerical errors caused by finite floating point precision also compound with the number of computation steps.

From an RF perspective, the Quadrupole Resonator is a four-wire transmission line , shorted pairwise close to the bottom end plate. To gain a basic understanding of the electromagnetic modes, we will consider an ideal four-wire transmission line, shorted at either end. Another way to think about this is a pillbox cavity with four parallel rods connecting the end plates. Such a model was studied with Microwave Studio. The dimensions used for this analysis were similar to those of the CERN QPR, the pillbox cavity was of radius 120mm and length z=300mm, the four parallel rods having a radius of 10mm and being centered at x,y = $\pm 20, \pm 30$ mm. In Table 4.1, the first 30 modes of this simplified model are listed. All of the modes up to 1.6 GHz are either TEM or TE modes. In Figure 4.1, the magnetic fields of a typical TEM and a TE mode are shown. It shows that the fields are focussed around and between the rods much more strongly for the TEM modes than the TE modes. This is a useful property, as we are looking to restrict the fields to a small sample if possible. Note that TEM modes are classified by only two indices, l and n, as the index m denotes the radial variation of the longitudinal field components, which do not exist for these modes.

The TEM modes appear at integer multiples of the baseline frequency of 499 MHz in a passband of four degenerate modes. The fields of these modes can be expressed as:

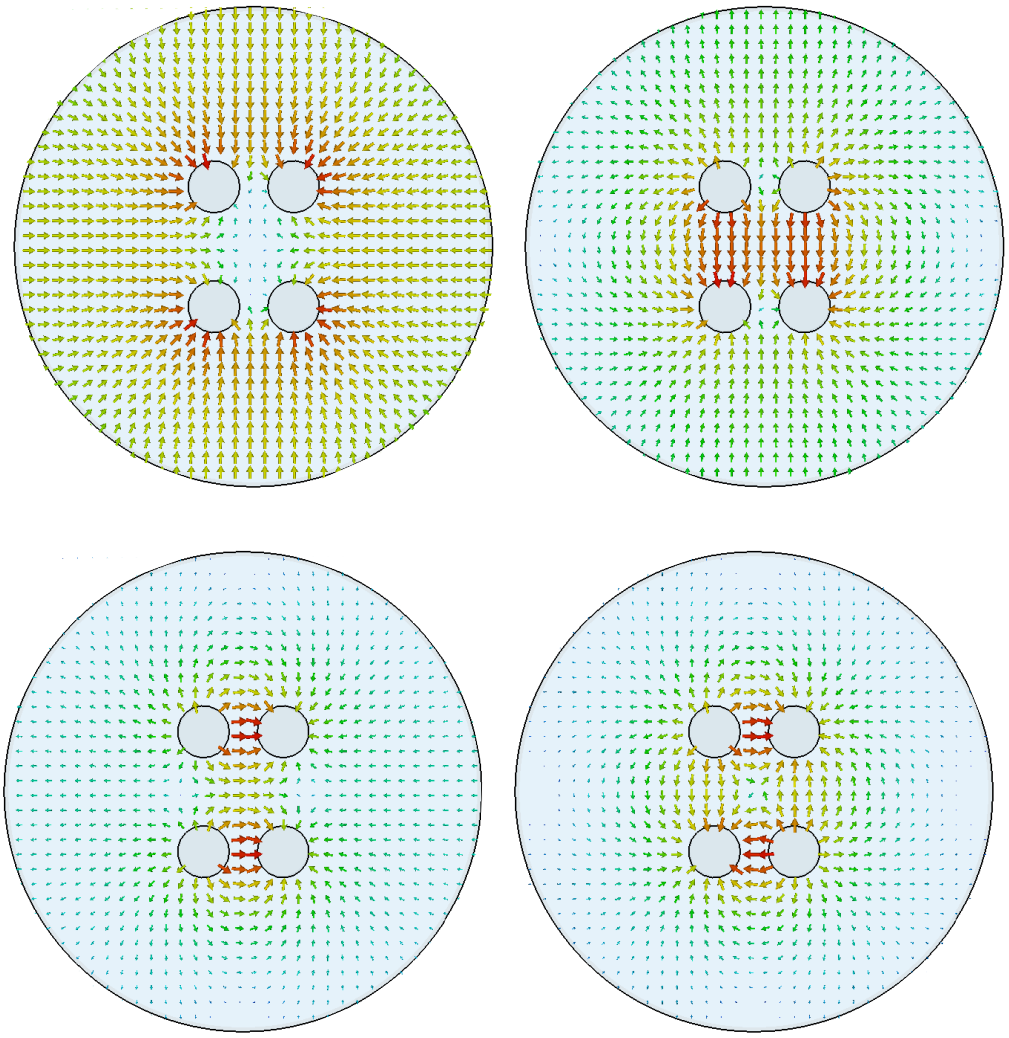

Figure 4.2: Electric field distribution $E_l(\phi, \rho)$ for monopole (top left), dipole (top right, bottom left) and quadrupole mode (bottom right). All the fields are plotted using the same, logarithmic scaling.

$$E_{l,n}(\phi, \rho, z) = E_l(\phi, \rho) \cdot |\sin n\frac{\pi}{L}z| \tag{4.2}$$

$$H_{l,n}(\phi, \rho, z) = H_l(\phi, \rho) \cdot |\cos n\frac{\pi}{L}z| \tag{4.3}$$

One can see, that all TEM modes will have a magnetic field maximum at both end plates. In Figure 4.2, the field lines for $E_l(\phi, \rho)$ are shown. For the monopole case ($l = 0$), the charge on the four rods is the same. The two dipole modes ($l = 1$) have identical charges on neighbouring rods, whereas for the quadrupole mode ($l = 2$) diagonally opposite rods are in phase. In this idealized case there is no frequency shift between the different $\mathrm{TEM}_{\mathrm{ln}}$

No.	Frequency [MHz]	Mode	No.	Frequency [MHz]	Mode
1	499.524	TEM_{01}	16	1495.662	TEM_{13}
2	499.530	TEM_{11}	17	1495.662	TE_{13}
3	499.530	TEM_{11}	**18**	**1495.663**	$\mathbf{TE_{23}}$
4	**499.531**	$\mathbf{TEM_{21}}$	19	1537.059	TE_{212}
5	843.476	TE_{011}	20	1551.664	TE_{212}
6	844.582	TE_{011}	21	1588.789	TE_{021}
7	998.316	TEM_{02}	22	1642.791	TE_{013}
8	998.328	TEM_{12}	23	1643.344	TE_{013}
9	998.329	TEM_{12}	24	1726.096	TE_{311}
10	**998.330**	$\mathbf{TEM_{22}}$	25	1730.681	TE_{311}
11	1207.059	TE_{112}	26	1808.696	TE_{022}
12	1208.421	TE_{212}	27	1831.423	TM_{010}
13	1271.015	TE_{211}	28	1870.183	TM_{110}
14	1288.542	TE_{211}	29	1898.104	TE_{223}
15	1495.642	TEM_{03}	30	1898.320	TM_{011}

Table 4.1: Mode table for simplified Quadrupole Resonator

modes for unchanged n, this changes when a gap is introduced between the connected rods and one of the end plates. Now that we have an idea about the fields within the Quadrupole Resonator, we will move onto the RF design.

4.1.1 Figures of Merit

At the beginning of the RF design, several figures of merit were defined, allowing us to quantitatively compare different geometries:

- The focussing of the magnetic fields onto the sample is given by $c = \frac{1}{2}\int_{\text{Smpl}} |H|^2 dA/U$ and is directly accessible by simulation. The higher the value of c, the larger the fraction of stored energy that will dissipate through the sample, increasing the measurement signal and improving the resolution.

- To maximise the measurement signal (the dissipated power) at a given peak field on the sample ($\hat{H}_{\text{Smpl}}$), the relevant figure of merit is $\frac{cU}{\hat{H}^2_{\text{smpl}}}$. This can also be expressed with the dimensionless quantity $\frac{\langle H^2\rangle_{\text{smpl}}}{\hat{H}^2_{\text{smpl}}}$, which is also measure for the inhomogeneity of the magnetic field on the sample.

- The peak magnetic field $\hat{H}_{\text{rods}}$ on the niobium rods is higher than the peak magnetic field on the sample. As superconductivity breaks down above the critical magnetic

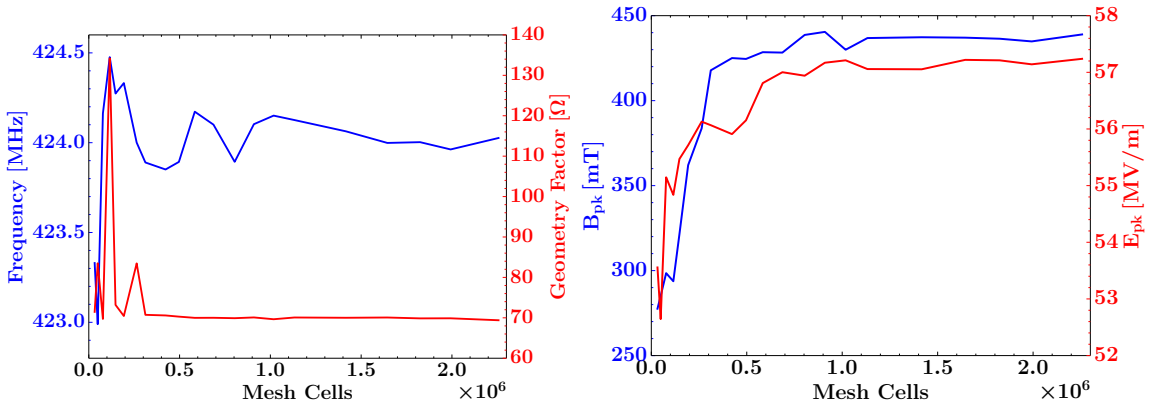

Figure 4.3: Various parameters versus number of meshcells. At over 1 million mesh cells, only small variations in the parameters are observed.

field, increasing the parameter $\hat{H}_{\text{Smpl}}/\hat{H}_{\text{rods}}$ will increase the maximum attainable field on the sample.

- RF fields in a cavity can also be limited by high electric fields (more on this in Section 7.2.1). We therefore want to maximize $\hat{H}_{\text{Smpl}}/\hat{E}_{\text{pk}}$ where $\hat{E}_{\text{pk}}$ refers to the peak surface electric field.

- Heating on the normal conducting flange behind the cutoff tube may cause measurement bias (see Section B.3). To reduce this, we want to maximise the dimensionless factor $\delta = \frac{\int_{\text{Smpl}} |H|^2 dA}{\int_{\text{Flange}} |H|^2 dA}$

4.1.2 Parameter Scans

The next step during the RF design was implementing a fully parametrised model of the Quadrupole Resonator and computing how changes to individual parameters affect the figures of merit. In a first step however, a sufficient mesh had to be determined.

There are two main methods for meshing a 3D geometry within CST, using tetrahedral and hexahedral elements. For the QPR we chose the hexahedral mesh, as this naturally allows a high mesh density in the gap between rods and sample. To find the required mesh density, the same geometry was computed several times with different number of mesh cells. Figure 4.3 shows how frequency, the geometry factor of the sample and the peak electric and magnetic field change with the number of mesh cells. It was found that at over 10^6 cells, the relevant figures of merit did not change significantly any more. For most of the following simulation results, around two million cells were used.

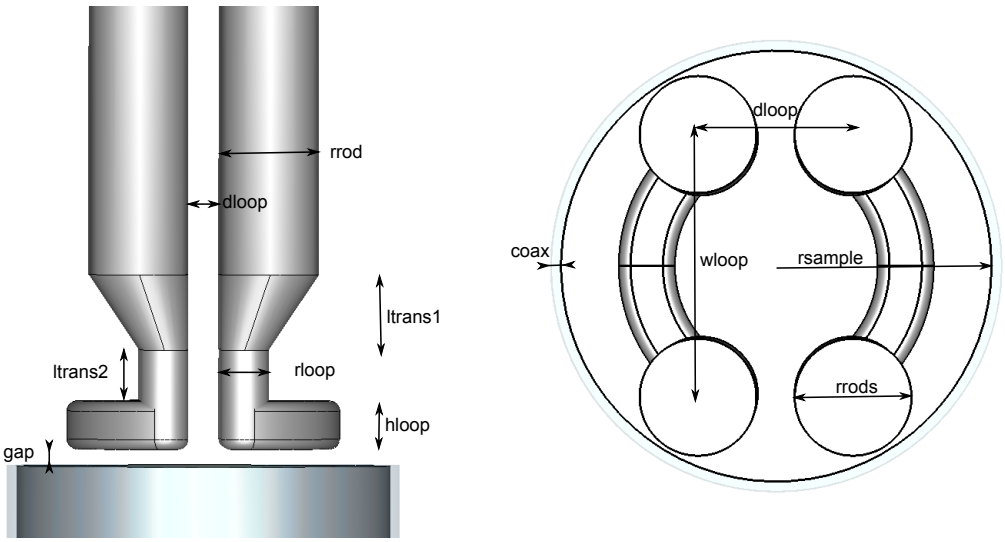

Figure 4.4: Parametrised model of the QPR. Not shown in this diagram are the length of the rods and the radius of the cavity.

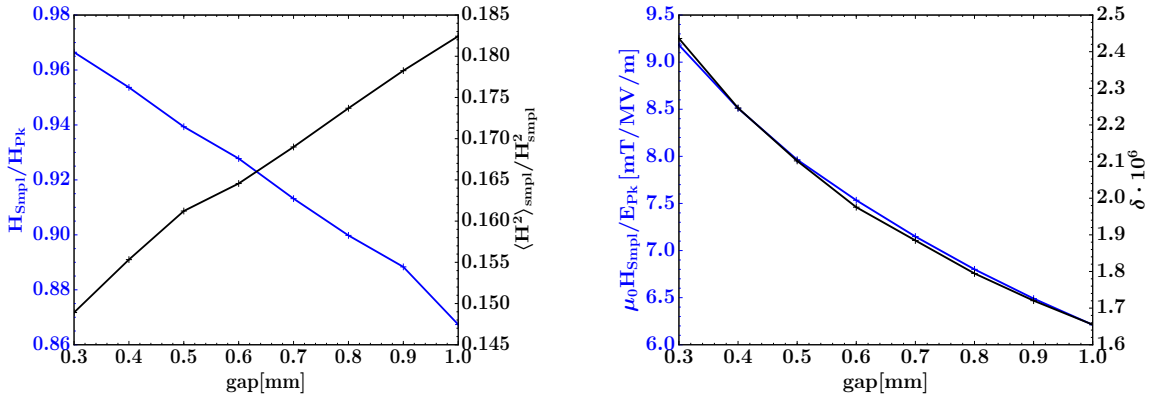

Figure 4.5: Simulation of the RF figures of merit when changing the gap between sample and rods. The peak field ratios improve, whereas the measurement resolution decreases when going towards smaller gap widths.

The starting point of the RF Design was the CERN geometry, adapted slightly in length of the rods to change the fundamental frequency from 400 MHz to 433 MHz. This adaption was done to allow measurements using the higher harmonic mode at 1.3 GHz. A fully parametrised version was created, shown in Figure 4.4, with more than 10 independent parameters available. Every parameter was then varied independently and the influence on the figures of merit was assessed.

As seen in Figure 4.5, the figures of merit were very sensitive to the gap width between sample and rods. Decreasing the gap width improves significantly the peak field ratios H_{Smpl}/H_{pk} and H_{Smpl}/E_{pk}. The ratio of sample to flange heating δ is also improved, whereas the

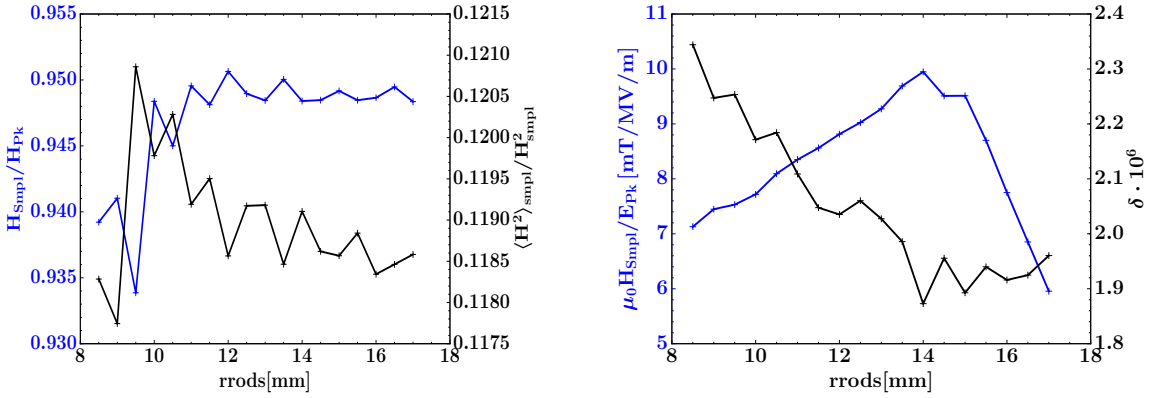

Figure 4.6: Increasing the radius of the rods up from the original 8 mm decreases the peak electric fields on the rods, as the field lines on the curved surface are thinned out. Making the rods thicker will however also decrease their distance eventually increasing the peak field.

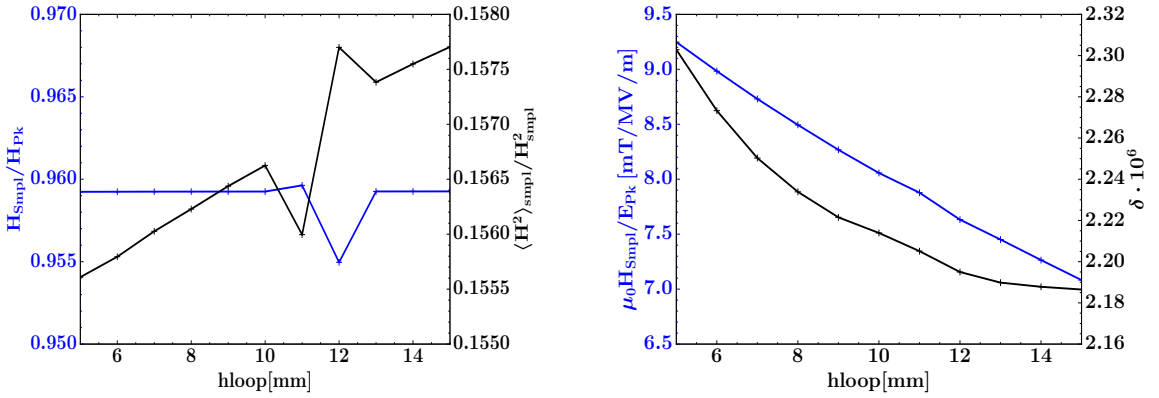

Figure 4.7: Parameter scan of the height of the loop connecting the pair of rods. The effect on the magnetic field distributions is very small, both figures of merit staying within 1% . The value of H_{pk}/E_{pk} however improves significantly towards small values of *hloop*. Mechanical considerations and the requirement of having a cooling channel through this section restricted *hloop* to 10 mm.

Increase Parameter	Frequency	c	$\frac{\langle H^2\rangle_{smpl}}{\hat{H}^2_{smpl}}$	$\hat{H}_{smpl}/\hat{H}_{rods}$	$\hat{H}_{smpl}/\hat{E}_{pk}$	δ
gap	↓	↓	↑	↓	↓	↓
rrods	↑	↓	→	→	↗↘	↗
dloop	↑	↓	↘	→	↑	↓
ltrans	↘	↓	↑	↓	↓	↓
ltrans2	↗	↘	↗	↗	↘	↗
rloop	↗	↑	↑	↘	↓	↑
wloop	↗	↑	↑	→	↗↘	↗
hloop	↗	↘	↗	→	↑	↘

Table 4.2: Influence of increasing a single geometric parameter on the various RF figures of merit. Vertical and diagonal indicate whether a modest change in the geometric parameter influence the figure of merit by more or less than 1%. Parameters are defined such that an increase is always desirable.

field inhomogeniety increases. Reducing the gap thus allows measurements at higher field, at the cost of a slightly reduced measurement resolution. The simulation also showed a very large dependence of the resonance frequency on the gap width $\frac{df}{dz} \approx -1\,\mathrm{MHz}/100\,\mu\mathrm{m}$. In total, decreasing the gap between sample and rods is beneficial with mechanical tolerances giving a lower limit.

A second parameter with a large influence was the radius of the rods, shown in Figure 4.6. We see that the peak electric field can be decreased by increasing the radius of the rods up from the 8 mm of the baseline design. The intuitive explanation for this is that the charge on the rods will spread over a larger surface area. Increasing the radius will however also decrease the distance between the rods, which will eventually cause peak fields to rise again at large radii. There is thus an ideal rod thickness for minimizing the peak electric field, which however depends on other loop parameters *dloop* and *wloop*. For the HZB design, the radius of the rods was increased from 8 to 13 mm. The wider rods also had the effect of increasing the frequency of the lowest mechanical vibrational mode, which was expected to help with microphonics.

Many other parameters, such as the length of the transition between the rods and the loop section (*ltrans*) only have a very small influence on the figures of merit, changing by less 1 % over a wide range. A qualitative summary of the influence of different dimensional parameters is shown in Table 4.2.

After performing the individual parameter scans, a new model with several changes, most notably thicker rods and a smaller gap width, was implemented. Mechanical restrictions place limits on the extent one can change the geometrical parameters to optimize the RF figures of merit, as was seen for the height of the loop *hloop*. The length of the

Parameter	Baseline Design	HZB Design
c	$5.15 \cdot 10^7\ \mathrm{A}^2/\mathrm{J}$	$11.2 \cdot 10^7\ \mathrm{A}^2/\mathrm{J}$
$\frac{\langle H^2 \rangle_{smpl}}{\hat{H}^2_{smpl}}$	0.18	0.16
$\hat{H}_{smpl}/\hat{H}_{rods}$	0.81	0.89
$\mu_0 \hat{H}_{smpl}/E_{pk}$	4.76 mT/(MV/m)	7.69 mT/(MV/m)
δ	$1.65 \cdot 10^6$	$2.1 \cdot 10^6$
1st Mechanical Mode	69 Hz	130 Hz

Table 4.3: Comparison of the figures merit between the baseline and the optimized design.

transition (*ltrans1*, *ltrans2*) had to be used for frequency tuning, to accommodate existing narrow bandwidth RF systems of 433 MHz and 1300 MHz. In contrast to the simplified model presented in Section 4.1, the higher harmonic modes are not precisely at integer multiples of the baseline frequency and thus the length of the rods alone is not sufficient for tuning two modes. The figures of merits for the baseline and the optimized model are shown in Table 4.3. We see that there is significant improvement in the peak field ratios, especially $\hat{H}_{sample}/\hat{E}_{pk}$. A larger fraction of the stored energy is focussed on to the sample, albeit with a slightly higher inhomogeneity. Due to the shorter and wider rods, the lowest mechanical vibrational mode of the rods increases 69 Hz to 130 Hz. [1]

[1] The 69 Hz comes from the microphonic spectrum from the CERN Quadrupole Resonator [54], the 130 Hz is a simulated value. Issues with microphonics for the HZB resonator will be discussed in Section 7.1

Chapter 5

Production and Surface Treatments

This chapter focuses on the period between the completed RF design of the Quadrupole Resonator and the manufactured cavity being ready for commissioning. The mechanical design is shown, tolerance studies and acceptance tests are discussed. The surface treatments, which are required for niobium cavities to maintain low losses at high magnetic field levels, were adapted from the procedures for elliptical cavities and performed at Jefferson Laboratory, Newport News, USA.

5.1 Mechanical model and production

Figure 5.1 shows a cross section of the mechanical design of the Quadrupole Resonator as produced by Niowave Inc., on basis of the RF model developed in Chapter 4. The top and bottom plate of the screening cylinder are inclined, allowing water or acid to flow out of the cavity during cleaning procedures. Four ports extend upwards from the top plate, used for feeding in RF power and for evacuating the cavity. Another change from the CERN design was omitting the flange in the middle of the screening cylinder. This reduced the price for production at the cost of reduced mechanical stability and limiting access to the resonator's interior.

After preparing a test aluminium model of the rods and loop section, the cavity was produced from RRR 300 polycrystalline niobium. The rods and and the outer cylinder were rolled from niobium sheets of thickness 3 mm and 2 mm respectively. For the loop section, top and bottom halves were machined from solid material as shown in Figure 5.2a and subsequently welded together. The sample piece, which would later be used to benchmark the system, was produced from large grain RRR 300 niobium. In was welded to the cutoff tube and subsequently brazed onto the stainless steel flange, a photo is shown in Figure 5.2b.

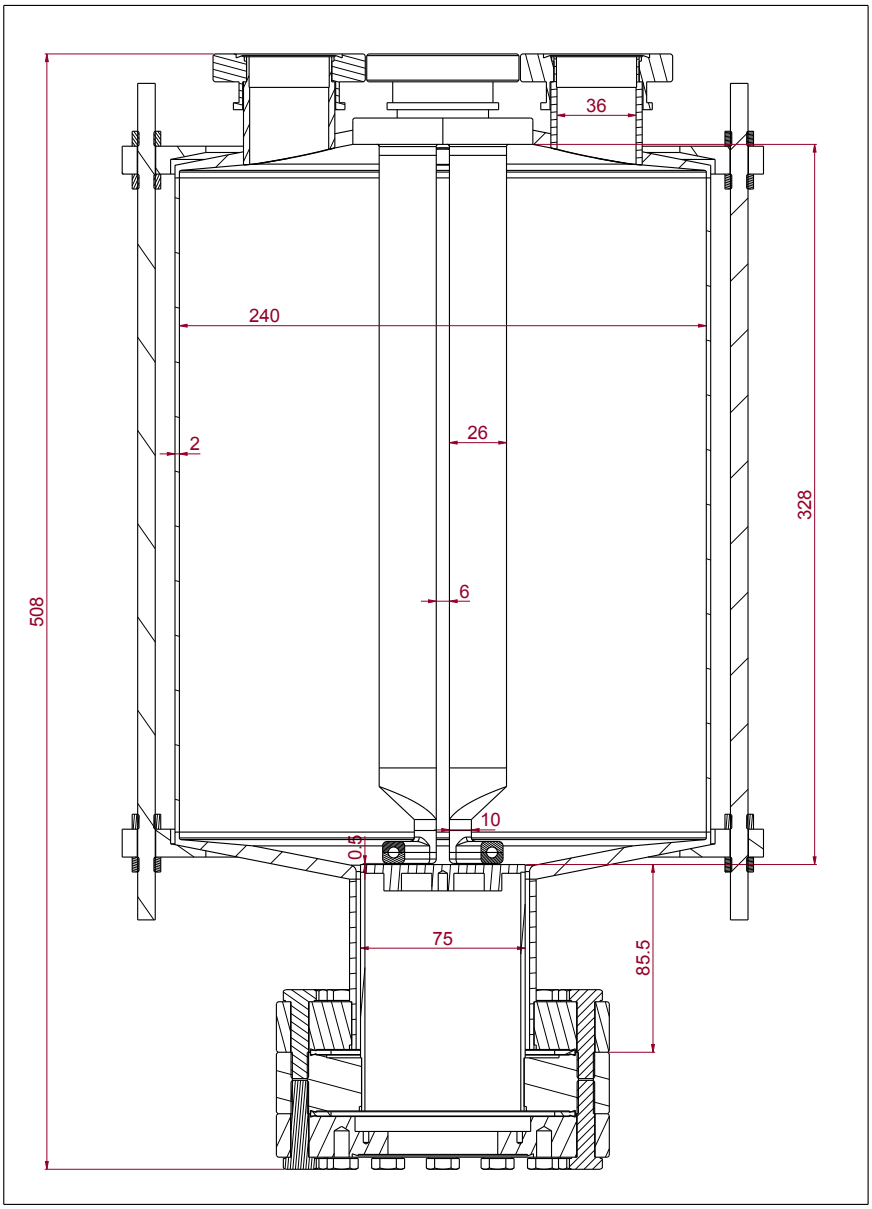

Figure 5.1: Design drawing of the HZB Quadrupole Resonator. The rods are hollow, allowing for efficient cooling by liquid helium into the superconducting state. All measurements shown are in mm.

5.2 Tolerance Studies and Demonstrations

An important step of the pre-production phase of an RF cavity was determining suitable mechanical tolerances to which the manufacturer must adhere to. RF simulations involving the change of single parameters, as shown in Section 4.1.2, were crucial for this assessment. Furthermore, simulations were performed where symmetry breaking effects were studied. Figure 5.3 shows the effect of a vertical offset of one of the niobium loops on the

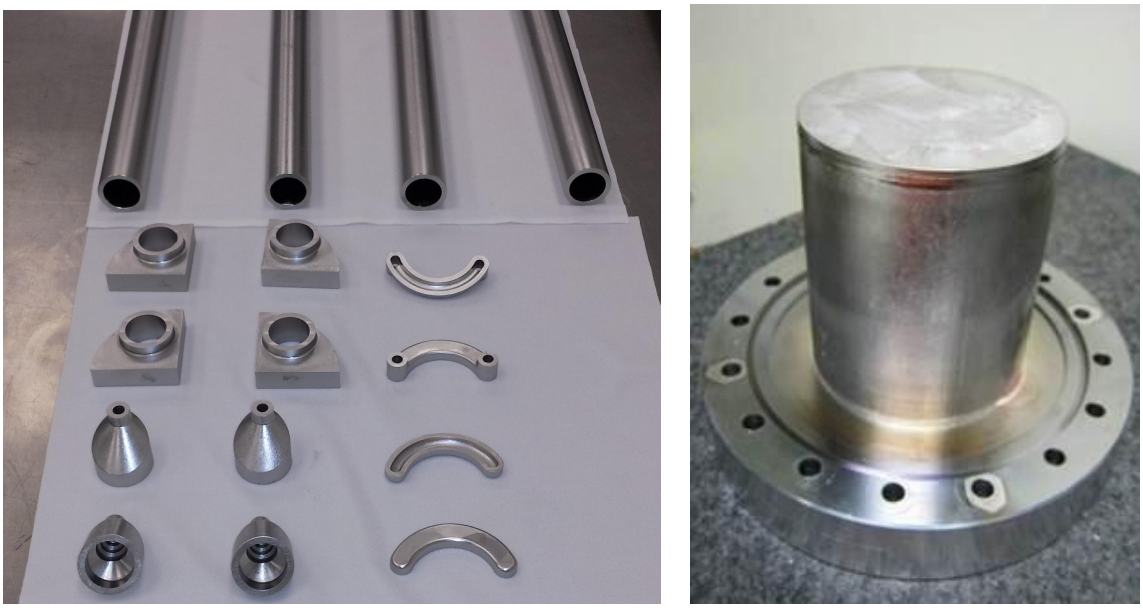

(a) Niobium parts pre-welding

(b) Niobium sample fully assembled

Figure 5.2: Left: Niobium parts for the rods and loop section before welding. All parts are hollow to allow for efficient cooling by liquid helium. Right: Niobium sample, welded to cutoff tube.

measurement results. We see that already a 250 μm shift causes the surface resistance to be overestimated by 10%. A lateral displacement of the sample only has a small direct influence on the surface resistance measurement, it however reduces the effectiveness of the cutoff tube. Overall it was found that manufacturing tolerances could be kept relatively relaxed (DIN ISO 2768-m) without suffering large detrimental effects. The gap between sample and rods being a sensitive parameter was specified to $500 \pm 50\,\mu$m. The parallelism between the loop and the surface was also specified to better than 50 μm.

To test the gap width and the flatness of the loops, an indium crush test was performed after production. For this, four strips of 1.5 mm thick indium were placed on the loops as shown in Figure 5.4. The sample piece was then mounted with a copper gasket until there was metal to metal contact between the two sealing flanges. After removing the sample, the crushed indium was measured using a dial indicator. The results show that the gap remains within 20 μm of the nominal value. Two further acceptance tests were measuring the coaxial gap at different azimuthal positions using a set of pin gauges in a go/no go test and measuring the flatness of the niobium loops.

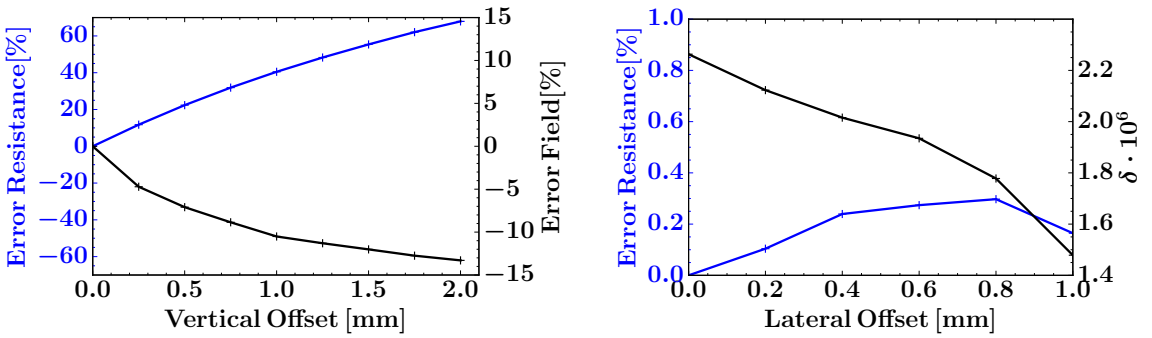

Figure 5.3: Left: Field and Resistance error caused by vertical offset of one of the two niobium loops. Right: Lateral displacement of the sample only causes small measurement error, significantly reduces the effect of the cutoff tube however.

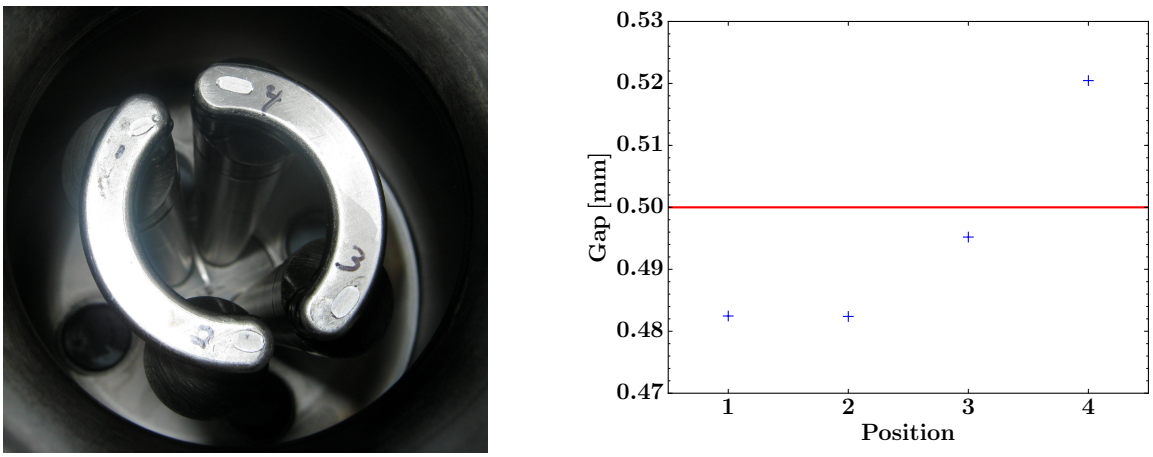

Figure 5.4: Indium Crush Test: The four indium test strips are placed at the ends of the niobium loops, and subsequently crushed by fastening the sample piece into position. The results show good agreement with the target value (red).

5.3 Surface Treatments

After production at Niowave, the QPR was shipped to Jefferson Laboratory for surface processing. Surface treatment mainly followed the standard procedure for niobium cavities [30], which is used on elliptical cavities to reliably ensure both high gradients and quality factors. For material removal, buffered chemical polishing (BCP) replaced the more complicated electro polishing. The procedures performed were:

1. Degreasing
2. 150 μm Buffered Chemical Polishing (BCP)
3. High temperature 600° C bake
4. 10 μm light BCP
5. Rinse to resistivity in ultrapure water (18 M$\Omega \cdot$ cm)
6. High pressure rinse
7. Low temperature 120° C bake

In the subsequent sections, more details will be given on the BCP, the high temperature bake and the High Pressure Rinse.

5.3.1 Buffered Chemical Polishing

Buffered Chemical Polishing is used to remove the top 150 – 200 μm layer of the inner surface of a niobium cavity. This is necessary, as the top layer of 80 – 120 μm is damaged during the mechanical preparation of the niobium sheets, used to form the cavity. As the niobium rods were made by rolling niobium sheets, these figures were applied as well.

The solution used to etch the niobium is a mix of hydrofluoric acid (HF), nitric acid (HNO_3) and phosphoric acid (H_3PO_4), which acts as a buffer to slow the chemical reaction. The nitric acid reacts with the niobium acid to form the oxide Nb_2O_5, which is then dissolved by the hydrofluoric acid into water soluble NbF_5 The chemical reactions are:

$$\begin{aligned} 12\,\mathrm{Nb} + 10\,\mathrm{HNO_3} &\rightarrow 10\,\mathrm{NO_2} + 5\,\mathrm{H} + \mathrm{Nb_2O_5} \\ \mathrm{Nb_2O_5} + 10\,\mathrm{HF} &\rightarrow 2\,\mathrm{NbF_5} + 5\,\mathrm{H_2O} \end{aligned} \tag{5.1}$$

A photo of the QPR in the BCP cabinet of JLab is shown in 5.5. The acid inlet was mounted to the bottom flange, at the position where the sample chamber is typically

Figure 5.5: Photo of the QPR mounted in the JLab BCP cabinet. The acid inlet is through the bottom opening where the thermometry chamber is mounted, two of the top auxiliary ports are used as outlets.

mounted. Two of the ports on the top plate served as the outlet. Custom plugs made from acid resistive polyethylene were used to protect the brazes connecting the niobium cavity to the stainless steel flanges.

The reaction rate of the entire process depends strongly on the temperature and the acid flow rate. For elliptical cavities it was found that for a typical acid flow rate, the material removal rate differs by a factor of 1.9 between iris and equator [58], suggesting a non-uniform process for the Quadrupole Resonator as well. The process was monitored by an ultrasonic device measuring the changing wall thickness of the outer cylinder. To measure the material removal from the bottom of the rods, a coordinate measurement machine was used post chemistry (see Section 5.3.5).

5.3.2 High Temperature Bake

Soon after adopting Niobium as the material for superconducting cavities, it was found, that slowly cooling down the cavity at temperatures of around 100° K led to severe degradation of the quality factor [18], a phenomenon described as "Q-disease". These additional losses were attributed to niobium hydrides. At room temperatures, very high hydrogen concentrations are required to form hydrides. In the temperature range of $-70°$ K $-150°$ K however, the critical concentration is lowered by three orders of magnitude [4]. Niobium hydrides are normal conducting or only weakly superconducting, thus increasing the surface resistance greatly if they precipitate close to the surface.

Cooling down quickly through the critical temperature range can prevent Q degredation. This is due to the fact that hydrogen present in the material is initially concentrated at lattice defects, vacancies as well as at the interface between the niobium oxide layer and the bulk niobium. In the critical temperature range, hydride islands will start growing, so that reducing the time spent in this period is beneficial. A detailed description of this process is found in [59].

A different method for preventing Q degradation is lowering the hydrogen content in the niobium. As the niobium lattice has an affinity for absorbing hydrogen, some hydrogen will be present in the sheet material. The hydrogen content further increases after chemical procedures such as BCP. To remove the hydrogen, the most efficient method has been found to heat the cavity to temperatures above 600° C in a high vacuum furnace and degas the hydrogen. The QPR was treated at 600° C for 10 hours.

5.3.3 High Pressure Rinse

The high pressure rinse is used to remove any particulates from cavity surfaces and is typically performed after the chemical treatments. Ultra pure water is pressured to $70 - 100$ bar with a water compressor and sprayed to the cavity wall through a nozzle. The cavity is rotated continuously, to cover the entire surface area and to make sure that the same spot is not hit for a prolonged period, as this causes surface damage.

As the clearance between the rods is just 28 mm, the nozzle was not moved between the rods but kept below the niobium loops. The nozzle used had a 15° spray jet and was operated at around 55 bar pressure. For testing purposes, an acrylic glass model of the QPR was produced using a 3D printer, with which the spray pattern could be observed. Detailed information concerning the High Pressure Rinse setup at Jefferson Lab can be found in [60].

5.3.4 120° C Bake

Baking a cavity at around 120° C for a prolonged period (typically 48 hours) has two main effects [61]:

- A significant reduction of the BCS surface resistance, up to 50 % at 4.2 K.
- Disappearance of the high field Q-drop, a sharp decrease of the quality factor at high fields not caused by field emission (determined by the lack of X-rays).

The decrease of the BCS surface resistance indicates a reduction of the electron mean free path, moving it closer towards the mimimum of surface resistance shown in Figure 2.4. This can be correlated to surface analysis studies, which showed a modified oxide structure after baking, with a dissolution of the niobium pentoxide phase (Nb_2O_5) combined with a decrease of the oxygen concentration in the surface region due to diffusion into the bulk [62].

Furthermore the 120° C can also help against hydride formation, which was introduced in Section 5.3.2. This is due to hydrogen being released from vacancies, thus reducing the hydrogen content. Additionally, oxygen migrating through the material will compete with the hydrogen at lattice vacancies, thus reducing the nucleation centers for hydride percipitates [63].

The QPR was baked 'in situ' for 48 hours at 120° C, remaining evacuated in the process.

5.3.5 Coordinate Measurement Machine

A Coordinate Measurement Machine (CMM) is a device routinely used for dimensional measurements of RF cavities. It uses a touch trigger probe which can be moved in three orthogonal directions to map the (x,y,z) coordinates of a surface. For measurements of the niobium loops, the origin was determined by taking the average value of four points taken on the flange surface to which the calorimetry chamber is mounted. Eight points were then recorded, the results are shown in Figure 5.6. To compensate for the alignment error between the CMM and the resonator, the inclination of the coordinate system was fitted to minimize the square of the deviations of the z-coordinate. The dimensions of the sample were also measured with the CMM, allowing to determine the gap width between loops and sample to be 750 μm when mounted without a gasket.

A useful measurement was performed at this point in repeatedly measuring the resonance frequency of the QPR - first with the sample being mounted to the resonator without a gasket, later using a copper gasket. Here the measurement was performed with the screws

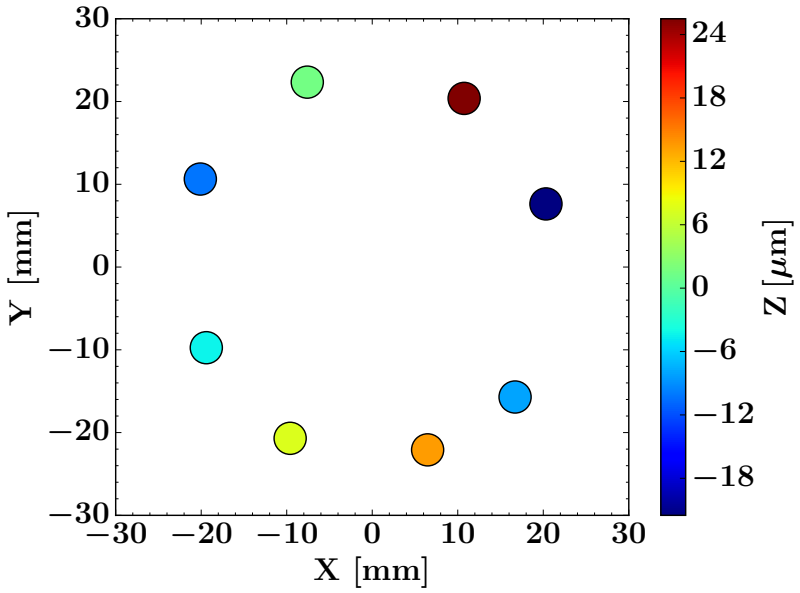

Figure 5.6: CMM measurement of the niobium loops, measuring the X,Y,Z coordinates at eight locations with a micrometer precision. The flatness of the loops is within the specified 50 μm

being fastened first loosely, then tight. In each case, a feeler gauge was used to measure the distance between the flange surfaces. This frequency measurement combined with the gap measurement performed with the CMM, allows for a subsequent absolute gap calibration using only the resonance frequency in the warm state.

Chapter 6

Experimental Setup

The experimental setup consists of three main components. The first is the cryostat in which superconducting cavities are tested. The second is the RF system, required to power the cavities and stabilize RF fields. Third is the thermometry system, used for the RF-DC compensation measurement with the Quadrupole Resonator which was introduced in Section 3.4.

6.1 Helium Bath Cryostat

When it comes to testing SRF cavities, one typically distinguishes between horizontal and vertical testing. The distinction goes further than the alignment: for horizontal testing, a cavity has to be welded into a helium tank, allowing for auxiliary components such as tuners and high power couplers to be mounted. For vertical tests, a naked cavity is tested within a liquid helium bath.

At HZB, testing cavity horizontally has been possible since 2006 in HoBiCaT [64]. A new helium bath cryostat was commissioned and built in 2014 for vertical testing. Figure 6.1 shows a diagram of the cryostat which was manufactured by Kriosytems. In contrast to other cryostat designs, no liquid nitrogen shield was used. Instead, the radiation shield is cooled down by the helium gas flowing through the exhaust pipe. The temperature of the radiation shield typically drops to around 60 K during filling of the cryostat, when the helium flow through the exhaust is highest. During operation, only very little helium is evaporated and the shields reach an equilibrium temperature of around 150 K. The static losses of the cryostat are 2-3 Watts.

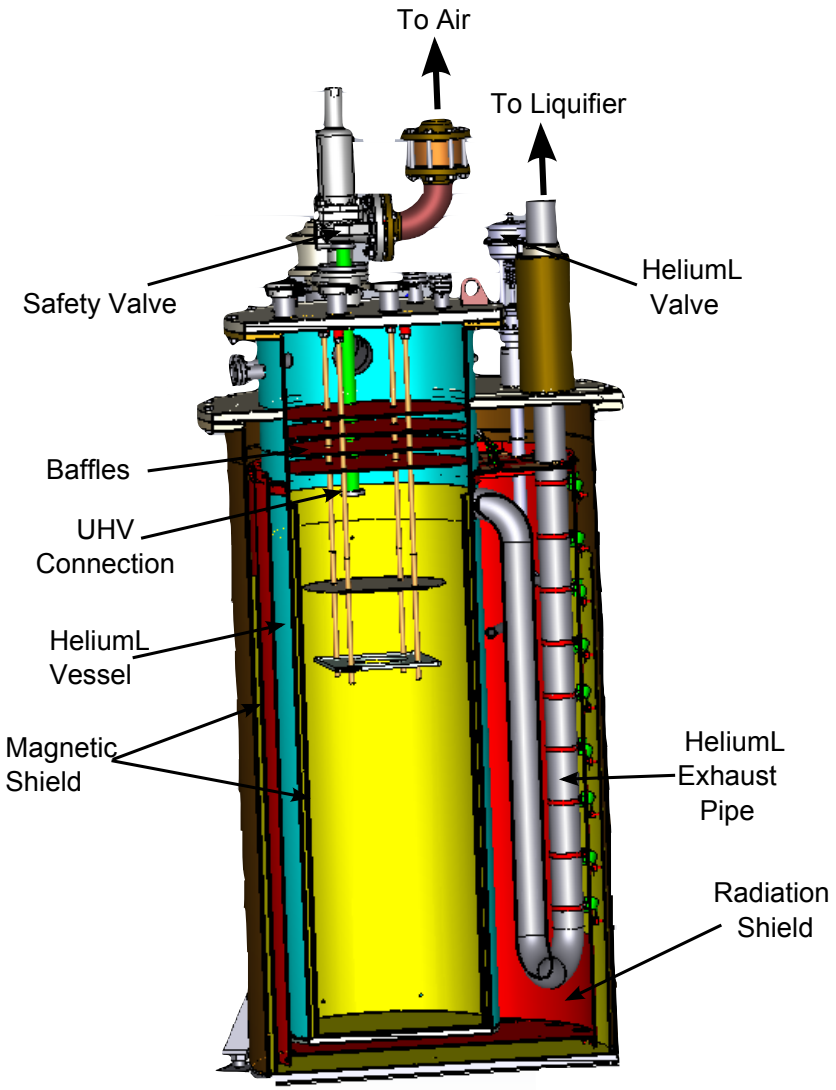

Figure 6.1: Helium Bath Cryostat at HZB. The helium tank has a height of 220 cm with a filling height of 140 cm.

Another important features are the two magnetic shields, as a low magnetic field environment is essential for high quality factor cavities. A magnetic shield is made out of very high permeability material ($\mu_r > 10^4$) and a saturation magnetization greater than 800 mT. It shields an inner volume by diverting the magnetic field lines through the shield and thus around the shielded area. The field attenuation factor of a single shield is proportional to the thickness of the shield. If two shields are sufficiently far apart, the attenuation factors of both shields are roughly multiplied, thus providing for a more efficient use of material.

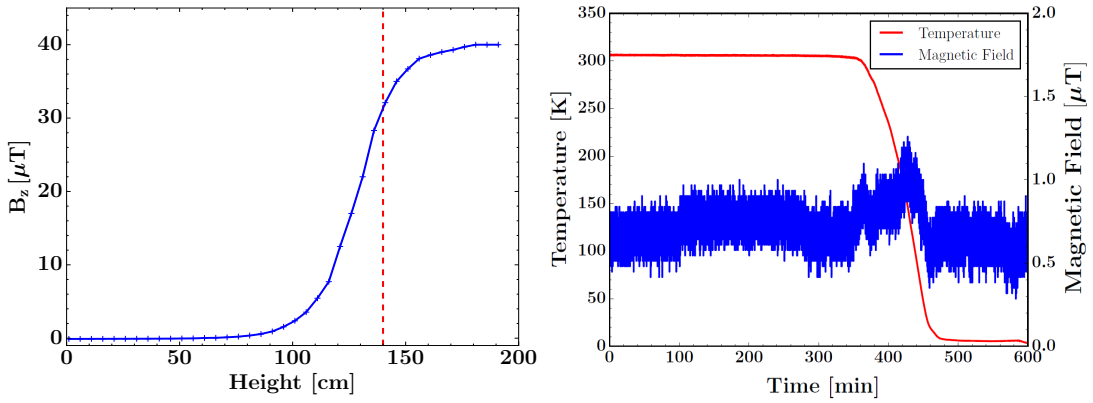

Figure 6.2: Left: Magnetic Field in the vertical test stand. Below 70 cm, the field is attenuated to below $< 1\,\mu$T, the red dotted line is the maximum filling height Right: Magnetic field probe in the QPR during cooldown. Right: The performance of the magnetic shield does not degrade with dropping temperature.

In our configuration, the outer shield is located in the vacuum vessel and is made out of MuMetal. The inner shield is inside the liquid helium tank and is made of Cryophy, a material for which the permeability increases at cryogenic temperatures. Both MuMetal and Cryophy are commercially available Nickel-Iron alloys.

Several simulations were performed to correctly dimension the magnetic shields. It was found, that if one leaves a cylindrical shield open at one end, the field will decay exponentially inside with a characteristic length similar to the radius of the cylinder. A measurement of the magnetic field down into the cryostat is shown in Figure 6.2, alongside with a measurement of how the remanent field changes during cooldown. We see that for a cavity installed at below 60 cm, we have a remaining field of $< 1\,\mu$T at cryogenic temperatures.

6.2 RF System

During operation, the resonance frequency of the cavity (the QPR) will constantly be changing due to pressure fluctuations of the helium, pressure drift from helium depletion, mechanical vibrations or Lorentz Force detuning. To maintain stable fields, the applied RF frequency (f) must remain at the resonance of the cavity (f_0). For the input coupling typically used for the QPR, the bandwidth is around 100 Hz.

To compensate detuning, a phase lock loop system is used, shown in Figure 6.3. A feedback voltage is generated by mixing the RF input signal with the transmitted signal of the cavity. Both signals will have the same frequency but a phase shift $\Phi = \Phi_{\text{const}} + \Phi_{\text{var}} +$

$\Phi_{\mathrm{Cav}}(f - f_0)$, where Φ_{const} is a constant phase shift by the signal pathway, Φ_{var} is the shift caused by the variable phase adjuster. The phase shift between incident and transmitted signal through a detuned cavity is given by:

$$\tan(\Phi_{Cav}) = -2Q_L \frac{f - f_0}{f_0} \tag{6.1}$$

For small detuning, one has a linear relationship between detuning frequency and phase shift. The signal transmitted through the cavity ($\boldsymbol{V}_{\mathrm{In}}$) is mixed with a signal directly from the generator $\boldsymbol{V}_{\mathrm{LO}}$ to produce a DC and a $2f$ signal, from which the DC component is extracted using a lowpass:

$$\begin{aligned} V_{\mathrm{Out}} &= V_{\mathrm{In}} \cos(\omega t + \Phi_{\mathrm{In}}) \cdot V_O \cos(\omega t + \Phi_{\mathrm{LO}}) \\ &= \frac{1}{2} V_{\mathrm{In}} V_{\mathrm{LO}} \sin(\Phi_{\mathrm{In}} - \Phi_{\mathrm{LO}}) + \cancel{V_{\mathrm{In}} V_{\mathrm{LO}} \sin(2\omega t)} \\ &\approx \frac{1}{2} V_{\mathrm{In}} V_{\mathrm{LO}} \Delta\Phi \end{aligned} \tag{6.2}$$

Ideally one uses the variable phase shifter to set $\Delta\Phi = \Phi_{\mathrm{In}} - \Phi_{\mathrm{LO}} = \Phi_{\mathrm{Cav}}$, obtaining a signal which is negatively proportional to the frequency offset. Equation 6.2 also demands that the amplitude of both signals going into the mixer remain constant, as a change in amplitude can not be discerned from detuning induced phase shift. For this reason, a limiting amplifier is is used on the transmitted signal.

The feedback signal is finally used to modulate the RF frequency produced by the signal generator. The frequency the generator outputs is $f = f_C + g \cdot V$, where f_C is the manually set center frequency, V is the feedback voltage and g is the gain factor, typically several kHz/V.

Not shown in Figure 6.3 are the connections of the individual components to the control and DAQ system. Both control and data acquisition are united in a single Labview program, run on an a commercial PC equipped with a National Instruments PCI-6229 board. In total 32 analog channels can be read and four analog voltages can be output in the -10V to 10V range. The analog voltages are used to control the adjustable phase shifter and attenuator, required for setting the desired RF field level. The RF power sensors are of the type Gigatronics 80322A and are read out with a Gigatronics 8540 power meter. The signal generator used is a Rohde and Schwarz SML03, which can be run in a frequency modulated (FM) mode and also can also provide RF pulses, necessary for measurements at high field.

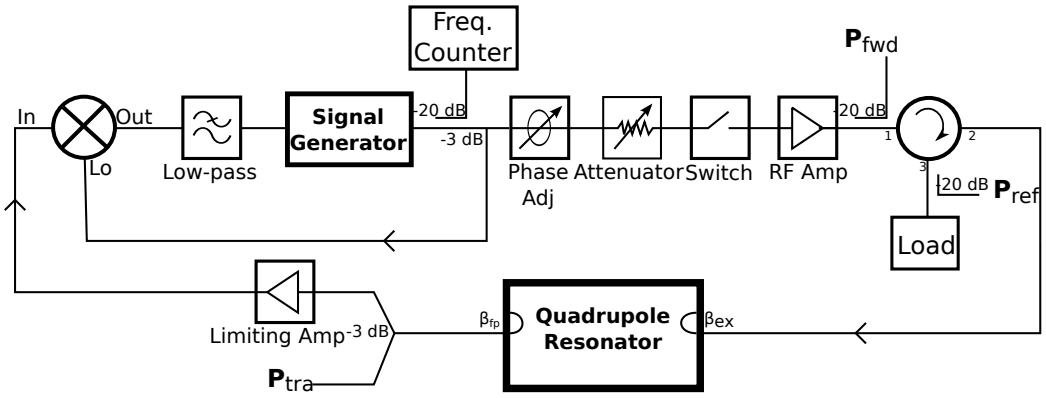

Figure 6.3: Schematic of the phase-locked loop used for testing the QPR. The RF signal of the generator is split and subsequently recombined in a mixer, with one branch having passed through the cavity. This creates a feedback signal which can compensate differences between the generator and the cavity resonance frequency.

An important issue in setting up the RF system is a correct calibration of the RF power sensors P_{fwd}, P_{ref} and P_{tra}. The procedure to calibrate the cables was taken from [65], which provides much useful information on testing SRF cavities. A photograph of the RF rack, standing next to the cryostat in the testing environment is shown at the end of this chapter in Figure 6.5.

6.2.1 Field calibration

During RF tests, superconducting cavities are typically equipped with two coupling antennas. The first is the external coupler, which feeds power into the cavity. The second is a weakly coupled field probe, which does not perturb the fields but can be used to measure them. Similar to the definition of the intrinsic quality factor Q_0 given in Equation 2.5, the quality factors Q_{ex} and Q_{fp} can be defined, giving an expression for the amount of power flowing out of either coupler when a cavity is left to ring down:

$$Q_{\text{fp}} = \frac{\omega_0 U}{P_{\text{tra}}} \qquad Q_{\text{ex}} = \frac{\omega_0 U}{P_{\text{ref}}} \tag{6.3}$$

Once the value of Q_{fp} is known, measuring the transmitted power gives us knowledge of the stored energy inside the cavity. The relation between stored energy and peak magnetic field is different for each cavity and needs to be simulated. For the HZB Quadrupole Resonator it is:

$$\frac{B_{pk}}{\sqrt{U}} = \frac{440\,\text{mT}}{\sqrt{1\,\text{J}}} \tag{6.4}$$

For critically coupled cavities ($Q_0 \approx Q_{ex}$), a decay time measurement can be used to calibrate Q_{fp}. For a strongly coupled cavities ($Q_{ex} \ll Q_0$), this method leads to very large errors [65, 66]. Therefore, an emitted power measurement is used for the field calibration. It works on the principle, that when a strongly coupled cavity is left to ring down, nearly the entire stored energy flows back through the input coupler. The integral over the entire power pulse measured with the reflected power meter can be related to the stored energy:

$$U \approx \int_{t_0}^{\infty} P_{ref}(t)dt \approx \sum_{m}^{N} P_{ref}\Delta t \tag{6.5}$$

where Δt is the sampling time of the power meter, N is the number of samples and m is the sample at which the RF power is switched off. To make such a measurement, one needs sufficiently fast power meters which can resolve an expected decay time of:

$$\tau = \frac{Q_L}{\omega_0} \approx \frac{Q_{ex}}{\omega_0} \approx \frac{10^7}{2\pi \cdot 416\,\mathrm{MHz}} = 3.8\,\mathrm{ms} \tag{6.6}$$

It should be noted that the emitted power measurement does not allow us to measure Q_0 directly. For the QPR this is inconsequential, as the value of Q_0 plays no part in the calorimetric measurement.

6.3 Thermometry System

Figure 6.4 shows a cross section of the thermometry chamber with full instrumentation. The flat sample disc is welded to the cut off tube and connected to a doubled sided stainless steel flange using an indium seal. The top side of the flange is then connected to the resonator, the bottom side seals off the chamber from the cryostat.

A heater and several temperature sensors are mounted directly to the bottom side of the sample. The heater is composed of a copper body with cryogenic heating wire (Lakeshore MW-30), which has a temperature independent resistance wrapped around it. The thermal contact is provided by Apiezon N grease. The temperature sensors used are calibrated Cernox CX-1050 resistors which have a very large sensitivity of $> 10^3\,\Omega/\mathrm{K}$ at cryogenic temperatures. The sensors are read out by a Lakeshore 336 temperature controller, which also controls the heater current. The temperature of the sample can be stabilized to 0.1 mK with this setup.

A copper mounting frame is also attached to the sample, supporting a coil and a single axis fluxgate magnetometers used for trapped flux studies (see Section 8.3). Furthermore, space is provided for winding heating wire around the copper support frame and using it as a heater. This solution provides the benefit of a reduced temperature gradient across the

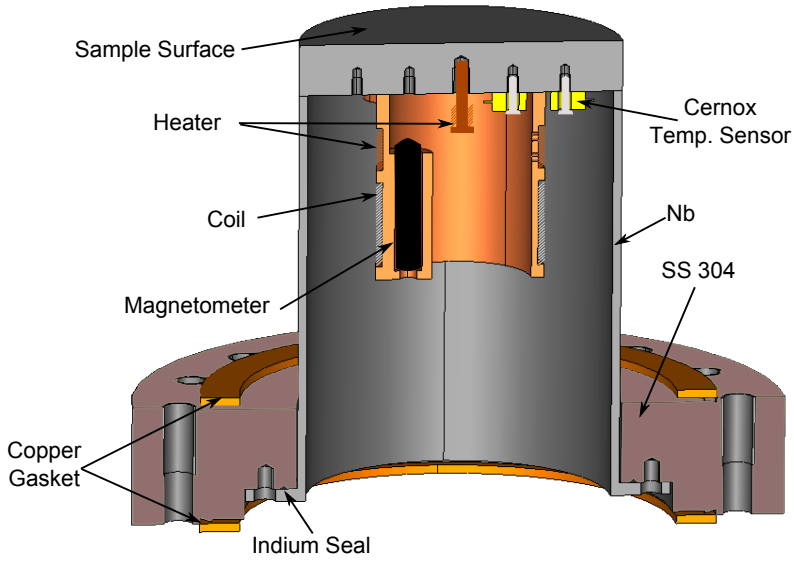

Figure 6.4: Schemata of the calorimetry chamber. Heater and temperature sensors are mounted to the sample directly. A copper holding frame supports the coil and magnetometer for trapped flux studies. The niobium cutoff tube is screwed on to the stainless steel flange using an Indium gasket.

sample compared to the central heater. For the data shown in this work, a central heater was used.

Several iterations of thermometry chambers have been tested at HZB during the past years. Within the work of [67], a thermometry chamber was designed where the flat sample was mountable by screws to the cutoff tube. Unfortunately, this attempt has not provided satisfactory results so far, with measured surface resistances being in the $\mu\Omega$ range for niobium samples. The reason for this remains unclear, field enhancement at the gap between sample and cutoff tube causing normal conducting losses are a possibility.

Figure 6.5: Photo of the helium cryostat and the 19 inch rack housing the RF and thermometry control system.

Chapter 7

Commissioning of the Quadrupole Resonator

One of the main aims of the Quadrupole Resonator at Helmholtz-Zentrum-Berlin was to extend the measurement capabilities to high RF fields. The attainable fields in superconducting cavities, given sufficient RF power, are generally determined by high field effects such as field emission, magnetic quench or multipacting.

For the Quadrupole Resonator, the effect of mechanical perturbations on the resonance frequency was found to be very high compared to standard elliptical cavities, and during the first runs the field limit was determined by the frequency control system, the phased-lock-loop introduced in Section 6.2.

All of these aspects were challenges that needed to be overcome during the commissioning phase of the Quadrupole Resonator

7.1 Detuning and Microphonics

One of the main challenges during commissioning was microphonics. Microphonics is a term used to describe the unwanted generation of noise by mechanical vibrations. For RF cavities, microphonics refers to the detuning of the resonance frequency of the cavity. Microphonics can be problematic for cavity operation, as the excitation frequency provided by the RF source has to be within the bandwidth of the cavity for stable field.

In general, any deformation of the cavity wall will result in detuning of the resonance frequency. There are two main causes of static detuning for RF cavities:

- Change in resonance frequency due to external pressure. The term $^{df}/_{dp}$ is a measure for how strongly the cavity suffers from microphonics due to pressure fluctuations.

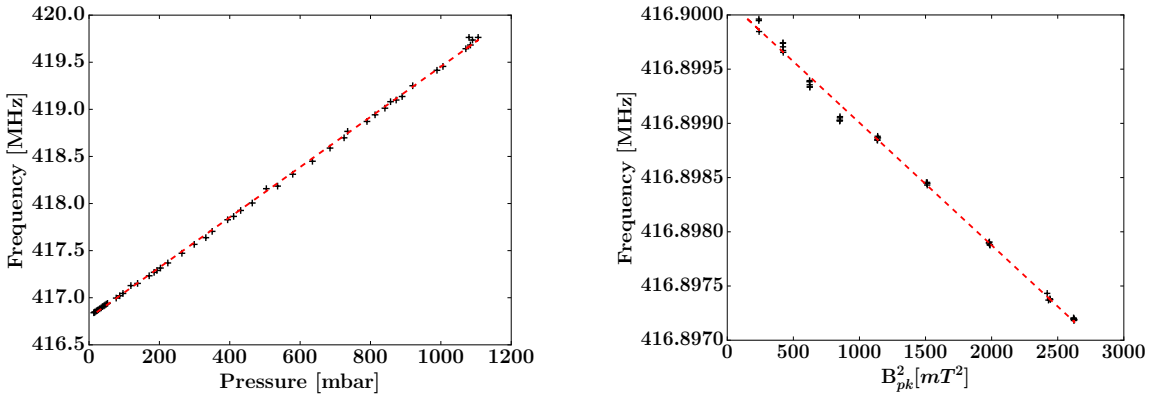

Figure 7.1: Measurement of the static detuning parameters $^{df}/_{dp}$ = and K_L.

- Lorentz force detuning. The pressure caused by an RF field on the cavity surface is given by:

$$P = \frac{1}{2}(\epsilon_0 E^2 - \mu_0 H^2) \tag{7.1}$$

  The figure of merit used to compare cavities is the Lorentz force coefficient $K_L = {}^{\Delta f}/_{E^2_{acc}}$. As the QPR does not have an accelerating gradient E_{acc} we will normalize this value to the peak magnetic field B_{pk} instead.

In Figure 7.1, measurements of $^{df}/_{dp}$ and the Lorentz Force coefficient are shown for the QPR. For the pressure sensitivity, the value of 2.6 kHz/mbar is three orders of magnitude above typical values for elliptical cavities with $^{df}/_{dp} \approx 3$ Hz/mbar Nearly the same is also true for the Lorentz force coefficient which was 0.96 Hz/mT^2 for the QPR compared to ~ 0.05 Hz/mT^2 for TESLA type cavities [5].

Static detuning of the Quadrupole resonator was also studied in coupled mechanical-RF simulations, for which the Lorentz Detuning coefficient was within 50% of the measured value. It was shown that the Lorentz forces act strongly on the loop section, causing the connected rods to come closer together. As the fields are strongly concentrated in this region of the resonator, the resulting detuning is very large.

7.1.1 Dynamic Detuning

During the commissioning run of the Quadrupole Resonator at HZB, the attainable peak field was limited to 30 mT in CW and 60 mT in pulsed operation. The limitation occurred due to the phased-lock loop losing it's lock on the resonance frequency. The detuning of the cavity can be measured directly by sampling the error signal produced by the mixer in the phased-lock-loop. Figure 7.2 shows how the resonance frequency of the cavity changes

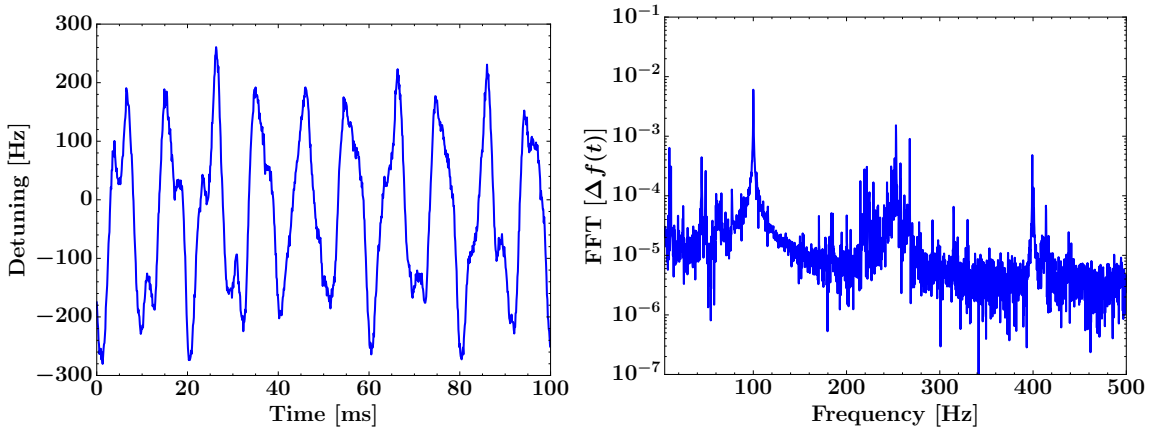

Figure 7.2: Left: Detuning of the Quadrupole Resonator in a 100 ms time period. Right: Fourier transform of the detuning signal. Several resonance peaks are visible, around 100, 250 and 400 Hz.

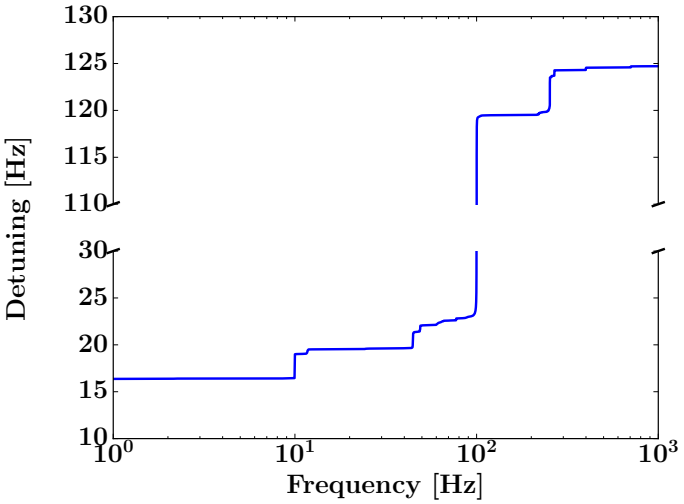

Figure 7.3: Cumulative Detuning spectrum of the Quadrupole Resonator. Most of the detuning is caused by the 100 Hz perturbation, note the gap in the y-axis.

over a period of 100 ms. We see that peak to peak detuning is around 400 Hz, much higher than typical values for elliptical cavities in the $1 - 10$ Hz range [68]. The detuning is also shown in the frequency domain, several distinct peaks being visible.

To determine the contribution of each frequency component to the total detuning, a cumulative spectrum was calculated by summing over the frequency bins of the Fourier transform:

$$\Delta f_{rms} = \frac{1}{\sqrt{2}} \sum_{i=1}^{n} |(FFT(\Delta f(t))_i|^2 \tag{7.2}$$

The integrated spectrum for the Quadrupole resonator is shown in Figure 7.3. As we can see, more than 15 Hz rms detuning comes from very low frequency sources (below 0.1 Hz), attributed to LHe pressure fluctuations. Around 80% of the rms detuning comes from the resonance at 100 Hz, the peaks at 10 Hz and around 250 Hz also cause significant detuning.

Looking at the microphonics spectrum alone, does not yet give information on the nature of the disturbance. Two main sources of detuning are:

- External, single frequency noise source coupled to the cavity
- Excitation of a mechanical resonant mode of the cavity, driven by broadband white noise

These two sources may be differentiated, by calculating the autocorrelation function of the detuning signal [69, 68], given by:

$$R_x(\tau) = \langle x(t) \cdot x(t+\tau) = \lim_{T\to\infty} \frac{1}{T} \int_0^T x(t) \cdot x(t+\tau) dt \tag{7.3}$$

The autocorrelation is a measure of the correlation of a measured sample with itself, after a certain time shift. One can calculated the expected autocorrelation response of a damped harmonic oscillator. If the oscillator is driven by an external sinusoidal driving force with frequency ω_{drive}, the autocorrelation function will be of the form $\cos(\omega_{drive}\tau)$. If a mechanical resonance is excited by white noise, the autocorrelation will be of the form $\cos(\Omega_n\tau) \cdot e^{-\frac{t}{\tau_n}}$, where Ω_n is the mode frequency and τ_n is the decay time constant, a typical values being some 100 ms for elliptical cavities. For the detuning sample studied, no decay of the autocorrelation function was observed, indicating the presence of a sinusoidal driving force.

During the commissioning run, an interesting event was observed on several occasions. Above a threshold field of around 30 mT , the field would be stable for several tens of seconds, followed by several seconds of increasing detuning and subsequent field breakdown as the phased-lock loop lost the lock on the resonance frequency. Such an event is shown in Figure 7.4. The fact that these kind of events occurred consistently at same field level, with lower fields being completely stable and higher fields being unobtainable, suggest that modulations on the RF field directly might be the source of the microphonics. The same event is shown in a spectrogram in Figure 7.5, which shows how the frequency components of the detuning signal change with time.

After the commissioning run, much research was made into finding out the nature of the field limiting microphonics. The mechanical modes of the Quadrupole Resonator were measured with a geophone (see Section 7.1.2 and Appendix C), with the result that several modes existed right at around 100 Hz. A 100 Hz component was also found in some of the electronic devices in the phased-lock loop leading to a slightly modulated RF input signal. Thus, the small 100 Hz modulation of the RF signal led to a resonant excitation of a vibrational mode of the niobium rods by dynamic Lorentz forces. For the subsequent runs, the electronic components with the 100 Hz were replaced and the input coupling increased to increase the cavity bandwidth. Even though microphonics remained a major disturbance, the field limitations were now caused by the typical high field effects, discussed in Section 7.2.

7.1.2 Geophone Modal Analysis

For further mechanical analysis, the mechanical modes of the QPR were measured in the warm state with a geophone [70, 71, 72]. A geophone consists of a spring mounted coil with an iron core rigidly mounted to the outer case. A schematic diagram is shown in Figure 7.6, together with a photo of the geophone mounted to the QPR. Vibrations passed onto the outer case cause a relative motion between the coil and iron core. The induced voltage is the measurement signal and proportional to the relative movement of the iron core and the coil. By integrating the measurement signal and taking the Fourier transform, one obtains the microphonic spectrum of the cavity. A more detailed discussion about geophones is given in Appendix C

The sensitivity of the geophone is highly frequency dependent and is measured by exciting it with white noise during a calibration measurement.[1] The fourier spectrum of the measurement signal is shown in Figure C.3. Any data measured, has to be subsequently

[1]The measured sensitivity spectrum is shown in the Appendix C.

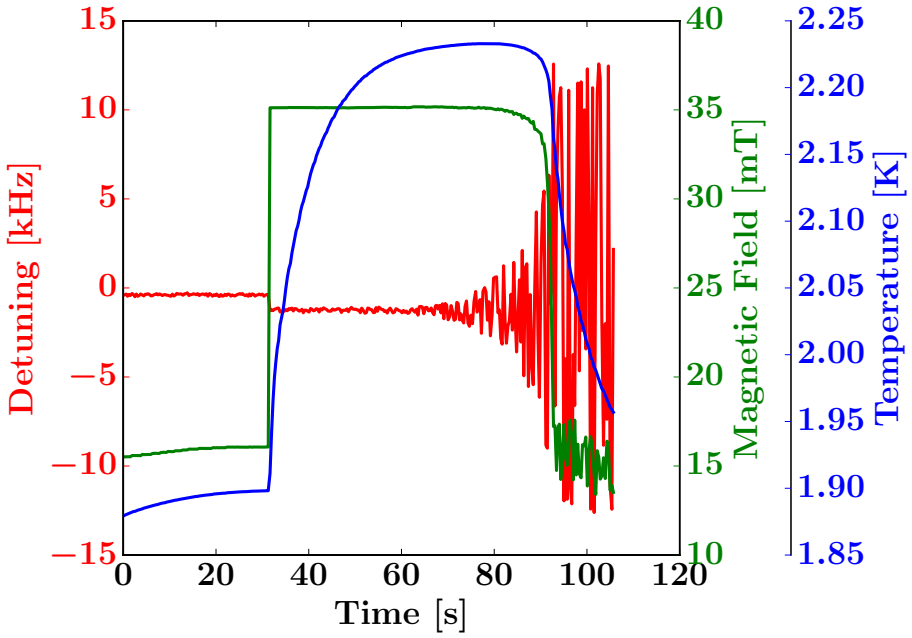

Figure 7.4: Slow, runaway build up of microphonics with subsequent loss of field due to the finite bandwidth of phased-lock loop. The temperature of the sample shows that a runaway temperature increase is not the source of this event.

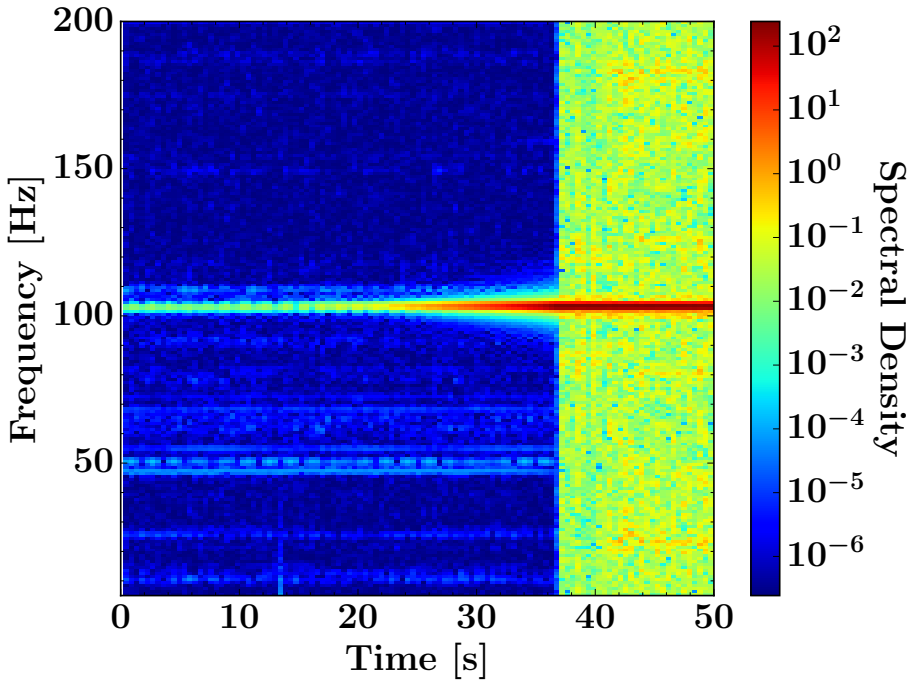

Figure 7.5: Spectogram, showing the change of the frequency components of the detuning signal during the event shown in Figure 7.4.

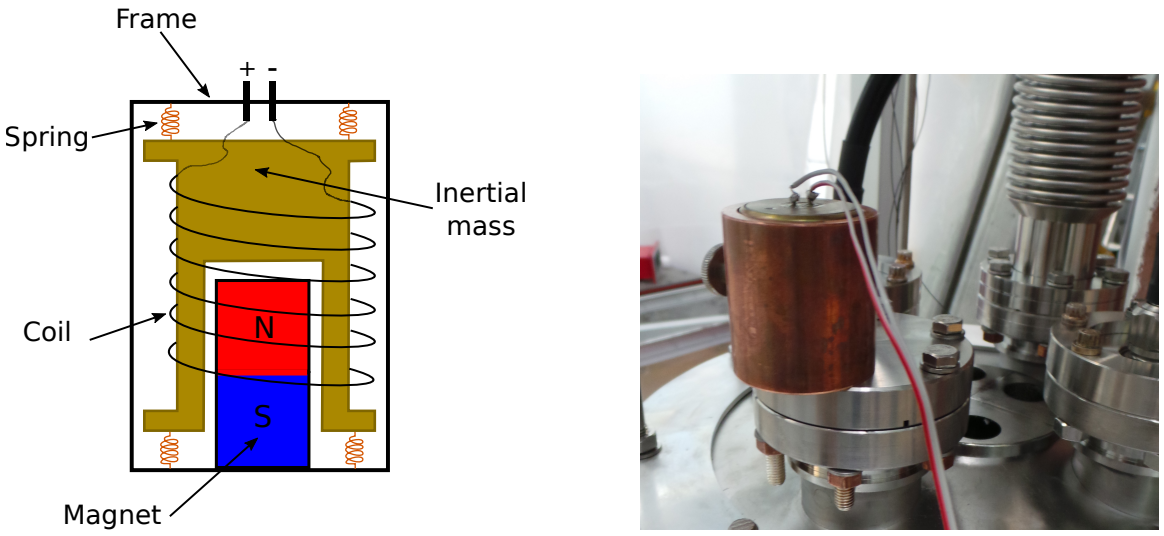

Figure 7.6: Left: Schematic drawing of a geophone. Right: MXVE Geophone mounted to the auxillary port of the QPR on the top plate

normalized to the white noise spectrum, if one wants to make meaningful comparisons of the amplitude of the frequency components.

After mounting the geophone to the QPR, mechanical vibrations were induced using a small rubber hammer. Inducing the vibrations at different locations, allowed a coarse localization of the mechanical modes. In Figure 7.7, two parts of the recorded spectra are shown. One can see that resonances are excited differently, depending on whether the mechanical activation occurred on the cavity side walls or at the top plate close to the niobium rods. An important result is that several peaks are visible around 100 Hz, the modes coupling both to side walls and niobium rods.

7.2 Field limitations of SRF cavities

Various mechanisms, related to either the surface electric or magnetic field, can fundamentally limit cavity performance. The most common limitations will be presented in this section, together with an analysis of their potential and actual impact on the Quadrupole Resonator.

7.2.1 Field Emission

Field emission is one of the most common limitations in superconducting cavities. It is a quantum mechanical effect, caused by high surface electric fields, which allows bound electrons to tunnel through the potential barrier, the height of which is the work function of the material.

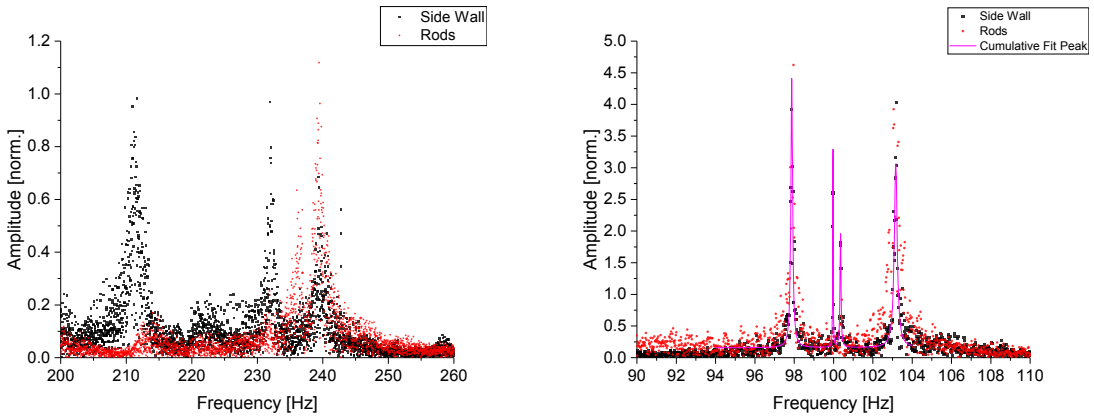

Figure 7.7: Two parts of the frequency spectrum of the QPR measured with the geophone. Left: Changing the position of the mechanical stimulus changes the response. Right: Peaks around 100 Hz

The tunnelling current for a DC field was found by Fowler and Nordheim [73] to be:

$$J_{FN} = \frac{a\beta^2 E^2}{\Phi} \exp \frac{-b\Phi^{3/2}}{\beta E} \tag{7.4}$$

where E is the applied surface electric field, Φ is the work function of the material and β is the geometric field enhancement factor, which can take on values between 50 and 1000 when particulates with rough edges attach to the cavity surface. The constants in Equation 7.4 are $a = 1.54 \cdot 10^{-6}\,\mathrm{AeV/V^2}$ and $b = 6.83 \cdot 10^3\,\mathrm{V}/\mu\mathrm{eV}^{-3/2}$.

From Equation 7.4 we see that the tunnelling current is expected to increase exponentially with applied electric field. Free electrons generated by field emission will be subsequently accelerated by the RF field before hitting a cavity wall. The acceleration causes RF power to be lost proportional to the tunnelling current, hot spots caused by the electrons can further increase the losses. Typically, field emission leads to an exponential decrease of the quality factor at high fields.

Field emission is best prevented by keeping the cavity surface free of particulates. Particles with a size of only some μm can already cause severe degradation of cavity performance due to an increased field enhancement factor β. For this purpose, it has become standard procedure to perform a high-pressure rinse on superconducting cavities [30]. Particulates causing field emission can be processed away using RF power, significantly changing performance during a cooldown cycle. A detailed review of the field emission and processing phenomena is given in [17].

For the QPR, we expect field emission to be less critical than for elliptical cavities, as the peak electric fields are comparatively low. The factor E_{pk}/B_{pk} is 13.5 MV/m/100 mT

compared to 47 MV/m/100 mT for TESLA type cavities [5]. However as the QPR needs to be opened on a regular basis to exchange sample and the geometry making efficient high-pressure rinsing difficult, electron emission at medium fields is a possibility. If field emission is present in the QPR, there are two distinct scenarios:

- The electron trajectories do not cross the sample. As the sample measurement does not rely on the quality factor of the resonator, no measurement error is induced. Field emission might well limit the obtainable field levels however.
- The emitted trajectories hit the sample. In this case, the power dissipated by the electrons will be included in the measurement. As the losses are caused by external electrons and are not intrinsic losses of the material, the surface resistance will be grossly overestimated.

7.2.2 Superconducting Quench

The ultimate field limit in an SRF cavity is given by the superheating field H_{SH}, which is the highest field for which the superconducting state is meta-stable (see Section 2.2.3). Once this field level has been reached, the cavity turns normal-conducting and within the time order of $\sim 10\,\mu$s a significant part of the stored energy will have dissipated in this normal conducting region. Due to the fast nature of this process, this is called a 'quench'.

Often one observes such a quench at fields significantly below H_{SH}. This can have different causes:

- Magnetic quench: Defects in the cavity can lead to areas with a locally decreased critical fields. Once these turn normal conducting, the additional heating caused by the normal conducting area spreads outwards, causing a quench.
- Thermal quench: A local defect with an increased surface resistance leads to a hot spot. Once this hotspot is normal conducting, the entire cavity quenches rapidly.
- Field emission induced quench: In this case, electrons produced by field emission deposit there energy in hot spots that become normal conducting.

One can differentiate between magnetic and thermally induced quenches by noting that in the magnetic case, a quench occurs when a threshold value of the surface magnetic field H_S is reached, while thermally induced quench happen at a critical value of H_S^2. Experiments with multi-cell cavities have been performed, in which two pass-band modes are excited simultaneously [74] allowing to discern between both models. It was found that

neither a 'pure' magnetic or thermal quench is compatible with experimental data, but a combination of both models is required.

The field limit of the QPR is given by a superconducting quench. The peak surface field occurs on the niobium rods, where it is about 10% higher than on the sample. At a peak field of $\sim$ 125 mT (on the sample), a quench is repeatedly identified from the fast collapse of the stored energy in the cavity during the filling period. The quench location is not on the sample, as no temperature spike is measured simultaneously.

7.2.3 Multipacting

Multipacting is the resonant electron discharge, during which an initial seed electron is accelerated by the RF field against cavity wall, creating secondary electrons. If the emission is resonant with the RF fields, this can cause the secondary electrons to be accelerated again and emit further electrons, leading to an exponential growth of the number of electrons. In either case, power supplied to the cavity is dissipated by the electrons, limiting the microwave field to a certain threshold.

There are two methods of preventing multipacting. One is by choosing a geometry for which a resonant acceleration of electrons is not possible or at least unlikely. This can be simulated with a particle tracker solver which is part of advanced RF codes such as CST. The second handle one has on multipacting is the material. The amount of secondary electrons emitted on average, named secondary electron yield (SEY), depends on the initial electron impact energy as well as from the material. For multipacting to persist, the SEY must be greater than one at the impact energy.

In the case of the Quadrupole Resonator, potential locations for multipacting are the narrow gap between sample and rods as well as between the rods at half the vertical height of the resonator, where the magnetic fields disappear. These regions are prime candidates for multipacting, as no magnetic field is present to bend the electrons away from a stationary trajectory. The electric field in such an area can be described by $E = E_0 \sin(\omega t)$ and the equation of motion of an electron is given by:

$$\ddot{x} = \frac{eE_0}{m} \sin(\omega t) \tag{7.5}$$

The multipacting barriers can be approximated analytically, by imposing a boundary condition that emitted electrons reach the other side of the gap at odd integer numbers of the half RF period. Furthermore, the impact energy of the electrons has to be between 100 and 1000 eV, as only in this case more than one secondary electron is emitted on average by a

heat-treated niobium surface [75]. For a gap of length L and order of multipacting n, the gap voltage V is [76]:

$$V = L \cdot E_0 = \frac{4\pi m}{e} \frac{L^2 f^2}{(2n-1)} \tag{7.6}$$

from which the impact energy can be calculated. Between sample and rod, the gap is so narrow that electrons cannot reach dangerous impact energies before hitting the opposing sides. For the case between the rods we have:

Order n	Impact Energy [eV]	E_0[kV/m]	B_{smpl}[mT]
1	2767	241	5.3
2	922	80.5	1.8
3	553	48.3	1.1
4	395	34.5	0.75
15	95.4	8.3	0.18

Table 7.1: Two point multipacting barriers between niobium rods

We see that there are many orders of multipacting producing potentially dangerous electrons. All of these barriers occur at very low fields, for the $n = 2$ case, the peak magnetic field on the sample is below 2 mT.

During commissioning multipacting was repeatedly observed. It did not limit performance however as the barriers could be processed away by applying RF for several hours. As the barriers are all at low field levels, if one fills the cavity sufficiently quickly, there is a high probability that no seed electron to start the resonant process will be present. In general the signature with which one identifies multipacting is a truncated transmitted power level when one sends a rectangular forward power pulse. The clearest evidence found with the QPR is shown in Figure 7.8, where one sees the stored energy spike downwards during the falling edge of an RF pulse.

We can make some estimates of the time scale and the number of electrons in this process. Comparing the multipacting onset (at around 0.7 mT with our analytical calculations in Table 7.1, we will make the assumption that we have multipacting of order 4 between the rods. This corresponds to a gap voltage of $V = L \cdot E_0 = 620\,\mathrm{V}$. At the onset level, we have a stored energy remaining in the cavity of $\sim 10\,\mu\mathrm{J}$ which decays faster than the $20\,\mu$s time resolution of the power meter. If we assume that the entire process takes $1\,\mu$s the power dissipated by the electrons is $P = \frac{dU}{dt} = 10\,\mathrm{W}$ and we have a multipacting current of $I \approx 15\,\mathrm{mA}$. We can now explicitly calculate the number of electrons in our multipacting current to be $N_E = 0.015\,\mathrm{A} \cdot 6.24 \cdot 10^{18}\,\mathrm{e/s} \cdot \frac{7T_{RF}}{2} \approx 10^9$. The question that remains is how quickly we can create 10^9 electrons from a single seed electron. If we assume a SEY of

1.3, it will need around 80 multiplications, taking around $t = 80 \cdot \frac{7T_{RF}}{2} = 0.67\,\mu$s, consistent with our assumptions.

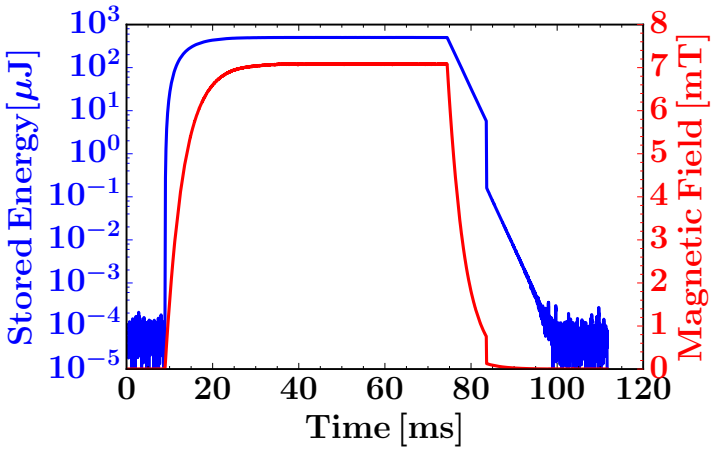

Figure 7.8: Multipacting event seen with QPR

During measurement campaigns, multipacting occurred often as a serious disturbance and a major time sink. During the start of most runs, multipacting would limit the fields to $< 5\,$mT, with an increase in forward RF power not further increasing the field level. Applying RF power continuously would generally slowly raise the field limit, as the RF surface is "cleaned" by the electron bombardment and the SEY is lowered, but this process could take one or two entire days.

Chapter 8

Characterization of Niobium Samples

In this chapter, the results of the RF characterization of two Niobium samples are discussed. Photographs of the two samples studied are shown in Figure 8.1. Both samples were made from bulk niobium, with the same nominal purity, specified as RRR 300. Both samples had the top 150 μm layer removed by chemical etching and were subsequently baked at 600 °C for 12 hours. They differ in two aspects:

- Sample A was made from large grain niobium (the boundaries are visible in the photo), Sample B from polychristalline Niobium.
- Both samples underwent a high temperature bakeout at 600 ° after the BCP, Sample A was subsequently baked at 120 °C for 48 hours. The effects of this low temperature bake were discussed in Section 5.3

The measurements and data analysis to extract key superconductor parameters will be presented. In this chapter the temperature dependence of the surface resistance, penetration depth and critical field are studied, as is influence of trapped magnetic flux. The dependence of the surface resistance on the applied RF field is left for Chapter 9.

8.1 Temperature Dependence of the Surface Resistance

Several key material properties can be extracted from the temperature dependence of the surface resistance. The surface resistance of superconductors increases exponentially with temperature and is often fitted with the Arrhenius expression [77]:

$$R_S(T) = A \cdot \frac{\omega^2}{T} \cdot \exp\left(-\frac{\Delta}{k_B T}\right) + R_{res} \tag{8.1}$$

which is a good approximation in the temperature range of $T < T_C/2$, where the energy gap can be considered to be constant. For cavity tests, with the temperature range being

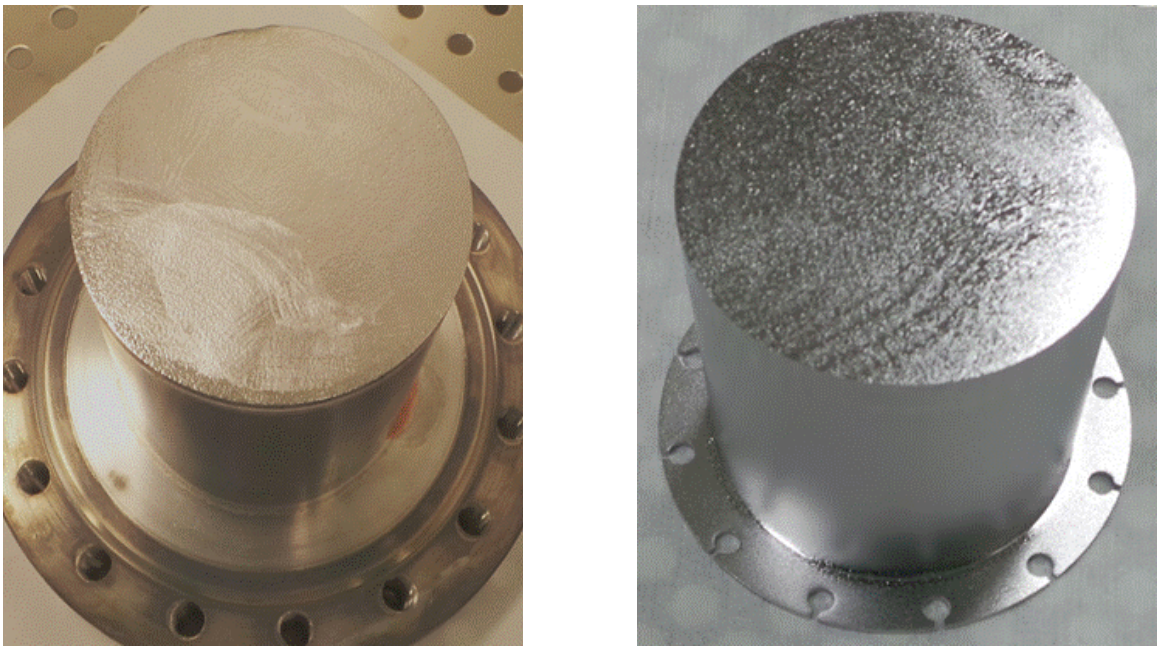

Sample A Sample B

Figure 8.1: Photos of the two Niobium samples

limited to the boiling temperature of helium 4.2 K or even the Lambda point (2.17 K), this restriction is not a concern. For measurements with the Quadrupole Resonator, measurements above $T_C/2$ are possible, but should not be included into the Arrhenius fit. Fitting data with the Arrhenius expression yields the superconducting energy gap as well as the residual resistance.

The surface resistance against temperature data can also be fitted using BCS theory using Halbritter code, which was already introduced in Section 2.2.2. To calculate a single value of $R_{BCS}(T, T_C, f, l, \Delta, \lambda_0, \xi_0)$, around two seconds are required for each call on a standard PC. To speed up the fitting process, a large lookup table was created with λ_0 , ξ_0 and T_C being fixed to literature values and the frequency to the measurement frequency (here 416 MHz). Before fitting data, this table was loaded and interpolated, rapidly speeding up the process.

Figure 8.2 shows the surface resistance of both samples measured against temperature, together with the Arrhenius and the BCS fits. Both models can accurately describe the data below $T_C/2$, above which only the numerical theory provides a good fit. The extracted parameters are shown for both samples in Table 8.1. We see that for the energy gap Δ, the values from the Arrhenius and the BCS match nicely for Sample A and are just outside the 90% confidence interval for Sample B. The large errorbars on the residual resistance

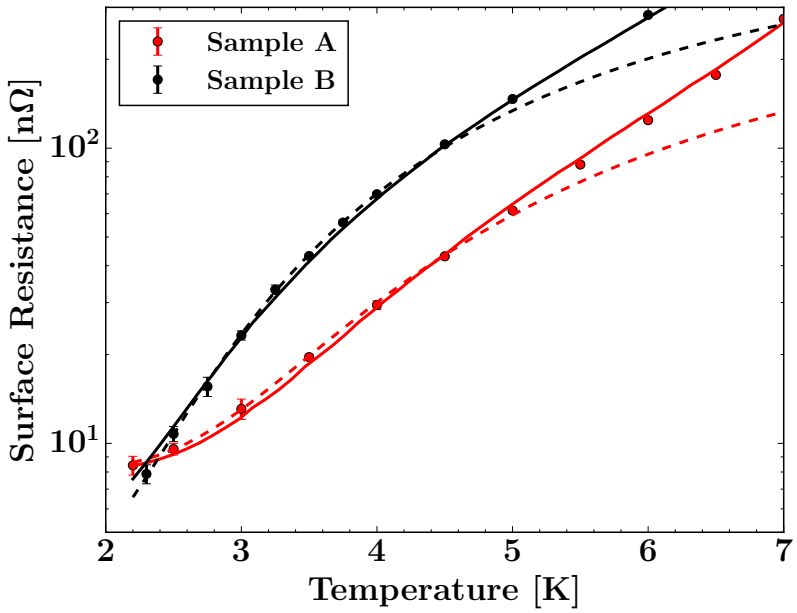

Figure 8.2: Surface resistance against temperature measurement at 416 MHz. At low temperatures the Arrhenius equation (dashed line) is sufficient for fitting the data, above $T_C/2$ numerical BCS theory is required, indicated in the continuous line.

	Fit	Δ/k_BT_C	R_{Res} [nΩ]	l [nm]	A [kΩ · Ks^2]	R^2
Sample A	Arrhen.	$2.25^{+.069}_{-.022}$	$7.94^{+0.62}_{-0.81}$		$15.4^{+8.61}_{-5.44}$	0.9999
	BCS	$2.18^{+.013}_{-.009}$	$8.98^{+0.65}_{-0.52}$	$14.5^{+3.10}_{-2.57}$		0.997
Sample B	Arrhen.	$1.95^{+.082}_{-.016}$	$3.456^{+1.24}_{-1.49}$		$23.4^{+5.24}_{-5.87}$	0.99957
	BCS	$1.778^{+.039}_{-.034}$	$4.53^{+1.31}_{-1.51}$	$24.33^{+14.82}_{-6.41}$		0.9998

Table 8.1: Fit parameters from the RvsT data for Sample A and B

R_{Res} is somewhat unexpected, a result of the large temperature interval reducing the relative weight of the low temperature data.

Compared to cavity results [61, 78], the energy gap for Sample A is significantly increased. The 120°C bake has been shown to slightly increase the energy gap after high temperature heat treatments, but a value of $\Delta/k_BT_C > 2$ is atypical for Niobium. The electron mean free path is significantly lower for Sample A than for Sample B, even though the original material was specified to the same purity (RRR 300). Here again, the difference comes from the additional 120°C baking procedure performed on Sample A, which is known to reduce the electron mean free path within the outer layer due to a modified oxide structure [61].

8.1.1 Fit Parameters Error

In Table 8.1, all fitted parameters were given with a 90% confidence interval, calculated with the statistical method of bootstrapping [79]. For this method, an initial fit is created by finding the parameter vector $\boldsymbol{p}$ which minimizes the sum of the squared errors:

$$\sum_{i=0}^{N} [y_i - f(\boldsymbol{x}_i, \boldsymbol{p})]^2 \tag{8.2}$$

where y_i are the measurement values and x_i the independent variables, in our case the surface resistance and the temperature respectively. After the initial fit,[1] residuals were calculated for each of the N data points as $r_i = y_i - f(\boldsymbol{x}_i, \boldsymbol{p}_{fit})$. In the next step, a large number ($M = 1000$) of artificial data sets were created by adding randomly selected residuals to each data point, the residuals being drawn with replacement. The model is then fitted to each of these test data sets, resulting in a statistical distribution of fit parameters shown in Figure 8.3. From these distributions, confidence intervals of the fit parameters can be easily obtained.

An interesting result was found when plotting the histograms of the fit parameters for the Sample A data, shown in Figure 8.3. For the mean free path, one can see that the result clearly looks like it is drawn from two normal distributions. This means that the mean free path of 24 nm (the mean of the bootstrap-ensemble) is not the maximum likelihood estimate, which would be around 21 nm.

To further understand this result, an artificial R vs T data set was created, using the Halbritter code with similar parameters to those of our samples. A small Gaussian error with was added and the bootstrapping analysis detailed earlier was applied. The resulting histograms again showed two peaks and were very similar to those of Figure 8.3.

Finally, we plotted the fit error on a 2D colormap, for a wide range of Δ and l, see Figure 8.4. One sees, that there is strong correlation between the fit parameters and that the relationship is non-linear. Slight perturbations in the data, produced in this case by the bootstrapping method, lead to two parameter distributions centered around two separated (Δ,l) minima.

8.2 Penetration Depth Measurement

The penetration depth is the characteristic length with which a magnetic fields decays inside a superconductor. With the Quadrupole Resonator, the penetration depth of the sample can

[1] Fits were performed using Python's open source library Scipy. The function used was optimize.leastsq, which can calculate nonlinear minimization problems based on the Levenberg-Marquardt-Algorithm [80].

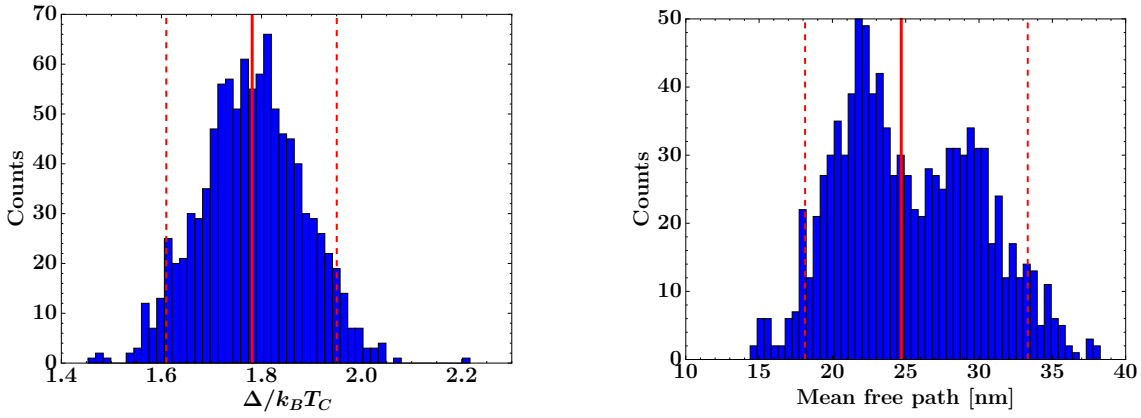

Figure 8.3: Histogram of the fit parameters from the boostrapping data sets. The solid red line represents the mean of the fit parameter and is used as the best estimate, the 90% confidence interval is marked with the dashed line.

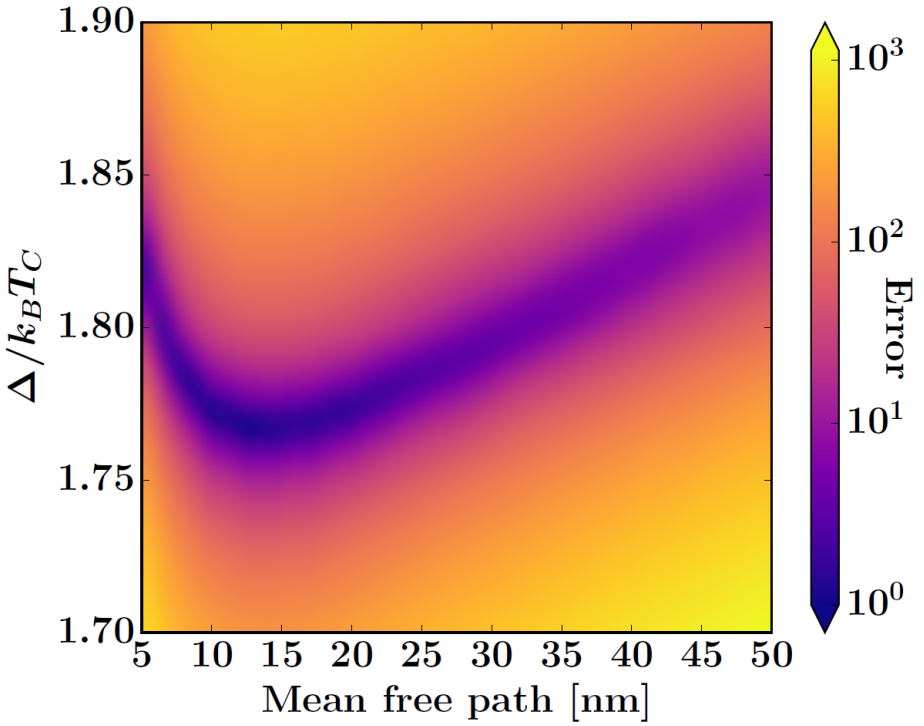

Figure 8.4: Normalized squared error of the BCS fit to the data shown in Figure 8.2. The measurement is much more sensitive to the energy gap than to the mean free path, the correlation between the two parameters is non-linear.

be determined by measuring the change in resonance frequency as the sample temperature is varied. The measurement principle relies on Slater's theorem, which gives a general relationship between the change of resonance frequency to a change in stored energy.

$$\frac{\Delta f}{f} = \frac{\Delta U}{U} \tag{8.3}$$

By heating up the sample, the penetration depth will increase, increasing the electromagnetic volume and changing the stored energy. Slater's theorem at a perfectly conducting boundary can be written as [81]:

$$\begin{aligned} \frac{\Delta U}{U} &= \frac{-\int_{Vol}\left(\epsilon_0|E|^2 - \mu_0|H|^2\right)dV}{4 \cdot U} \\ &= \frac{\Delta\lambda \cdot \int_{Smpl}\left(\epsilon_0|E|^2 - \mu_0|H|^2\right)dA}{4 \cdot U} \\ &\approx -\frac{\Delta\lambda \cdot \int_{Smpl}\mu_0|H|^2 dA}{4 \cdot U} \end{aligned} \tag{8.4}$$

In the last equation, the term for the electric density was omitted, due to it being about two orders of magnitudes lower than the magnetic density for our particular geometry. We can now combine the result from Equation 8.4 with the definition of the geometry factor for the QPR, to directly relate the change in measurement frequency with a change in penetration depth.

$$\Delta\lambda = \lambda(T) - \lambda_0 = -\frac{G_{Smpl}}{\pi\mu_0 f^2}\Delta f \tag{8.5}$$

The effective penetration depth at $T = 0$ can now be extracted by fitting the Gorter Casimir expression to the data:

$$\lambda(T) = \frac{\lambda_0}{\sqrt{1 - (T/T_C)^4}} = \frac{\lambda_L\sqrt{1 + \frac{\xi_0}{l}}}{\sqrt{1 - (T/T_C)^4}} \tag{8.6}$$

The Gorter Casimir expression describes the temperature dependence of the penetration depth. Figure 8.5 shows the effective penetration depth, calculated using both numerical BCS theory and the Gorter Casimir expression for two different purities. One sees, that the Gorter Casimir expression provides a reasonable estimation of the BCS result, particularly in the dirty limit.

Both methods provide a good fit to the data, as shown in Figure 8.6. The results for both sample are shown in Table 8.2. Note, that if the effective penetration depth is close to

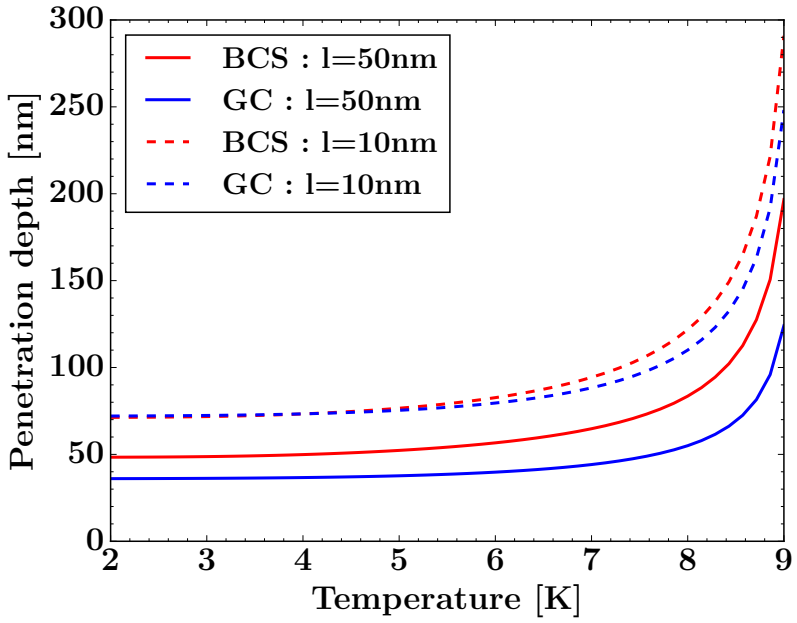

Figure 8.5: Penetration depth of Niobium, calculated using the Halbritter code and using the Gorter Casimir expression. For a local superconductor $\xi \ll \lambda$, the approximation holds to a high degree, for a cleaner superconductor there are significant deviations.

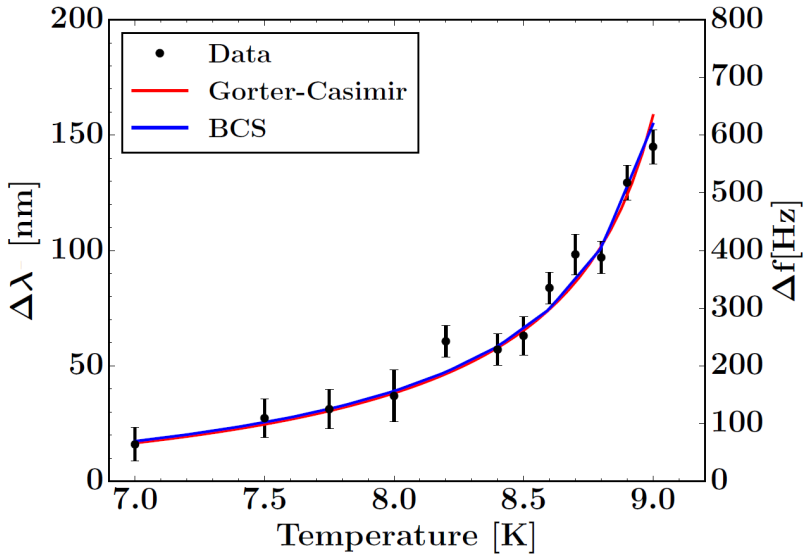

Figure 8.6: Penetration depth data fitted with BCS theory and Gorter Casimir. Both models provide a good fit to the data, the extracted mean free path differs however.

London penetration depth, the error on the calculated mean free path becomes very large. It is thus difficult to differentiate between clean and very clean sample with this measurement.

	Sample A	Sample B
$\lambda(0)_{BCS}$	58.5 nm	45.6 nm
$\lambda(0)_{GC}$	75.3 nm	53.6 nm
l_{BCS}	19.4 nm	80.0 nm
l_{GC}	11.53 nm	32.1 nm

Table 8.2: Results of the penetration depth measurement

8.3 Trapped Flux Studies

Trapped magnetic flux contributes significantly to the residual resistance in superconducting cavities. These additional losses occur as magnetic flux lines present during the superconducting transition are not fully expelled from the material entirely as predicted by the Meissner effect, but may remain trapped by pinning centers with efficiencies of up to 100 % [82]. For niobium cavities with RRR 300 material, the rule of thumb for losses due to trapped flux is given by $R_{\mathrm{tf}} \approx 3\,\mathrm{nOhm}/\mu\mathrm{T}$ for 1.3 GHz cavities, already making efficient shielding of the earth magnetic field a requirement. For niobium doped cavities with a very low electron mean free path, losses due to trapped flux over $R_{\mathrm{tf}} \approx 30\,\mathrm{nOhm}/\mu\mathrm{T}$ have been reported [83].

In a simple model [19], a magnetic field B_{trap} trapped in a superconductor of area A, will form N flux tubes, each carrying the magnetic flux quantum $\phi_0 \approx 2 \cdot 10^{-15}$ Wb:

$$B_{\mathrm{trap}} \cdot A = N\phi_0 \tag{8.7}$$

The cross section of the normal conducting flux tubes is in the order of the coherence length ξ, providing a good estimate of the residual resistance caused by trapped flux:

$$R_0 = \frac{N}{A}\pi\xi^2 R_n = \frac{\pi\xi^2 R_n}{\phi_0} \cdot B_{\mathrm{trap}} \tag{8.8}$$

The sensitivity to trapped flux of a superconductor is defined as the ratio of additional residual resistance to the trapped magnetic field. Our simple model predicts a smaller sensitivity in dirty superconductors, as a small electron mean free path also reduces the effective coherence length. In more sophisticated models, the effect of the pinning centres (which trap the field in the first place) on the motion of the vortices causing RF-dissipation are analysed [84, 83]. It is found that the sensitivity scales with $R_0 \propto 1/\sqrt{l}$ in the clean limit and $R_0 \propto l$ in the dirty limit, with a maximum sensitivity at around $l = 10\,\mathrm{nm}$ for Niobium.

Furthermore the RF frequency plays an important role for the trapped flux losses and investigating $R_{tf}/B_{trap}(f)$ is a direct test to the theory. In the naive model, trapped flux losses

will scale like the normal conducting surface resistance with $\sqrt{f}$. In the model where the losses due to trapped vortices oscillating with the RF field are calculated directly [84], the power dissipated by a single vortex increases with f^2 at low frequencies, before saturating above a threshold frequency.

To study trapped flux effects with the Quadrupole Resonator, a copper solenoid was mounted under the sample with a fluxgate magnetometer placed inside it, as previously shown in Figure 6.4. To perform a field-cooled thermal cycle, the sample was heated above the transition temperature, an ambient field applied and the sample then cooled through the transition temperature before turning off the current passing through the coil. A higher reading of the magnetometer at this point compared with the initial reading are evidence of the incomplete Meissner effect. This process is shown in figure 8.7. Note that the field produced by the heater is also seen by the magnetometer. Apart from the amount of ambient field present during the transition, one can also manipulate the cooling rate with which the sample passes through T_C, which has been shown to influence the residual resistance in superconducting cavities [85].

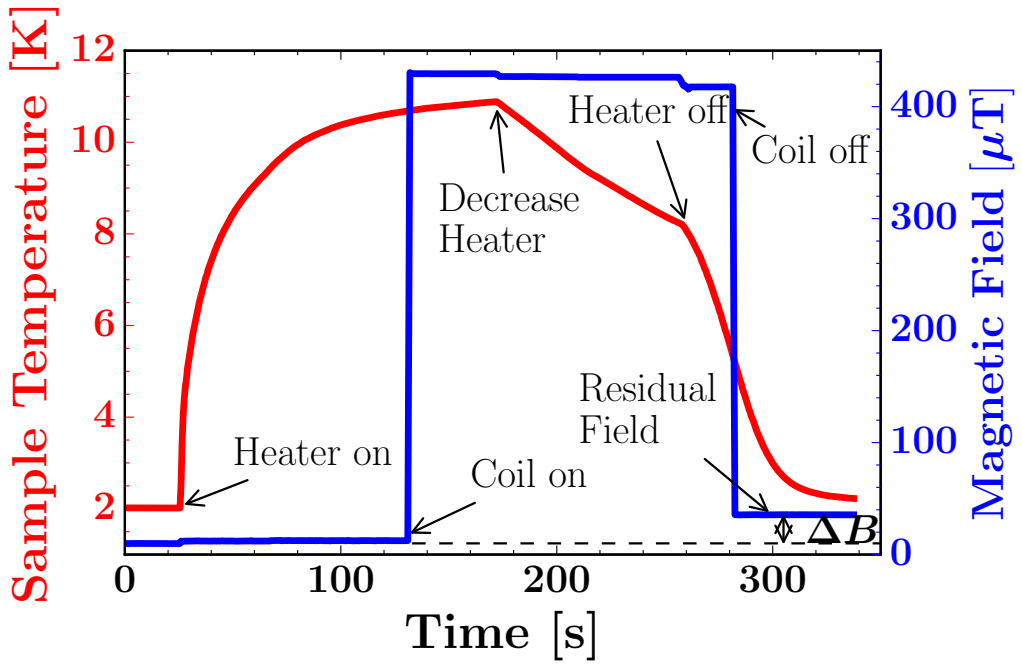

Figure 8.7: Sample temperature and reading of fluxgate magnetometer during thermal cycle with field cooldown

To relate the field measured with the magnetometer with the field on the sample surface, a magnetostatic simulation had to be performed, shown in Figure 8.8, together with a room temperature measurement of the coil. The simulation shows the conditions at which the sample temperature goes through the superconducting transition - the niobium cutoff tube

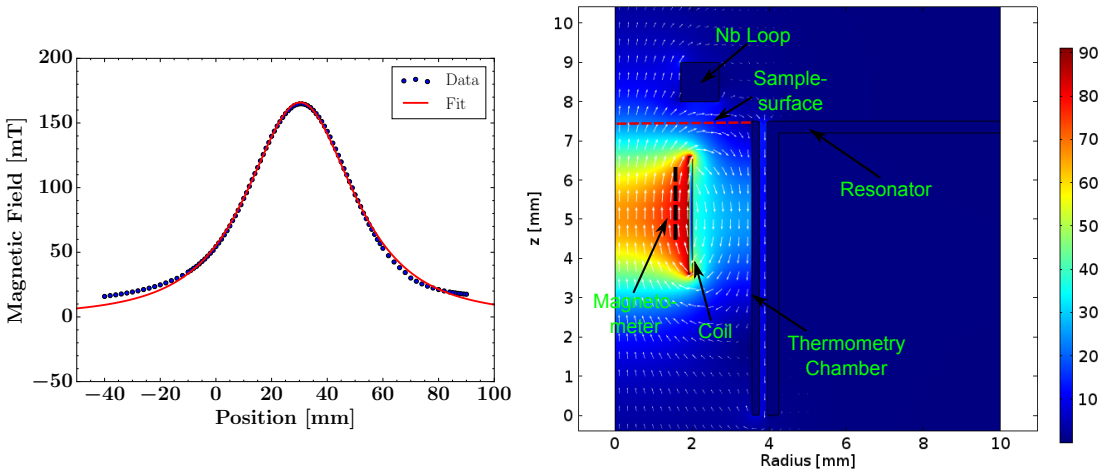

Figure 8.8: Field calibration for trapped flux measurements. Left: Solenoid field mapped out in the warm state. Right: Magnetostatic simulation during the superconducting transition. The niobium cutoff tube, the resonator and the niobium loop are all superconducting and field-free. For the calibration, the mean field at the postion of the magnetometer (black dashed line) is compared with the field across the sample surface (red dashed line).

is thus already below the critical temperature and has no magnetic flux passing through it, assuming full flux expulsion when the coil is turned on. For the calibration, the field at the position of the magnetometer is compared to that on the sample surface, indicated with black and red dashed lines.

Trapped flux measurements were performed only with Sample A. The sample was repeatedly subjected to the same thermal cylcle, being first heated to 11 K, after which the heater was switched off completely. This created the same cooldown condition, the applied magnetic field being the only variable. Figure 8.9 shows the surface resistance, measured at 2.5 K and 20 mT for different trapped fields. The gradient of the fit line determines the trapped flux sensitivity to be $\frac{R_S}{B_{\text{trap}}} = 0.8\,\text{n}\Omega/\mu\text{T}$. This value is very low when compared to cavity measurements at 1.3 GHz with a comparable mean free path and cannot be explained with the $\sqrt{f}$ scaling.

The effect of the cooling rate was also studied. For this, the sample was subjected to a constant ambient field, but the cooling rate at which it passed through the superconducting transition was varied. The results shown in Figure 8.10, unfortunately only a sparse data set could be gathered. The data shows that more magnetic field is trapped during a fast transition, the surface resistance is however larger for the slow cooldowns. Note that due to the geometry of the sample, no thermal currents caused by temperature gradients are expected.

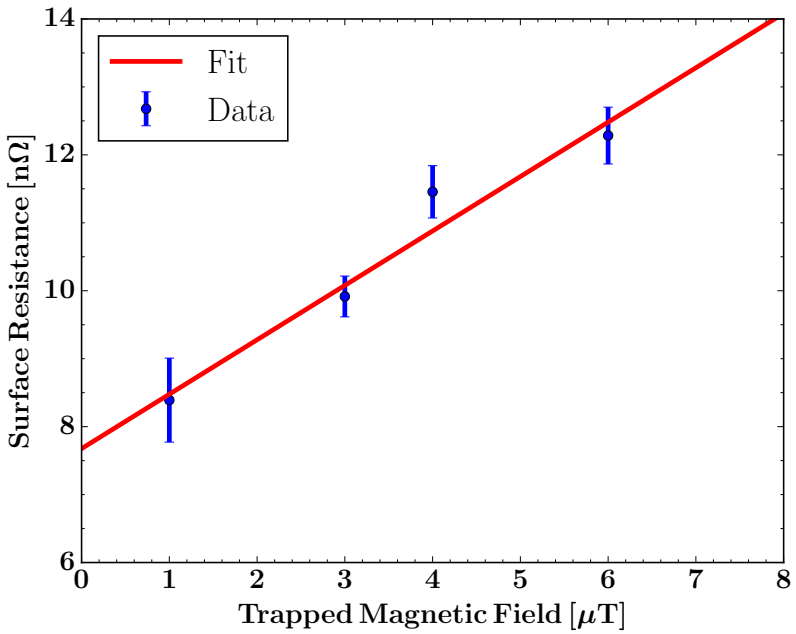

Figure 8.9: Surface resistance at 2.5 K and 20 mT against trapped magnetic field . The trapped flux sensitivity for Sample A was determined to be $\frac{R_S}{B_{\text{trap}}} = 0.8\,\text{n}\Omega/\mu\text{T}$.

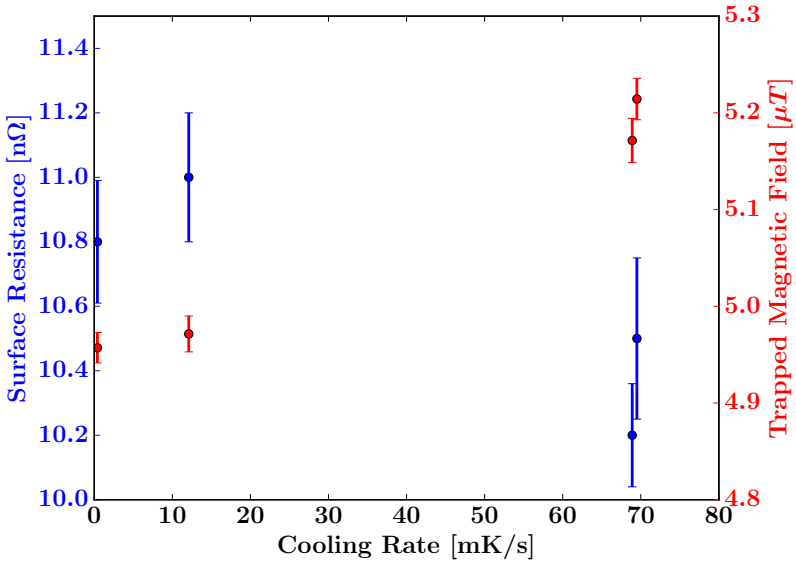

Figure 8.10: Trapped field and surface resistance measured for the same applied ambient field but different cooling rates.

8.4 Critical Field Measurements

In principle one can measure the RF critical field of a cavity by simply increasing the incident power until the cavity quenches. The problem with this approach is that a localized

defect with an increased surface resistance may be heated to temperatures significantly above the helium bath temperature and thus quench at a field leve below the critical field ("thermal quench"). Therefore, detailed studies measuring the critical field of Nb, Nb_3Sn and Pb were performed with very short, high power pulses [25], using a 2 MW klystron. With this setup, the surface fields in the cavity were raised faster than the timescale of heat propagation to reach the critical field before a thermal quench can establish itself.

To understand why so much power was needed, we can look at the equation of the transients fields when the RF power is switched on [4]

$$B(t) = B_0 \left(1 - e^{-t/2\tau}\right) \tag{8.9}$$

where $\tau = {}^{Q_L}/_{\omega}$ is equal to the cavity decay time and B_0 is the highest reachable magnetic field with the RF power, assuming no field limitation. We can thus increase the field ramping rate by two methods:

- Increasing the coupling to the cavity, thus decreasing Q_L and τ. To maintain the same field levels, the product of $Q_L \cdot P$ needs to remain constant.
- Increasing the steady state field B_0, which is proportional to $\sqrt{P}$

Both these options require more RF power, which explains the necessity of the high peak power klystrons.

Compared to regular RF cavities, measuring the critical field with the Quadrupole Resonator requires much less investment. This becomes clear when one considers that for a TESLA cavity, around 250 J of stored energy is required for the surface magnetic fields to reach 200 mT, calculated using the definition of R/Q_0 and cavity data from Table 2.1. For the Quadruple Resonator, the same field can be reached with only 0.2 J, more than three orders of magnitude less.

For the measurements shown here, the RF critical field of the sample was measured by applying short RF pulses with a pulse length of 10 ms and a low repetition rate increasing amplitude. A quench can be identified by the pulse shape of the transmitted power pulse. The sample has to be heated to a temperature higher than the helium bath temperature, to ensure that the quench occurs on the sample and not on the niobium rods. This can be confirmed by observing the sample temperature during the quench.

Measuring the critical temperature for different sample temperatures and assuming the typical $B_C(T) = B_{C0}\left(1 - \left(\frac{T}{T_C}\right)^2\right)$ scaling, one can now plot the critical field against T^2 and extract $B_{C,RF}$ from the y intercept of the fit, shown in Figure 8.11. The critical temperature T_C is the extrapolated x-intercept of this plot. The results for the studied niobium samples

	Sample A	Sample B
$B_{C,RF}$	(231 ± 2.4) mT	(221 ± 3.7) mT
T_C	(9.23 ± 0.04) K	(9.39 ± 0.07) K

Table 8.3: Results for the critical field measurements at 416 MHz. Error shown is calculated from the parameter covariance matrix.

are shown in Table 8.3. The values are significantly higher than the 180 mT of B_{C1}, but are consistent with the superheating field of niobium.

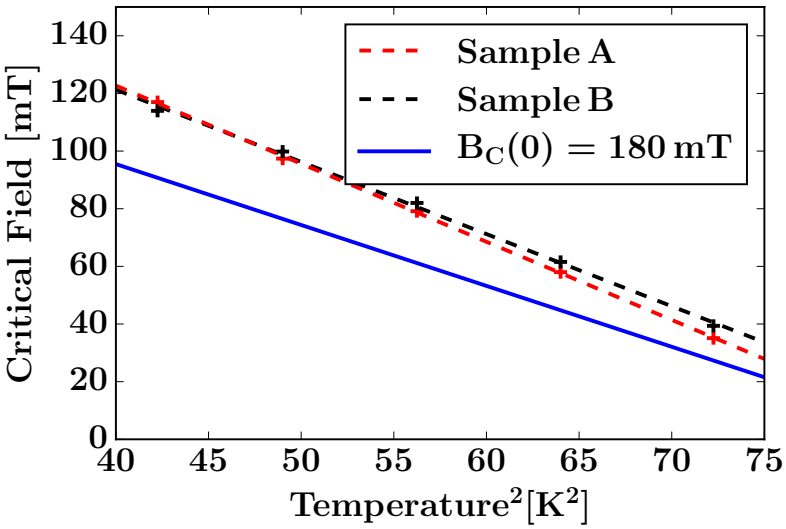

Figure 8.11: Critical Field measurements at 416 MHz. The results for both samples are very similar and show an RF critical field significantly above the value of $B_{C1} = 180$ mT for niobium.

Chapter 9

High RF-Field Studies

The unloaded quality factor Q_0 of superconducting cavities is generally found to be field dependent. For standard niobium cavities which received either a BCP or a EP treatment, a typical Q_0 vs. E_{acc} curve as shown in Figure 9.1 can be divided into three distinct regions:

- Low field Q-rise: At low fields up to 10 mT the quality factors are regularly found to increase with field. This may occur due to subgap states, localized in the oxide layer, reducing the effective energy gap. At higher fields, these quasi-particle states are not occupied, restoring the original energy gap [86].

- Medium Field Q-slope (MFQS): Degradation of the quality factor with increasing field, caused by positive feedback between rising cavity wall temperature and surface resistance [87]. The MFQS is generally represented with the dimensionless parameter $\gamma(T)$:

$$R_s(B) = R_{s,0}\left[1 + \gamma(T)\left(\frac{B}{B_C}\right)^2\right] \tag{9.1}$$

- High field Q-drop: Strong degradation of the quality factor at high RF fields, typically above 100 mT . Cavity measurements with thermometry systems indicate that local hotspots play a role in the high-field Q-drop. The origin of these hotspots may either be a defect with a locally increased surface resistance or losses due to pinned vortices [78, 88]. It was found empirically,that baking the cavities at 120° C for 48 hours would reduce or even eliminate the high field Q-slope [89, 90].

Within the past years it has been found favorable to bake niobium cavities in a controlled nitrogen atmosphere [31]. Cavities treated in this manner reach higher quality factors at intermediate fields, the quality factor systematically rising up until 70 mT. A typical Q_0 vs. E_{acc} curve for nitrogen treated cavity is shown on the right diagram in Figure 9.1.

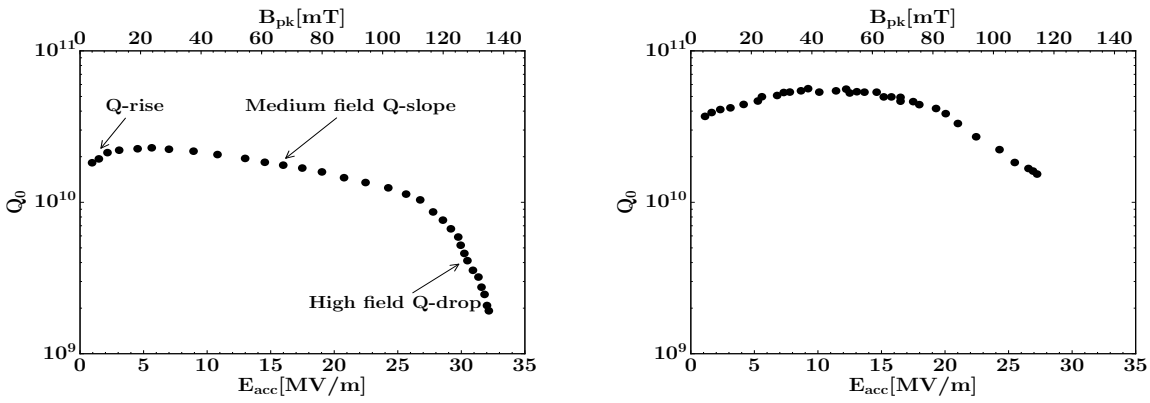

Standard BCP/EP N-doped cavity

Figure 9.1: Plot of Q_0 vs. E_{acc} for a standard BCP/EP treated niobium cavity and for a N-doped cavity [31]. The curve for undoped niobium can be separated into three different regions. For the nitrogen doped cavity, the quality factor increases up to 60-70 mT, reaching higher levels than for undoped cavities.

Note that this curve cannot easily be separated into distinct regions, but seems to follow a gradual trend.

In this chapter we will analyse R_S vs. B_{pk} data measured with the Quadrupole Resonator. Two non-linear models describing the field dependence of the surface resistance will be introduced and used to fit the data. We will start this chapter however, with an analysis of the systematic error involved in calculating a field dependent $R_S(B)$ from a quality factor measurement.

9.1 Comparing Surface Resistance Measurements between Systems

To test superconducting cavities one typically measures the quality factor as a function of accelerating gradient. The quality factor is given by the fraction of stored energy dissipated in the cavity walls per oscillation period and can be calculated with equation 9.2.

$$Q_0 = \frac{\omega U}{P_{Dis}} \tag{9.2}$$

Here, P_{Dis} refers to the power dissipated in the cavity walls, given by:

$$P_{Dis} = \frac{1}{2\mu_0^2} \int_{Surf} R_S(B)|B|^2 dA \tag{9.3}$$

For studying the superconducting material however, the surface resistance as a function of magnetic field is more interesting. The accelerating gradient can easily be converted to

the peak surface magnetic field. If one then takes the R_S term outside of the integral in the equation for dissipated power, one can define a geometry factor which relates quality factor and surface resistance.

$$G = \frac{2\omega U}{\int_{Surf} |H|^2 dA} = \frac{\mu_0 \omega \int_{Vol} |H|^2 dV}{\int_{Surf} |H|^2 dA} = Q_0 R_S \tag{9.4}$$

The last step here is an approximation, unless the surface resistance has no field dependence or the surface magnetic fields are perfectly homogeneous. This approximation error was studied by calculating the expected quality factor $Q_0(B_{\mathrm{pk}})$ for various types of RF cavities, assuming a known surface resistance function $R_S(B)$. For this, the dissipated power needs to be calculated explicitly. For an elliptical cavity with rotational symmetry, one can express Equation 9.3 as a line integral:

$$P_{Dis} = \frac{1}{2\mu_0^2} \int_0^L 2\pi r(z) R_s(B(z)) B(z)^2 \cdot dz = \frac{\pi \cdot \Delta z}{\mu_0^2} \cdot \sum_i r_i R_s(B_i) B_i^2 \tag{9.5}$$

Here, $r(z)$ is the cavity wall and $B(z)$ the magnetic field profile shown for two typical cavities in Figure D.1.

Using the geometry factor, $R_S^{meas}(B_{\mathrm{pk}}) = G/Q_0(B_{\mathrm{pk}})$ was then calculated and compared to the input function $R_S(B)$. The analysis was performed for two elliptical cavities (TESLA and ERL-type), an idealized half-wave-resonator and two cavities for sample testing, the Quadrupole Resonator and a TE_{011} cavity.

In Figure 9.2, $R_S^{meas}(B_{pk})$ is plotted assuming a quadratic dependence of the surface resistance, which is motivated in various mid-field Q-slope models [87]. We see that while the elliptical cavities are fairly accurate, the QPR and HWR distort the $R_S(B_{pk})$ curve significantly, causing relative errors of up to 30 % at high fields. That the error is largest for these cavities is to be expected, as they have particularly inhomogenous magnetic field distributions.

For Figure 9.3 we assumed a surface resistance with a minimum at intermediate fields, similar to the results found with N-doped niobium cavities. Again we observe that the elliptical cavities follow the material properties closely. Half wave resonators and the QPR not only have different Q-slopes, but the minimum of the measured surface resistance is shifted significantly.

This shows, that naive calculations of $R_S(B_{pk})$ can produce large systematic error and will cause different cavities to produce different results for identical material. To fit different $R_S(B)$ models to cavity data it is therefore necessary to use the information of the magnetic

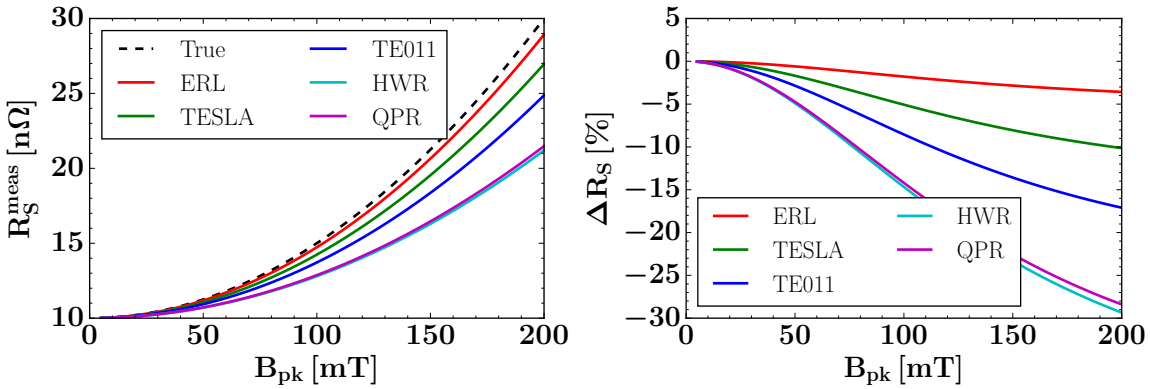

Figure 9.2: Simulated surface resistance measurements using different cavities and a constant geometry factor. The 'true' surface resistance has the form of $R_S(B) = R_0 + \alpha B^2$. Absolute values are shown in the left, percentage error are shown in the right plot.

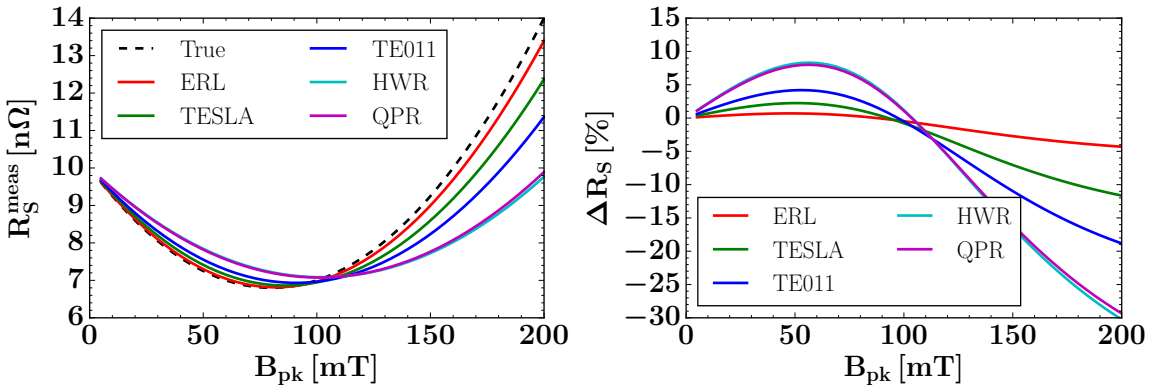

Figure 9.3: Simulated surface resistance with a minimum resistance at intermediate fields. Not only do the slopes change, the field at which the minimum resistance occurs is also shifted significantly

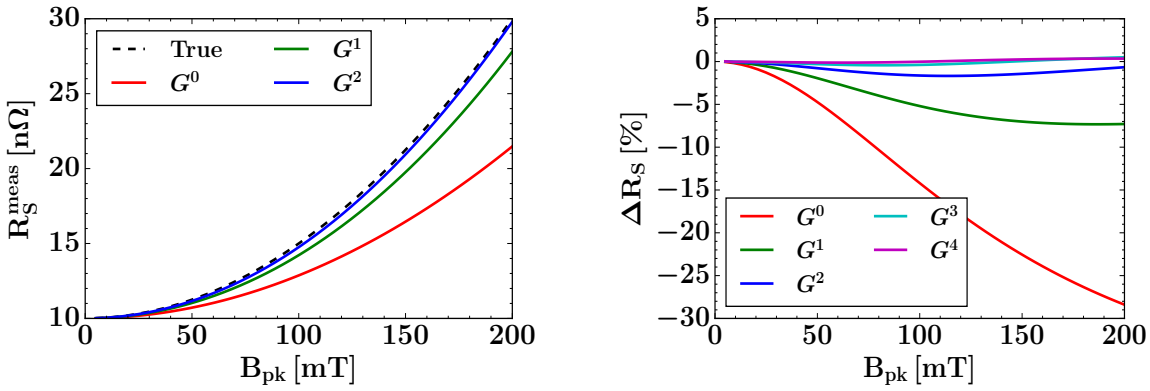

Figure 9.4: Correction using the field dependent geometry factors on calculated results using the field distribution of the Quadrupole Resonator. Only a few iterations are required to eliminate the error caused by the inhomogeneous field distribution.

field distribution within the cavity. Using an iterative method, a field dependent geometry factor can be calculated which eliminates the error:

$$
\begin{aligned}
R_{S,0}(B) &= \frac{G_0}{Q_0(B)} \\
G_1(B) = Q_{calc}(R_{S,0}) \cdot R_{S,0} \quad &, \quad R_{S,1}(B) = \frac{G_1(B)}{Q_0(B)} \\
G_2(B) = Q_{calc}(R_{S,1}) \cdot R_{S,1} \quad &, \quad R_{S,2}(B) = \frac{G_2(B)}{Q_0(B)} \\
&\vdots
\end{aligned}
\tag{9.6}
$$

Here, $Q_0(B)$ is the initial measurement and G_0 is the geometry factor computed with Equation 9.4. Using the first estimate of the surface resistance ($R_{S,0}$), an expected quality factor is calculated, using Equations 9.2 and 9.3[1]. A field dependent geometry factor is then computed and the surface resistance results are updated. The updated results are used to compute a new geometry factor, and so on. In Figure 9.4, the result of such an iterative computation is shown, using the example of the Quadrupole Resonator and a quadratically increasing surface resistance. Only a small number of iterations is required to converge on the correct result. The same behavior was also observed for the parabolic shaped surface resistance.

Now that we have shown that the iterative approach converges towards the true result under 'ideal' circumstances, the next step was applying the method to experimental data.

[1]How to calculate the dissipated power P_{Dis} differs for the individual cavities, for eliptical cavities and the half wave resonator it is shown in Appendix D. For the QPR, the surface fields of the sample are exported from CST directly.

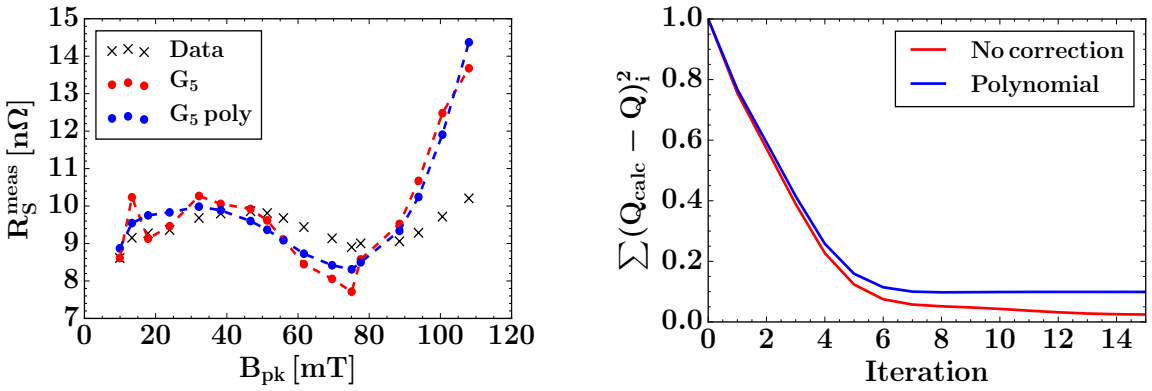

Figure 9.5: Left: Actual measurement data corrected with the field dependent quality factor. Applying only the iterative calculation detailed in Equations 9.6 leads to overfitting and a distorted $R_S(B)$ curve (red). Fitting a third degree polynomial through G_i at each iteration produces the blue curve. Right: The squared error is continually reduced with every iteration but reaches a plateau around G_5.

Unlike the computational results shown earlier, there is now measurement error and uncertainty about the exact field distribution to consider.

In Figure 9.5 exemplary results are shown for data from Sample A at 2.5 K. The original data, computed with constant geometry factor are shown in black. The red line shows the results after five iterations of applying Equations 9.6. One sees that the data has become severely distorted, the algorithm is clearly not converging towards the correct result. It is however reducing the rms-error of the data, as shown in the plot on the right side. As a possible method to avoid this overfitting, a third degree polynomial was fit through the geometry factor at each iteration, producing the blue results. Even though this method does not reduce the error quite as well, it produces a much smoother curve for $R_S(B)$. There is however the concern, that a bias may be introduced by the choice of the function with which the geometry factor is fitted.

For this reason, when surface resistance models are fit to experimental data for the remainder of the chapter, the data was not pre-processed with the iterative method laid out in this section. Instead, the quality factor data is fitted directly, using an explicit calculation of the dissipated power which includes the field distribution. This has the advantage that no bias is introduced by the choice of an arbitrary fit function. The disadvantage is that it is computationally more demanding.

9.2 Surface-Impurity Model

The surface-impurity model does not require modifications to the BCS theory and can explain both medium field Q-slope as well as Anti-Q-slope [91]. The model posits a non-uniform dirty surface on top of a lower clean bulk material. As the penetration depth increases with applied magnetic field due to pair-breaking, the effective electron mean free path probed by the RF-field will also be field dependent. These two features give rise to a field dependent surface resistance, due to the m.f.p dependence discussed earlier in Section 2.2.2.

The magnetic field dependence of the penetration depth in s-wave superconductors is given by [92]:

$$\Delta\lambda_L(H,T) = \lambda_L(0,T)\left[1+\zeta(T)\left(\frac{H}{H_C}\right)^2\right] \tag{9.7}$$

This dependency is not used explicitly however in [91], it is convoluted with the impurity depth profile to define a effective penetration depth l_{eff}, given by:

$$l_{eff} = l_d + l_c \mathrm{erf}(\alpha B^{\beta}) \tag{9.8}$$

where *erf* is the error function, l_d and l_c denote the mean free path of the dirty and the clean parameters and α and β are left as free parameters that determine the impurity profile.[2] Using equation 9.8 and standard BCS theory (Halbritter code) for $R_{BCS}(l_{eff},...)$, we arrive at the desired field dependent surface resistance. In Figure 9.6, a qualitative diagram of the model is shown, together with a plot showing the effective mean free path as a function of magnetic field for various α and β values.

Furthermore, as a part of the residual resistance is expected to originate from normal conducting inclusions in the dirty layer, a reduction of the residual resistance is expected towards higher fields:

$$R_{\mathrm{res}} = R_A - R_B \cdot \mathrm{erf}(\gamma B) \tag{9.9}$$

Here R_A is the residual resistance of the dirty layer, R_B that of the clean bulk material and γ is a free parameter. The total surface resistance described by the surface-impurity model is given by:

$$R_S(T,B) = R_{BCS}(T,T_C,\lambda_L,\xi_0,l_{eff}) + (R_A - R_B \cdot \mathrm{erf}(\gamma B)) \tag{9.10}$$

an expression with which different Q_0 vs. E_{acc} curves can be fit successfully. There are several issues with this model however:

[2] In the original paper [91] and here also, the l_d term is omitted ($l_d = 0$), to reduce the number of fit parameters.

	Temperature	Δ/k_BT_C	l_c [nm]	α	β	R_{res} [nΩ]	R^2
Sample A	2.2 K	1.90	359	$2.94 \cdot 10^{-2}$	1.42	3.46	.001
	2.5 K	2.05	825	$1.73 \cdot 10^{-2}$	1.43	3.62	.29
	3.0 K	1.93	270	$1.1 \cdot 10^{-4}$	1.69	$7.2 \cdot 10^{-7}$	.72
	3.5 K	2.09	610	$1.49 \cdot 10^{-2}$	0.44	$1.3 \cdot 10^{-2}$	.67
	4.0 K	2.12	201	$8.61 \cdot 10^{-3}$	0.72	$1.17 \cdot 10^{-6}$	.62
	5.0 K	2.23	660	$8.61 \cdot 10^{-3}$	0.72	$7.71 \cdot 10^{-6}$	.52
Sample B	2.5 K	1.81	1343	$8.04 \cdot 10^{-4}$	1.52	$8.04 \cdot 10^{-7}$	.971
	2.75 K	1.79	7156	$3.14 \cdot 10^{-4}$	1.17	$1.4 \cdot 10^{-6}$	.929
	3.0 K	1.82	2327	$2.377 \cdot 10^{-3}$	0.87	$6.4 \cdot 10^{-7}$	.950
	3.5 K	1.82	1120	$5.05 \cdot 10^{-4}$	1.55	$2.16 \cdot 10^{-6}$	.925

Table 9.1: Fit parameters for the surface impurity model

- The model relies on a large numbers of parameters. Even if the values of λ_L ,ξ_0 and T_C are fixed to their literature values, seven more parameters are used to fit data with typically rather simple features. For the fits shown in this section, the residual resistance was assumed to be constant, reducing the number of parameters to five (Δ,l_c, α, β, R_{Res}).

- It is unclear, whether the field dependence of the penetration length λ is actually strong enough to significantly change the effective m.f.p. given a realistic impurity distribution within the superconductor. For V_3Si, the effect of increasing a DC field from zero to H_C only changed λ by less than 5% [92].

In Figure 9.7, the surface impurity model is fit to R_S vs. B data taken at different temperatures, for both samples. The extracted fit parameters are shown in Table 9.1. From the bad fit quality and the inconsistent fit parameters, it is clear that the surface impurity model cannot describe the data from Sample A. For Sample B, the model and data provide a much better match. The energy gap is consistently around $1.8 \cdot k_BT_C$, and the bulk mean free path is very high at all temperatures. The residual resistance R_{res} is however zero for all temperatures, incompatible with the R_S vs. T data shown in Section 8.1. Overall, the lack of consistency and the poor fit for Sample A makes us conclude that the surface-impurity model is ill suited to describe our data.

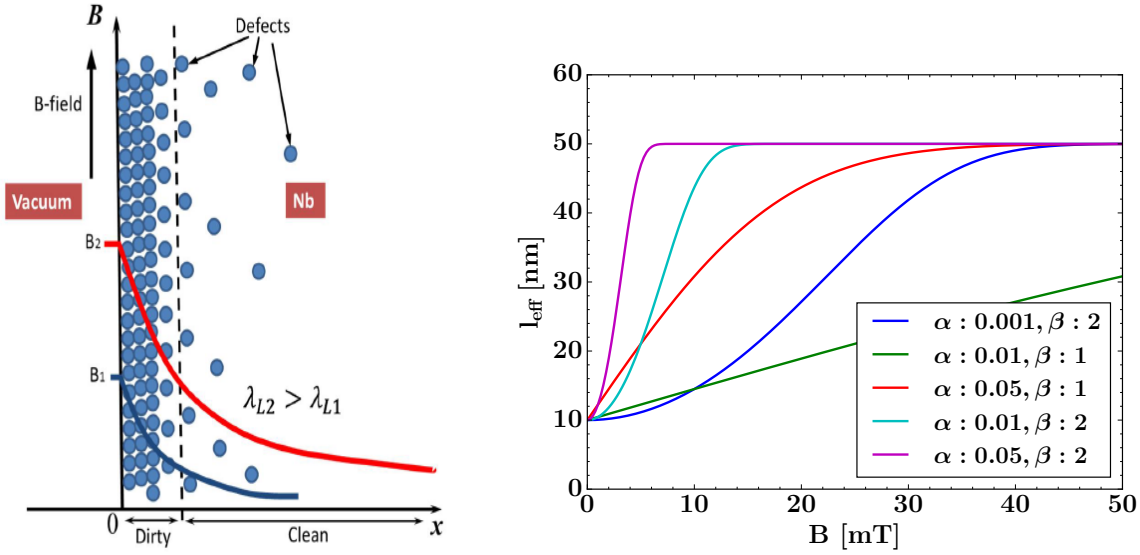

Figure 9.6: Surface impurity model. Left: Simple representation of the surface impurity model [91]. The field dependent penetration depth and the inhomogeneous defect concentration result in a different effective mean free path for B_1 and B_2. Right: Effective mean free path plotted against magnetic field for different (α, β) combinations, calculated for a material with $l_c = 10\,\text{nm}$ and $l_d = 50\,\text{nm}$.

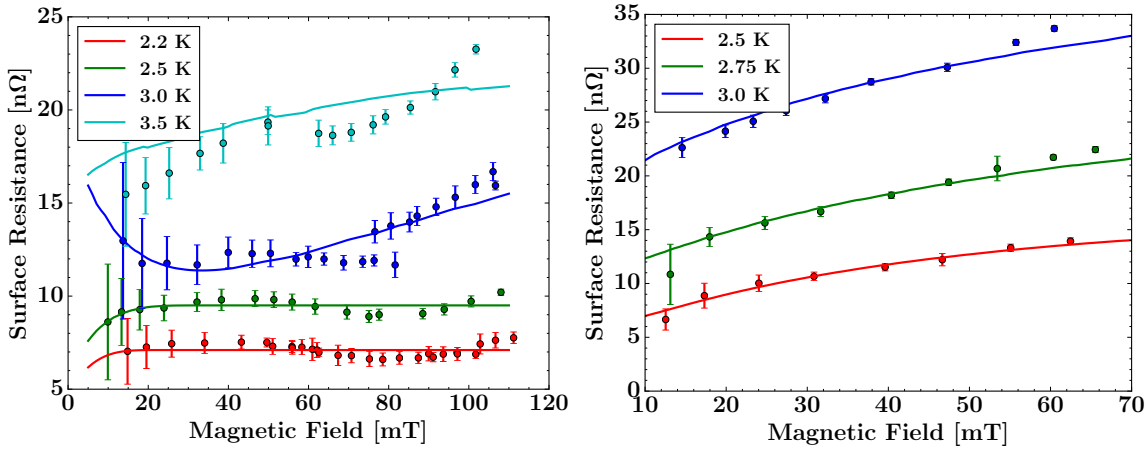

Sample A

Sample B

Figure 9.7: Surface impurity model fit to R_S vs. B data for Sample A and B. Whereas for Sample A, the model clearly provides no adequate fit, the fit cures align nicely with the data for Sample B.

9.3 Modified Density of States Model

In this section, a model will be introduced where the field dependent surface resistance is a result of the current-modified electron quasiparticle density of states. A model fully derived from BCS theory is found in [33] and is the basis of this discussion - here a simplified version will be introduced.

The surface resistance of a superconductor can be calculated using the differential rate at which unpaired electrons absorb and emit photons [93]. The surface resistance of a superconductor can be deduced from Fermi's golden rule and the BCS density of states. The transition rate for absorbing (n_+) and emitting (n_-) photons of energy $\hbar\omega$ is given by:

$$\begin{aligned} n_+ &\propto f(\epsilon)N(\epsilon)\cdot(1-f(\epsilon+\hbar\omega))\,N(\epsilon+\hbar\omega) \\ n_- &\propto f(\epsilon+\hbar\omega)N(\epsilon+\hbar\omega)\cdot(1-f(\epsilon))\,N(\epsilon) \end{aligned} \tag{9.11}$$

where ϵ is the electron-quasiparticle energy, $f(\epsilon) = e^{-\epsilon/k_bT}$ is the Fermi function and $N(\epsilon)$ is the BCS density of states given by:

$$N(\epsilon) = N_0\,\mathrm{Re}\left(\frac{\epsilon - i\gamma}{\sqrt{(\epsilon-i\gamma)^2+\Delta^2}}\right) \tag{9.12}$$

Here N_0 is the normal conducting electron density and γ is a damping parameter, accounting for subgap impurity states. Increasing the damping causes the peak of the electron density of states around $\epsilon = \Delta$ to widen, while reducing the quasiparticle energy gap. The differential rate can now be calculated as:

$$\begin{aligned} n(\epsilon) = n_+ - n_- &\propto N(\epsilon)N(\epsilon+\hbar\omega)\,(f(\epsilon)-f(\epsilon+\hbar\omega)) \\ &\approx N(\epsilon)N(\epsilon+\hbar\omega)\cdot\frac{\hbar\omega}{k_BT}f(\epsilon) \end{aligned} \tag{9.13}$$

The power dissipated by an RF field, proportional to the surface resistance, is a product of the transition rate n, integrated over all quasi-particle states multiplied by the matrix elements $|M|^2 = |\langle p_i|H_\omega(q)|p_f|^2$, with p_i and p_f being the momentum of the quasiparticle in the initial and final state, $H_\omega(q)$ the Hamiltonian and $\hbar q$ being the momentum of the exchanged photon.

$$R_S \propto P_{\mathrm{Dis}} \propto \int_\Delta^\infty N(\epsilon)\cdot d\epsilon \times \int dq dp_i dp_f |M|^2 \tag{9.14}$$

For constant matrix elements, Equation 9.14 reproduces the expression for the BCS surface expression in the clean limit, shown in Equation 2.23 [93].

Already in 1958, Mattis and Bardeen developed a non-local relationship between current density and applied field [94] including random scattering centers, similar to Chambers' expression for the anomalous skin effect [95]. No field dependence is included in this model.

Subsequently, a model for a field dependent surface resistance will be introduced, based on the current-induced broadening of the density of states. The latter has been studied experimentally in tunnelling spectroscopy experiments, where it was found that applying a current broadens the density peaks around Δ and reduces the energy gap [96].

An analytic expression for $N(\epsilon, B)$ can be found in [33], the result is plotted in Figure 9.8. In the same publication a theory extending standard BCS theory to strong RF fields is described, this being beyond the scope of this work however. For the simplified model, we will combine Equation 9.13 with the current modified $N(\epsilon, B)$ to reach:

$$\frac{R_S(B)}{R_S(0)} = k(\alpha, n_{ph}, B, T) = \frac{\int_{\epsilon_g}^{\infty} N(\epsilon, B) N(\epsilon + \hbar\omega, B) e^{-\epsilon/k_B T\left(1+\alpha\left(\frac{B}{B_C}\right)^2\right)} d\epsilon}{\int_{\Delta}^{\infty} N(\epsilon, 0) N(\epsilon + \hbar\omega, 0) e^{-\epsilon/k_B T} d\epsilon} \tag{9.15}$$

$$\epsilon_g = \Delta - n_{ph} \cdot \hbar\omega$$

Apart from the magnetic field and the temperature, the field dependent factor k, plotted in Figure 9.9, introduces two parameters:

- The parameter α, taken directly from [33], describes the overheating of the electron quasiparticles compared to the helium bath temperature (T_0) and is given by:

$$\alpha = \frac{R_s(0) B_C^2}{2\mu_0 T_0} \left(\frac{1}{Y} + \frac{d}{\kappa} + \frac{1}{h_K} \right) \tag{9.16}$$

  the terms $\frac{d}{\kappa} + \frac{1}{h_K}$ describe the thermal impedance of the cavity wall and niobium-helium interface, which is important for RF cavities but not for measurements with the QPR. The term Y describes the electron overheating due to slow quasiparticles-phonon energy transfer rate, which can be a large contribution at low temperatures [97].

- The second free parameter of the model is n_{ph}, which is used to set the lower integration boundary. The motivation behind this is, that the time scales involved in electron-phonon interactions is longer than an RF period and therefore energy states removed far from the unperturbed $N(\epsilon, 0)$ state are not occupied. A more thorough physical interpretation of this parameter is still lacking however.

Applying the simplified model to the data of a Ti-doped niobium cavity [98] reproduced a very similar value of $\alpha \approx 0.8$ compared to the full model fit ($\alpha \approx 0.91$). The large value of α is not fully explainable by thermal conductivity and interface resistance, the electron overheating thus being a significant contribution.

In Figure 9.10, the simplified model postulated here is fit to data obtained with the Quadrupole Resonator. The fitted curve fits the data well for both samples, the fit parameters are shown in Table 9.2. Looking at the fit parameters, we see that the value of n_{ph} is fairly constant for each sample. The values of $R_S(0)$ and α are plotted for the Sample A measurement in Figure 9.11. We see that at low temperatures, $R_S(0)$ nicely matches the BCS prediction for the energy gap and mean free path measured in Section 8.1. Above 3.5 K there are significant discrepancies however. The overheating parameter α increases with temperature, which is reasonable, as $R_S(0)$ increases more strongly than B_C^2 decreases in this temperature range. The absolute values of α are however quite high, especially for the 4 and 5 K measurement. Data could be taken up to 90 mT at 5 K, a value of $\alpha = 4.9$ means that the electron temperature is $T = T_0\left(1 + \alpha\left(\frac{B}{B_C}\right)^2\right) = 9.1$ K, which is still consistent with the sample remaining superconductive.

In this chapter, the field dependency of the surface resistance was studied. It was shown that calculating the surface resistance using the geometry factor significantly distorts the results. The data taken from both samples differed qualitatively, with the surface resistance slightly decreasing around 50-80 mT for Sample A, but rising continuously for Sample B. Two models were introduced and fit to the data. In the surface impurity model, a field dependent penetration gap and a non-uniform material purity are combined to yield a field dependent surface resistance. The second model, based around current-induced broadening of the density of states, fits the data better but has some open theoretical questions concerning the model-simplifications.

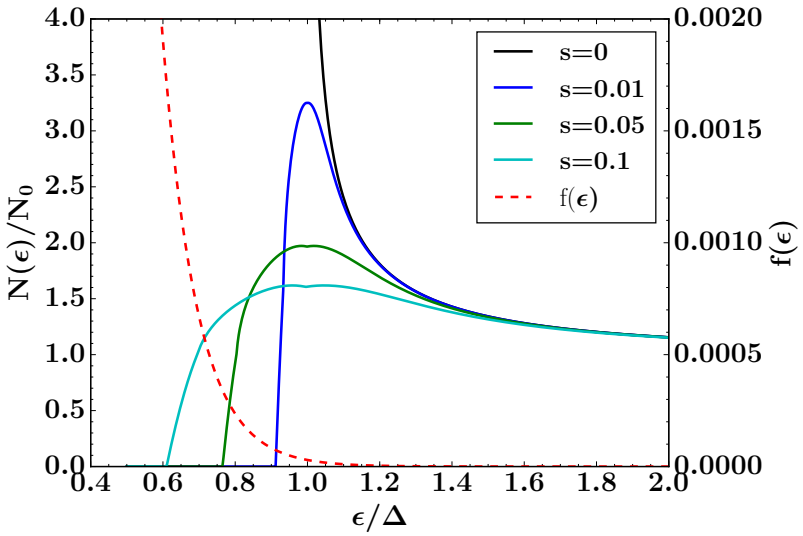

Figure 9.8: Electron density of states for a superconductor carrying different supercurrents $s \propto \left(\frac{J}{J_D}\right)^2$, where J_D is the critical current density. The red dashed line shows the Fermi distribution for $T = 2\,\mathrm{K}$.

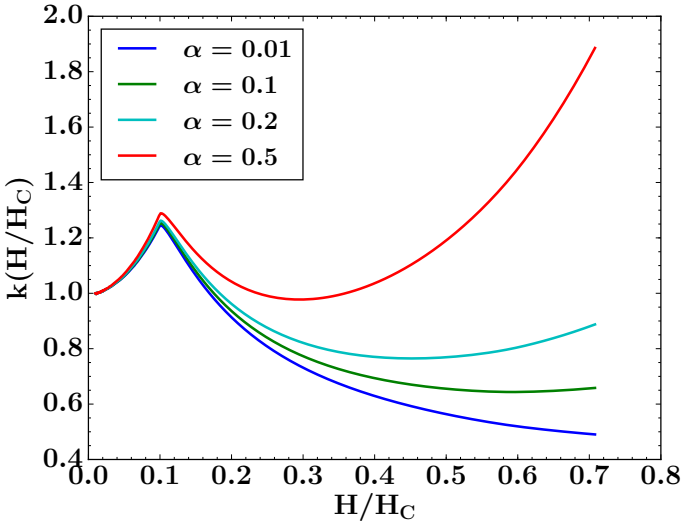

Figure 9.9: Correction factor k plotted against applied magnetic field, for different superheating parameters α. At intermediate fields, the surface resistance can be reduced by more than factor of 2. The initial rise in k is a result of the cutoff energy ϵ_g.

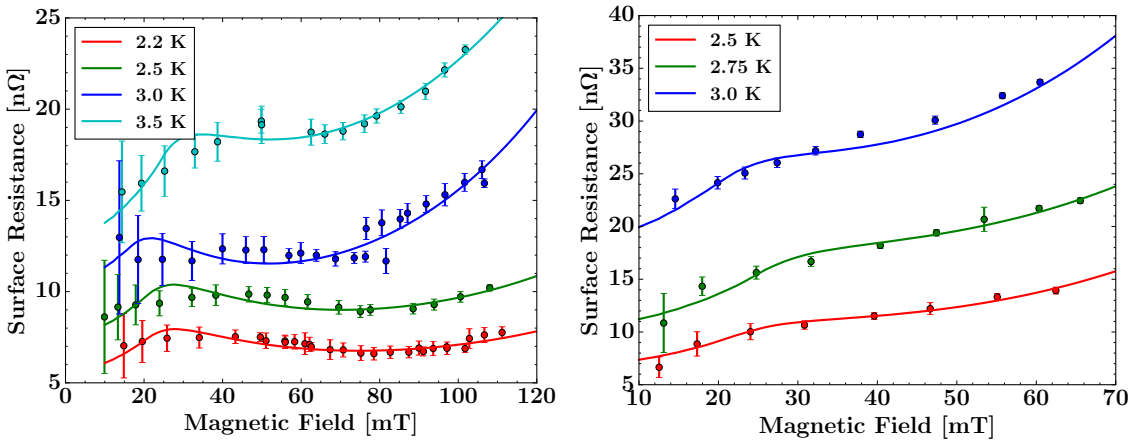

Sample A Sample B

Figure 9.10: Modified density of states model fitted to RvsB data for Sample A and B. The model reasonably fits the data from both samples at all temperatures. The extracted fit parameters are shown in Table 9.2.

	Temperature	$R_S(0)$ [nΩ]	α	n_{ph}	R^2
Sample A	2.2 K	$6.52^{+0.16}_{-0.15}$	$1.03^{+0.07}_{-0.07}$	$3.28^{+0.21}_{-0.18}$	0.67
	2.5 K	$8.43^{+0.22}_{-0.16}$	$1.28^{+0.11}_{-0.11}$	$3.44^{+0.22}_{-0.21}$	0.61
	3.0 K	$11.20^{+1.41}_{-0.92}$	$2.91^{+0.32}_{-0.26}$	$2.43^{+0.71}_{-0.92}$	0.87
	3.5 K	$14.5^{+0.28}_{-0.26}$	$2.87^{+0.19}_{-0.17}$	$4.05^{+0.22}_{-0.29}$	0.97
	4.0 K	$23.83^{+1.46}_{-1.22}$	$4.49^{+0.55}_{-0.51}$	$3.04^{+0.50}_{-0.60}$	0.82
	5.0 K	$48.9^{+6.69}_{-2.71}$	$4.91^{+0.85}_{-0.83}$	$5.27^{+.72}_{-1.07}$	0.77
Sample B	2.5 K	$6.97^{+0.45}_{-0.55}$	$1.35^{+0.17}_{-0.20}$	$6.20^{+1.21}_{-0.98}$	0.95
	2.75 K	$10.68^{+0.63}_{-0.62}$	$1.28^{+0.26}_{-0.21}$	$7.23^{+1.08}_{-1.25}$	0.96
	3.0 K	$15.97^{+1.41}_{-1.23}$	$1.76^{+0.41}_{-0.38}$	$5.40^{+1.04}_{-0.95}$	0.91
	3.5 K	$24.48^{+4.07}_{-2.30}$	$2.22^{+0.37}_{-0.39}$	$6.11^{+1.61}_{-1.44}$	0.98

Table 9.2: Fit parameters for the modified density of states model.

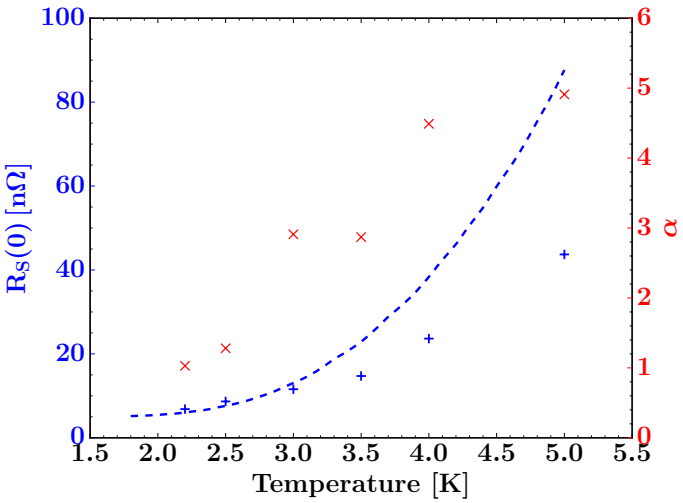

Figure 9.11: Fit results from sample A. The value of $R_S(0)$ is shown in blue, the overheating parameter α in red. The dashed blue line is the low field BCS resistance for the gap energy and mean free path measured in Section 8.1

Chapter 10

Summary and Outlook

For this work, an experiment for detailed RF-characterization of superconducting samples was designed, constructed and commissioned. The design of the Quadrupole Resonator was adapted from the original CERN design, attaining improved figures of merit and allowing measurements at 1.3 GHz, the operating frequency of many superconducting accelerators. After performing the required surface finishing procedures at Jefferson Laboratory, the Quadrupole Resonator was the first superconducting cavity to be tested in the newly constructed vertical testing facility at Helmholtz-Zentrum-Berlin. After resolving microphonics issues in the commissioning runs, stable measurements could be performed up to peak magnetic fields of 120 mT, higher than any previously published results from comparable sample testing experiments.

The core results presented were taken from two niobium samples of the same nominal purity. The main difference between the samples was that only Sample A underwent a 120° C baking procedure. Measurements of the surface resistance 416 MHz yielded results under 10 nΩ for both samples and showed the expected temperature dependency. Measurements of the penetration depth and critical field also nicely matched expected values. The established decrease in electron mean free path caused by the 120 °C bake was observed. A very low trapped flux sensitivity of 0.8 nΩ/μT was measured compared to 1.3 GHz cavities made from similar material. Measurements of the field-dependency of the surface resistance showed qualitative difference between both samples. Two models, the surface impurity and the modified density of states models were introduced and fit to the data, the latter providing a better match.

From the data analysis it was shown that extracting fit parameters from non-linear models (such as the BCS-surface resistance) needs to be done with care. It was demonstrated that a naive use of the geometry factor can lead to significant errors when measuring the field-dependent surface resistance using cavities with a strongly inhomogeneous field distribution.

Following this work, a new PhD project has already begun, with tests on nitrogen-doped niobium and Nb_3Sn already moving along. RF systems at 850 and 1300 MHz have been installed and will add a further measurement dimension. Other aspects of the experimental setup are also being continuously improved. Within this work, measurements often took a long time due to RF control issues, multipacting as well as long thermalization times, caused by stored heat in components connected to the sample. Interesting measurements had to be omitted due to time constraints, which could be reduced by better clean-room and instrumentation-mounting procedures. Measurements and analyses not performed within this work worth considering include:

- Combining multiple measurements for higher precision of the fit parameters. Using surface resistance against temperature data measured at various frequencies and combining it with penetraton depth against temperature data would result in very tight limits on the electron mean free path and energy gap.
- Measuring the RF field dependence of the trapped flux sensitivity and how the cooling rate effects the trapped flux losses. Using both a ring heater and the point-like heat source one could further control both the temporal and the spatial temperature gradient independently.
- Investigating the frequency dependency of the trapped flux sensitivity, as this is a direct test to the the various theories describing the loss mechanism.
- Studying the field dependence of the penetration depth. The result can be used to check the assumptions behind the surface impurity model.
- Measuring surface resistance against field curves at more temperatures and fit the field-dependent models globally.
- Using the frequency independent material properties (penetration depth, electron mean free path) to further benchmark the system and possible improving the simulation constants.
- Combining measurements of the Quadrupole Resonator with other diagnostic methods such as studying the surface profile (scanning electron microscopy), the elemental composition (X-ray photo spectroscopy) and the DC-magnetic properties.

Appendix A

Surface Impedance

Electromagnetic fields stored in an RF cavity will lead to power dissipation through eddy currents induced by magnetic fields. In this section we will motivate and define the surface impedance and calculate it for normal and superconductors.

To begin, we consider how electromagnetic waves will propagate within a lossy medium with permittivity ϵ and conductivity σ. Taking the curl of the Ampère Maxwell equation and using $\nabla \cdot \boldsymbol{H} = 0$ one obtains:

$$\begin{aligned} \nabla \times \nabla \times \boldsymbol{H} = -\nabla^2 \boldsymbol{H} &= \nabla \times (\boldsymbol{J} + \epsilon \frac{\partial \boldsymbol{E}}{\partial t}) \\ &= \nabla \times (\sigma \boldsymbol{E} + (\epsilon' - i\epsilon'') \frac{\partial \boldsymbol{E}}{\partial t}) \\ &= \mu_0 \omega (\omega \epsilon' - i(\sigma + \omega \epsilon'')) \boldsymbol{H} \end{aligned} \tag{A.1}$$

Here, the complex permittivity is separated into the real part ϵ' which is related to the stored energy within the medium and the dissipative term ϵ''. Note that Ohm's law $\boldsymbol{J} = \sigma \boldsymbol{E}$ was used here which gives a local relationship between current density and electrical field. Also, dielectric losses by ϵ'' cannot be distinguished from conductivity losses, allowing us to define an effective conductivity of $\sigma_{eff} = (\omega \epsilon'' + \sigma)$ [99].

For the rest of this section we will look at the situation in which the cartesian half space $z > 0$ is filled with a lossy material. Our Ansatz here is that E and H are plane waves decaying with a damping constant of γ

$$E_x(z,t) = E_0 e^{-\gamma z} e^{i\omega t} \ , \ H_y(z,t) = H_0 e^{-\gamma z} e^{i\omega t} \tag{A.2}$$

The damping constant γ can thus be calculated by applying Equation A.2 to Equation A.1

$$\gamma = \sqrt{\mu_0 \omega (-\omega \epsilon + i\sigma)} \tag{A.3}$$

Now one uses faradays law to relate magnetic and electric fields

$$\nabla \times \boldsymbol{E} = \frac{\partial E_x}{\partial z} = -\frac{\partial B_y}{\partial t} = -i\mu_0\omega H_y \tag{A.4}$$

the surface impedance is defined as the ratio of the tangential electric and magnetic field on the conducting surface:

$$\begin{aligned} Z_s = \frac{E_x(z=0)}{H_y(y=0)} &= \frac{\int_0^\infty \frac{\partial E_x}{\partial z} dz}{H_0} = \frac{\int_0^\infty i\omega\mu_0 H_0 e^{-\gamma z}}{H_0} \\ &= \frac{i\mu_0\omega}{\gamma} \\ &= \sqrt{\frac{i\mu_0\omega}{\sigma + i\epsilon\omega}} \end{aligned} \tag{A.5}$$

The surface impedance is a useful quantity, as it allows us to calculate how much power is dissipated by a given RF field. We start with the energy conservation equation stating that the power S flowing into a volume V must be equal to the change of stored energy W plus the power dissipated P_{Dis} in that volume:

$$-\oint_{\partial V} \boldsymbol{S} \cdot dA = \frac{d}{dt}\int_V W dV + \int_V P_{Dis} dV \tag{A.6}$$

After applying Gauss' law and dropping the volume integral, we arrive at the local conservation statement:

$$\nabla \cdot \boldsymbol{S} + \frac{\partial W}{\partial t} + P_{Dis} = 0 \tag{A.7}$$

For the steady state solution, we can drop the time dependant term and end with the power flowing across our interface being equal to the power dissipation in our material. From Maxwell's equations we can derive that the energy flux density is given by the Poynting vector $S = (E \times H)$, allowing us to calculate the dissipated power per unit area:

$$\begin{aligned} P_{Dis} &= \Re\{\langle (E \times H)_{z=0} \rangle\} \\ &= \frac{1}{2}\Re\{E_x(z=0) \cdot \overline{H_y(z=0)}\} \\ &= \frac{1}{2} R_S |H(z=0)|^2 \end{aligned} \tag{A.8}$$

where the surface resistance R_S is defined as the real part of the complex impedance. Note that A.8 is a local relationship and that the surface impedance is a material property. This means that even for complicated geometries, it is enough for us to know the surface magnetic fields to be able to calculate the dissipated power. The imaginary part of the surface impedance is the surface reactance X_S, giving us:

$$Z_S = R_S + iX_S \tag{A.9}$$

A.1 Skin effect

Let us now try to calculate the surface resistance for normal conducting metals. The equation for the damping constant can be simplified for good conductors ($\sigma \gg \omega\epsilon$)

$$\begin{aligned} \gamma = \sqrt{\mu_0\omega(-\omega\epsilon + i\sigma)} &\approx \sqrt{i\mu_0\omega\sigma} \\ &= \sqrt{\frac{\mu_0\omega\sigma}{2}}(1+i) = \alpha + i\beta \end{aligned} \tag{A.10}$$

The characteristic length with which an RF field will penetrate the metal is called the skin depth and is given by:

$$\delta = \frac{1}{\alpha} = \sqrt{\frac{2}{\mu_0\omega\sigma}} \tag{A.11}$$

An expression for the surface impedance of normal conductors can be calculated using equation A.5

$$Z_s = \frac{u\mu_0\omega}{\gamma} = (1+i)\frac{1}{\sigma\delta} \tag{A.12}$$

As a metal with a high conductivity copper has a conductivity of $\sigma = 5.9 \cdot 10^7\,\mathrm{S/m}$. At a typical frequency of 1 GHz for RF cavities, this corresponds to a skin depth of $\sim 2\mu$m and a surface resistance (and reactance) of 8 mΩ.

A.2 Anomalous skin effect

The skin effect does well at describing the surface resistance of metals at room temperature. As the resistivity of pure metals has an approximate linear temperature dependence, we expect a decrease in the surface resistance according to equation A.12. The measurement data however showed, that the surface resistance of (normal-conducting) Tin was higher than expected by a factor of 3 at 3.8 K [100]. The reason for this effect is that the mean free path of the electrons becomes large compared to the skin depth and that the electrons are therefore accelerated in an inhomogeneous field between collisions. This is however one of the assumptions of the Drude modell, which was used to derive Ohm's law ($\boldsymbol{J} = \sigma\boldsymbol{E}$).

An expression for the current density was developed by Chambers [95], which relates the current density not only to the local electric field $E(r')$ but to the volume for which $|\boldsymbol{r'} - \boldsymbol{r'}| \leq l$

$$\boldsymbol{J}(\boldsymbol{r}, t) = \frac{3\sigma}{4\pi l}\int_V \frac{\boldsymbol{R}(\boldsymbol{R}\cdot\boldsymbol{E}(\boldsymbol{r'}, t - \boldsymbol{R}/v_F))e^{-\boldsymbol{R}/l}}{\boldsymbol{R}^4}\boldsymbol{dV}\ ,\ \boldsymbol{R} = \boldsymbol{r'} - \boldsymbol{r} \tag{A.13}$$

Here v_F denotes the Fermi velocity of the electrons and the $e^{-\boldsymbol{R}/l}$ term weights the contribution of the electric fields depending on the distance from point $\boldsymbol{r}$. Following on from Equation A.13 one can define a dimensionless constant α as:

$$\alpha = \frac{3l^2}{2\delta} \tag{A.14}$$

with δ being the classical skin depth. In the case of the anomalous limit ($\alpha \gg 1$), the surface impedance is:

$$Z_{An} = (\frac{\sqrt{3}}{4}\mu_0^2\epsilon_0\omega^2\frac{l}{\sigma})^{1/3}(1 + \sqrt{3}i) \tag{A.15}$$

We see that in this limit, the frequency dependence is now $\sim \omega^{2/3}$. Furthermore, $\frac{l}{\sigma}$ is a material constant, independent of temperature. This means that further cooling down a conductor already in the anomalous limit will not further decrease the surface resistance, even though the conductivity will continue to rise.

Appendix B

Measurement Resolution and Bias

For the Quadrupole Resonator to be a useful tool to study materials for SRF cavities, the measurement resolution and precision must be in the order of 1 nΩ, comparable with the currently lowest achievable surface resistances. In this chapter we will assess both of these quantities, which are both RF field and sample dependent, and also discuss sources of measurement bias. For all of these considerations, an accurate thermal model of the thermometry chamber is required.

B.1 Thermal Simulation

Heat created by either the RF field or the DC heater needs to flow down the cutoff tube and across the stainless steel flange before being cooled by the liquid helium bath, shown in Figure B.6. This relatively long heat path, around 10 cm compared to the 3mm typical for niobium cavities, means that even small amount of heat will cause a rather large temperature increase of the sample. Being able to simulate the temperature response of the sample-flange system is important for a systematic understanding of the measurement capabilities of the QPR.

Due to the rotational symmetry of the sample, a simple code could be written, simulating the thermal model in full detail. It involves solving Fourier's law of heat conduction:

$$\dot{Q} = -k(T) \cdot A \cdot \frac{\partial T}{\partial z} \tag{B.1}$$

The geometry of the system can be described in cylindrical coordinates (r, ϕ, z), and the heat flow reduced to a one dimensional path from the center to the outside of the sample, down the cutoff tube and through the stainless steel flange to the helium bath. At each of these points, the cross section $A(\rho, z)$ through which the heat flows is calculated, shown in the top plot of Figure B.1. The domain is then discretized and Equation B.1 is solved for

each cell individually, calculating temperature gradients and updating the temperature in each cell until a stable solution is reached. The boundary conditions used is $T(z = 0) = T_B$ with a the starting condition of $T(i) = T_B$, where $T_B = 1.8$ K is the helium bath temperature, two further things have to be considered:

- The temperature dependence of the thermal conductivity - at very low temperatures, the dependence is very strong, doubling for high purity Niobium between 2 and 4 K [101]. Niobium at this temperature has around 100 times the thermal conductivity of stainless steel.
- The heat flowing through the system has two sources, the heater and the RF field. As the heater is positioned in the middle of the sample, it provides a constant heat flow through the entire system. For the RF field, the magnetic field profile taken from the RF Simulation is used to obtain a radial distribution of the heating on the sample surface. Furthermore the model includes the heat input the normal conducting flange (discussed in more detail in Section B.3.1). This is shown in the red curve of the center plot in Figure B.1.

With this model, we can now calculate the sample temperature for any combination of RF and heater power. To validate our model we compared the temperature versus heater power curve with experimental data, shown in Figure B.2.

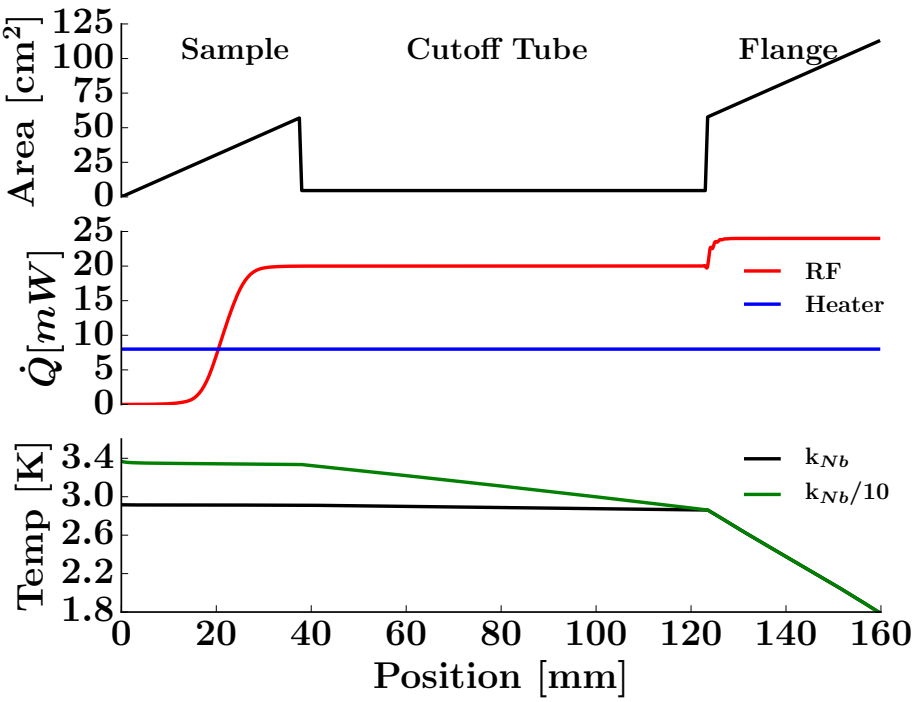

Figure B.1: Temperature profile across the thermometry chamber for the a given RF and heater power (shown in middle diagram). The helium bath is it at the x-axis origin, the center of the sample is at 160 mm. Temperature profile is shown for high purity niobium in black and for a sample with reduced thermal conductivity in green.

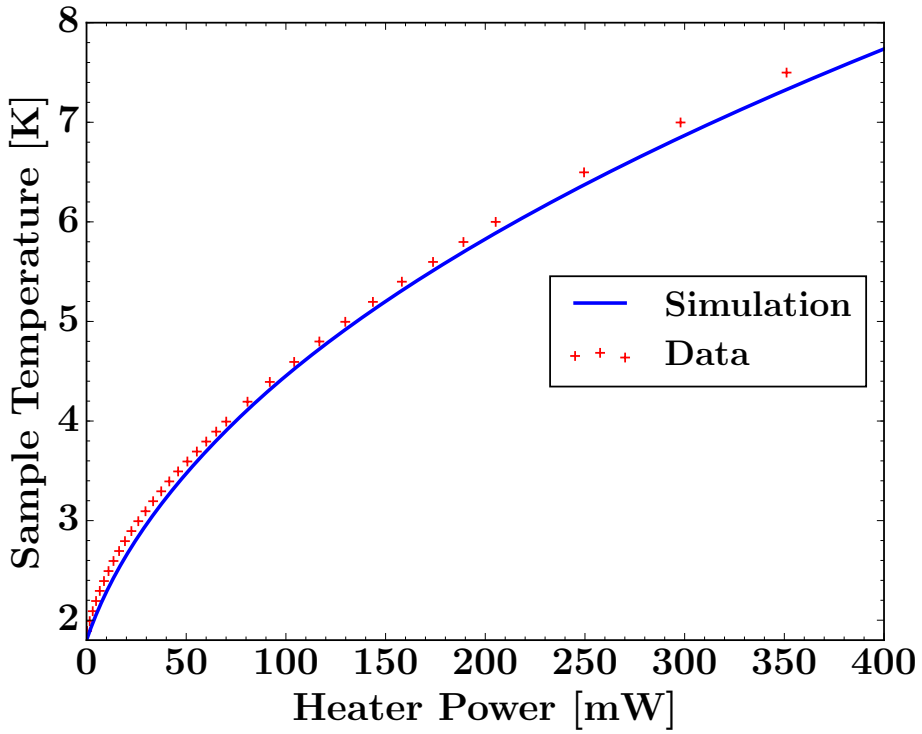

Figure B.2: Sample temperature versus heater power. Good agreement between simulation and experimental data.

We can calculate the measurement resolution of the Quadrupole Resonator, which is limited by the temperature resolution of the temperature controller, in our case 0.1 mK for the Lakeshore 336 model used with CERNOX sensors of type CX-1050. Using Figure B.2, the temperature resolution can be translated into a minimal detectable RF heating of around $2\,\mu$W at 2 K. We can translate this into a measurement resolution of :

$$\Delta R_S = \frac{2\Delta P_{RF}}{\int_{Smpl} |H|^2 dA} \tag{B.2}$$

We see that the temperature resolution is field dependent, increasing with the square of the applied RF field. For a field of only 5 mT, the resolution is already 0.3 nΩ and thus fully sufficient for our purpose.

B.2 Measurement Precision

The measurement precision of the QPR cannot be calculated simply, as it is varies with temperature and magnetic field, as well as the thermal conductivity of the sample. We will start our discussion by revisiting Equation 3.2, expressed explicitly in measurable quantities:

$$R_S = \frac{2\omega \cdot (V_1^2 - V_2^2)}{c \cdot Q_{FP} \cdot R_{Heater} \cdot P_T} \tag{B.3}$$

Three of these quantities are measurands, the RF power P_T and the heater voltages V_1 and V_2 . The noise of the RF power measurement is negligable, even though it has a large systematic error due to calibration uncertainty and impedance mismatch of around 5% (Gigatronics 8540C). Focussing solely on the on the $(V_1^2 - V_2^2)$ term, we can calculate the relative error explicitly by taking the derivative of Equation B.3:

$$\frac{1}{R_S} \cdot \frac{\partial R_S}{\partial (V_1^2 - V_2^2)} = \frac{2\Delta V}{V_1 - V_2} \tag{B.4}$$

where V_1 and V_2 are the heater voltages required to maintain the desired temperature without and with RF field and ΔV is the uncertainty of the voltage measurement. V_1 and V_2 can both be computed for abitrary temperature and RF field using the thermal model presented in Section B.1. The voltage uncertainty ΔV has several contributions:

- Measurement resolution of the voltmeter. The Keithly 2000 used to measure the voltage across the heater has a resolution of $\pm 0.1\,\mu$V and an accuracy of better than 0.01%. Compared with other sources this is a negligible contribution, electromagnetic interference from external sources can change this however.

- The current source. The temperature controller which drives the heater, a Lakeshore 336, has a specified rms noise of $\pm 12\,\mu$A. As we are using a 50Ω heater, this translates to 0.6 mV voltage deviation.

- Temperature stability of the helium bath. Pressure fluctuations in the helium system will change the required heating necessary to maintain a constant sample temperature. The pressure fluctuations of the HZB cryoplant are $\Delta P = \pm 0.1$ mbar at our operating temperature of 1.8 K [64] . We can translate this into a voltage uncertainty using partial derivatives:

$$\begin{aligned} \Delta V &= \frac{\partial V}{\partial \dot{Q}} \cdot \frac{\partial \dot{Q}}{\partial T} \cdot \frac{\partial T}{\partial P} \cdot \Delta P \\ &= \sqrt{\frac{R}{4 \cdot \dot{Q}}} \cdot \frac{\partial \dot{Q}}{\partial T} \cdot 2 \cdot 10^{-3}\,\mathrm{K} \end{aligned} \tag{B.5}$$

  here $\frac{\partial T}{\partial P}$ was calculated from pressure-temperature curves of helium II generated by HEPAK [102]. The term $\frac{\partial \dot{Q}}{\partial T}$ is a measure of how much heating is required to change the sample temperature and is provided by our thermal model. Is around 20 mW/K

for 2K and increases approximately linearly with rising temperature. The term $\frac{\partial V}{\partial \dot{Q}}$ is simply the voltage to power relationship of the heater.

Unlike the contribution from the current noise, the voltage error caused by pressure fluctuations thus depends on many parameters: The measurement temperature and field as well as the thermal conductivity of the sample. In Figure B.3, the two contributions for a high purity niobium sample measured at 20 mT is shown against temperature.

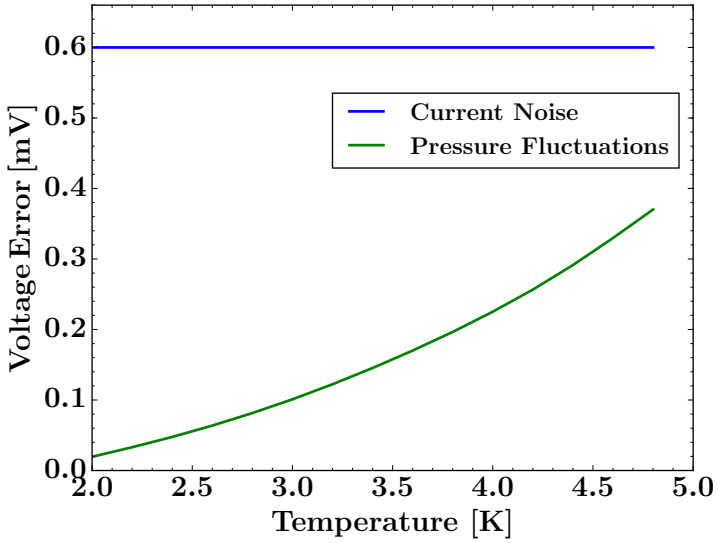

Figure B.3: Voltage fluctuations caused by current noise of the temperature controller and pressure fluctuations in the helium bath

Geometrically adding the two relevant contributions, the expected resolution of our system is shown in Figure B.4. One sees, that higher RF loses on the sample, either by a higher surface resistance or a higher field, improve the resolution. A low thermal conductivity of the sample will increase the resolution slightly, above 10 mT, the measurement precision is generally better than 1 nΩ . Averaging multiple data points can of course also be used to further increase measurement precision.

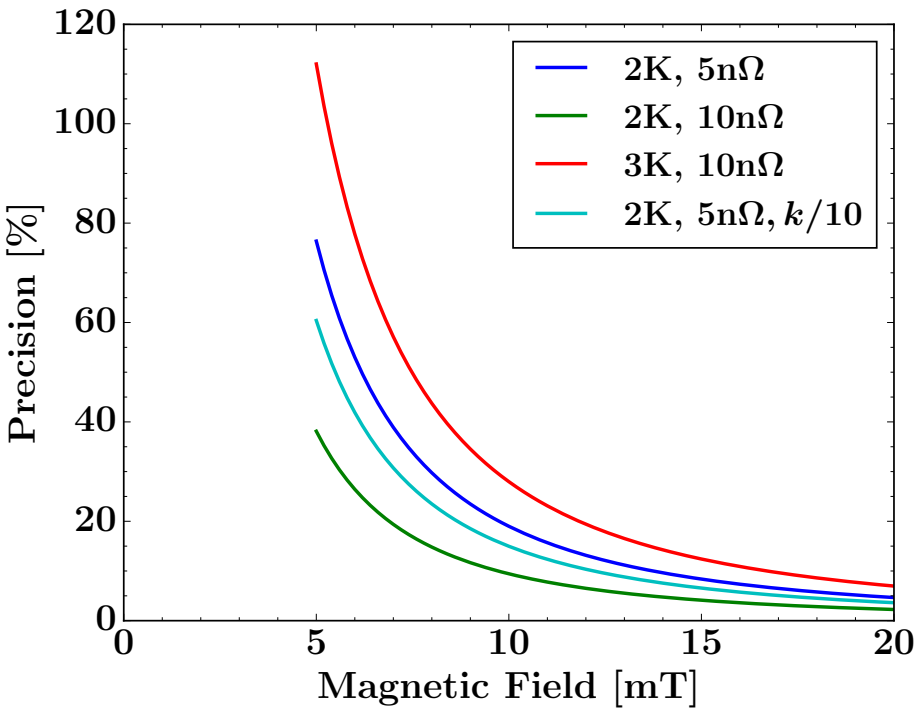

Figure B.4: Calculated measurement precision for the Quadrupole Resonator for several test cases. Even though the precision seems to get worse at higher temperatures, the increased surface resistance will typically compensates for this. Above 10 mT, the measurement precision is generally better than 1 nΩ.

B.3 Measurement Bias

The systematic measurement error of the QPR has several contributions. The first is the bias of the RF power measurement. The power meter (Gigatronics 8540C) has a nominal uncertainty of 0.2 dB, to which we can add another 0.1 dB due to uncertainty in the cable calibration. This comes to an error of 7%.

Another uncertainty stems from the value of the required simulation constant which relates the stored energy inside the cavity (which is measured by the RF power measurement) to the magnetic fields on the sample surface. This simulation constant is denoted denoted as 'c' in Equation B.3. There are two contributions to the uncertainty of this parameter, the first being the precision of the numerical computation of the eigenmodes, the second being the geometrical deviations of the physical resonator to the ideal geometry used in the simulation. The numerical accuracy can be set within the simulation software and is set to be better than 10^{-9}, negligable for our interest. The second term is rather difficult to assess. Measuring all relevant dimensions of the loop geometry is not possible due inaccessibility

of the inner resonator. As an indicator for the geometry mismatch, the resonance frequency is a good indicator. For the fundamental operating TEM_{21} mode, the measured frequency was around 4 MHz below the simulation value. If we could attribute the entire detuning to a single wrong dimensions, we could calculate a corrected version of c. Unfortunately this is not the case and the value of $\frac{\partial c}{\partial x}$ is very different for different parameters. For the gap between sample and rods, the value of c changes by around 10%/MHz whereas for the radius of the rods it is below 1%/MHz, a value similar to other parameters. As we were able to measure the gap width directly (see Section 5.3.5) we will use the second value and estimate this uncertainty to 5%.

For the rest of this section we will focus on three further systematic uncertainties, which require more detailed analysis. The first is the effect of the different heat distributions of the heater and RF field, the second is the effect of the RF heating of the normal conducting flange. Finally, we will consider the effects of pulsed measurements, which are required when high RF losses on the sample occur.

B.3.1 Non-uniform heat distribution of the RF field

As we saw in Figure B.1, the radial heat distribution is not uniform, due to the RF field being strongly focussed in the area directly below the niobium loops. If RF heating causes a different temperature response from the heater, a measurement bias may be introduced.

To study this effect, we used our thermal model from Section B.1 to simulate a $R(B)$ measurement at 3 K, for a sample with a constant surface resistance of 10 nΩ. Sample temperature versus heater power curves were calculated for different RF fields and used to calculate the heater power required to maintain the constant temperature. From the different heater powers, one can use Equation B.3, to recalculate the surface resistance, Figure B.5. The blue curve assumes the same constant heat flux for heater and RF field and should thus be field independent and constant, the field dependence being product of the numerical computation. The red curve was calculated with the non-uniform RF heating, producing a shift of 0.1 nΩ. The error caused due to non-uniform RF heating is thus only small compared to other measurement biases.

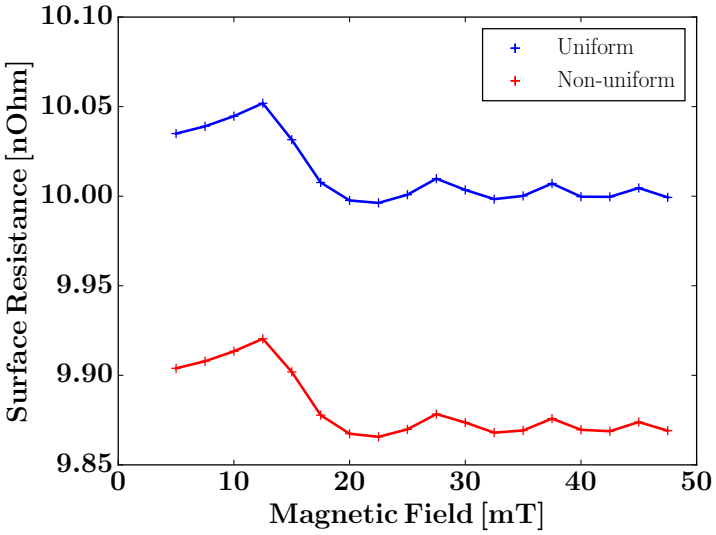

Figure B.5: Error from non-uniform RF heat flux, shown in red. The baseline calculation in blue is expected to be constant at 10 nΩ, the field dependence being a relict of the numerical computation

B.3.2 Unwanted Heating of Normal-Conducting Flange

A critical aspect of the QPR design concerns the connection between calorimetry chamber and resonator. For a UHV tight connection, Conflat flanges are typically used, which are made from stainless steel, the seal being provided by a copper gasket. As both steel and copper are normal conducting, they have to be positioned in a very low field area to avoid excess heating. This issue needs to be understood thoroughly, as additional heating may not only cause a quench of the resonator but may also cause a systematic measurement error. The following analysis will focus on first calculating how large the fields are at the normal conducting surfaces, how much heating these fields are expected to produce and on how this generated heat my affect measurements.

Figure B.6 shows a detailed view of the sample and the coaxial gap. The purpose of the coaxial gap is to attenuate the strong magnetic fields present at the sample surface down to a tolerable level at the stainless steel surface. From a CST MWS simulation, the magnetic field of the 433 MHz mode is plotted down the coaxial gap. One could of course simply extract the fields on the stainless steel flange from the simulation directly. There are however doubts as to the accuracy of the eigenmode solvers when dealing with strongly attenuated fields propagating below the cutoff.

To validate the simulation, the problem was cross-checked using transmission line theory. The coaxial gap can be treated as a coaxial conductor with an inner radius a of 37.5 mm

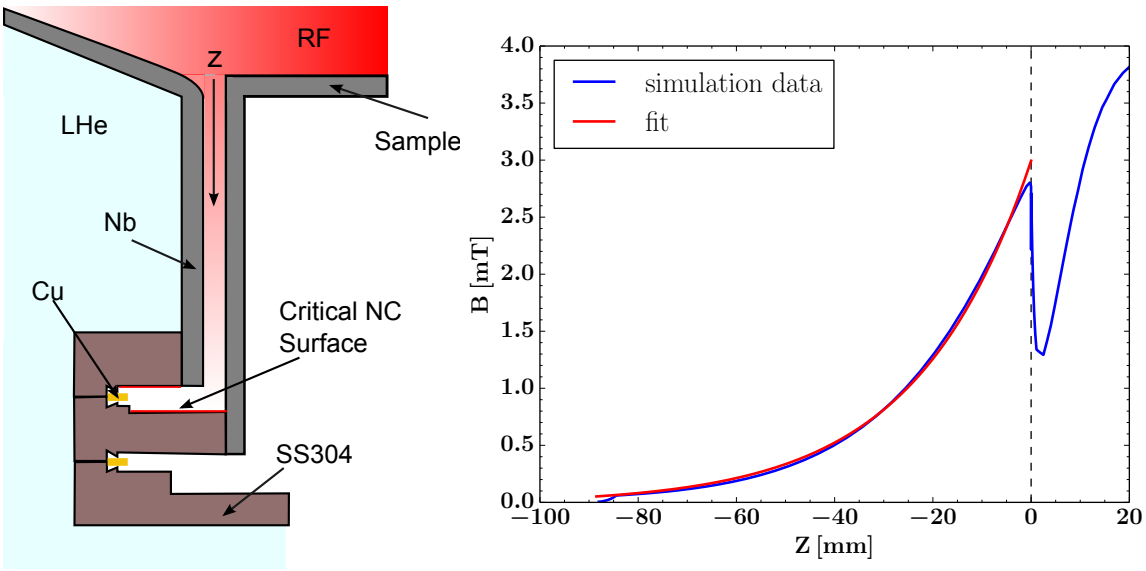

Figure B.6: Detailed view of the coaxial gap together with magnetic field plotted down towards the normal conducting flange

and an outer radius b of 39 mm. TEM-monopole modes in coaxial lines propagate at all frequencies. Higher order dipole and quadrupole modes have a cutoff frequency depending on the dimensions a and b. In our case, we are interested in the cutoff frequency of the TE21 mode.

Considering the TE modes, we have by definition $E_z = 0$ whereas H_z is assumed to be of the form $H_z(\rho, \phi)) = h_0(\rho, \phi)e^{-i\beta z}$ and solves the wave equation:

$$\nabla^2 H_z + k^2 H_z = 0 \tag{B.6}$$

with the appropriate boundary conditions

$$E_\phi(\rho, \phi) = 0 \qquad \text{for} \quad \rho = a, b \tag{B.7}$$

The analytical calculations are not shown here but can be reviewed in [99]. The propagation constant β can be calculated once the cutoff wavenumber k_c has been determined by $\beta = \sqrt{k^2 - k_c^2}$. Calculating the cutoff wavenumber for TE modes requires finding solutions for the transcedental equation

$$J_n'(k_c a)Y_n'(k_c b) - J_n'(k_c b)Y_n'(k_c a) = 0 \tag{B.8}$$

where J_n and Y_n and Bessel functions of the first and second kind. As we are looking for the cutoff of the quadrupole modes, we must find solutions for the second order $n = 2$ case.

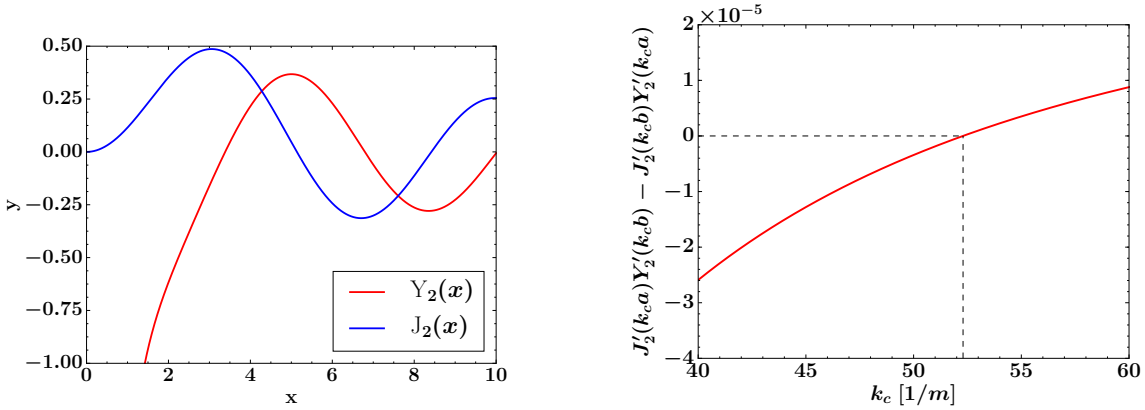

Figure B.7: Plot of Bessel function of first and second kind, second order. Right plot shows numerical computation of the cutoff wavenumber for the dimensions of our coaxial gap.

As no compact analytical expression for Y_n' exists, we performed a numerical computations of the derivatives, as shown in figure B.7b.

If one uses the the cutoff wavenumber obtained from B.7b, one can now calculate the characteristic length β with which the fields decay for 433 MHz and 1300 MHz, arriving at propagation constants of $^{0.052}/_{\text{mm}}$ and $^{0.045}/_{\text{mm}}$. The numerical value agrees with the simulation data to within 2%, establishing trust in our simulation. For the chosen dimensions of the coaxial gap with a length of 88mm, the dimensionless constant relating the dissipated power on the sample to that on the normal conducting flange is :

$$\delta = \frac{\int_{Smpl} ||H||^2 dA}{\int_{Flange} ||H||^2 dA} = 6.15 \cdot 10^6 \tag{B.9}$$

The small value of δ suggests that heating on the stainless steel flange should be small, the enormous difference between the RF surface resistance of normal and superconductors needs to be considered though. The electrical conductivity of stainless steel is taken from [103] to be $1.8 \cdot 10^6\,\Omega\text{m}^{-1}$. The normal conducting surface resistance is calculated with equation B.10 to be $R_s = 30.8\,\text{m}\Omega$ for 433 MHz.

$$R_s = \sqrt{\frac{\pi \mu_0 f}{\sigma}} \tag{B.10}$$

The power due to RF losses on the flange, can now be expressed as

$$P_{flange} = P_{sample} \frac{R_{s,SS}}{\delta \cdot R_{s,Nb}} \tag{B.11}$$

At temperatures below 2 K, values around 10 nΩ have been consistently reached for high quality niobium. Taking this value, one sees that the losses on the flange are about 50% of the losses on the sample, a considerable error source.

In the remaining part of this section, we will discuss how this heat can affect the surface resistance measurement. We start by the observation, that the surface resistance of the normal conducting surface is independent of temperature in the range we are measuring at. Our modified RF power now leads to a new expression for the surface resistance with just a constant offset:

$$P_{RF} = \frac{1}{2} \int_{Smpl} ||H||^2 (R_s(T) + R_{SS} \cdot \delta^{-1}) dA \tag{B.12}$$

$$\Rightarrow \quad R_s(T) \approx \frac{2P_{RF}}{\int_{Smpl} ||H||^2 dA} - R_{SS} \cdot \delta^{-1} \tag{B.13}$$

So far we have been making the assumption, that dissipated power on the sample and on the flange lead to the same temperature response (measured on the bottom side of the sample) and can thus be simply added together. Looking at the different paths heat must travel to reach the liquid helium from the two sources (see Figure B.6), one arrives at the conclusion that this assumption is erroneous.

Using the model introduced at the start of the section, we studied the effect of the additional heat source. Assuming a constant surface resistance of both the superconducting sample and the normal conducting flange, the necessary heater power to maintain a constant temperature was calculated for different applied magnetic fields. From this, the 'measured' surface resistance could be calculated and compared to the actual value. The results for a 10 nΩ sample are shown in Figure B.8. We see that the temperature dependence of the material produces a very small field dependence on the result, but the variations can be considered marginal. The resistance is overestimated considerably though, in this case by a constant offset of 4.6 nΩ. A constant offset can also be assumed when measuring surface resistance against temperature, as the superconducting resistance increases exponentially whereas the normal conducting losses stay almost constant, thus becoming negligable at higher temperatures. Unwanted heating on the normalconducting flange thus produces a significant measurement bias for high quality samples, leading to increased residual resistances. This error may be eliminated by either increasing the length of the cutoff tube or using higher conducting material on the flange surface.

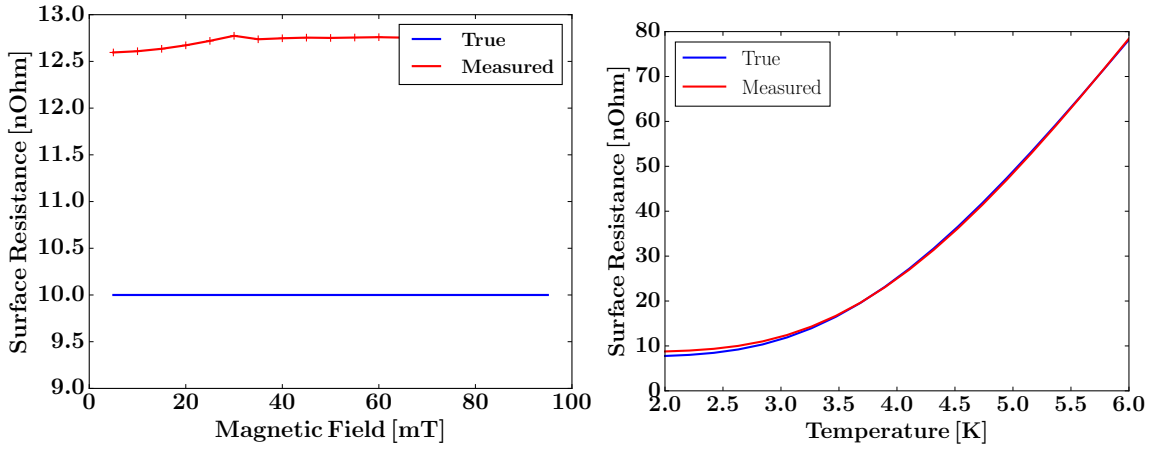

Figure B.8: Effect of the flange heating on measurement results. On the left, a constant resistance of 10 nΩ is assumed, the temperature dependence of the thermal conductivity induces small deviations at different applied fields. These are very small compared compared to the measurement offset however. On the right a resistance against temperature measurement is simulated. Only deviations at low temperatures are found, the residual resistance is thus overestimated. At higher temperatures, the curves converge.

B.3.3 Pulsed Measurement

As we saw in Figure B.1, already a moderate amount of dissipated power on the sample surface will cause a significant temperature rise. For the surface resistance masurement this means that not the entire parameter space can be mapped using a CW measurement, as the compensation technique does not work if the RF fields already heat the sample above the temperature of interest.

For this reason one must use pulsed RF fields. The measurement principle remains unchanged, only the duty cycle (the fraction of time the RF is switched on) must be factored into Equation 3.2. Figure B.9 shows the maximum duty cycle at which one can measure the surface resistance of a typical RRR 300 niobium sample for a typical range of temperature and peak magnetic fields. The plot was generated using the thermal model shown in Figure B.1 and Equation 2.23 to calculate the surface resistance of the niobium, which was here assumed to be field independent.

In Figure B.10, the influence of the chosen duty cycle and pulse period are shown are shown. At a low temperature and field, corresponding to low RF losses, the pulsed measurement can lead to a considerable error. At higher temperatures, where the RF losses are higher, the measurement results are far less sensitive to the duty cycle and pulse period. As a result, when measuring at low temperatures one should try to always measure at the highest duty cycle possible to reduce this source of error. More discussion on this topic can

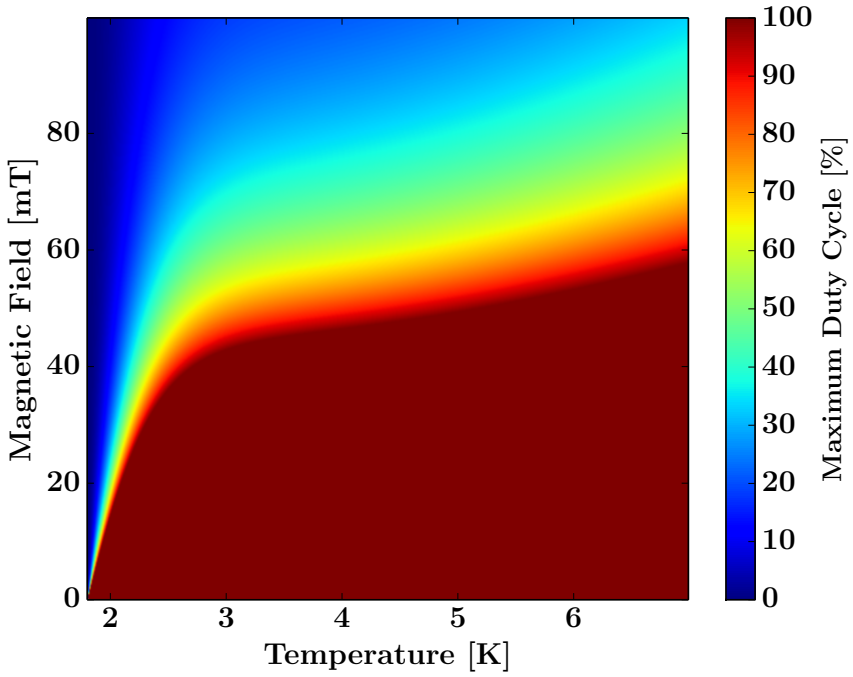

Figure B.9: Maximum duty cycle at which one can measure the surface resistance with the RF-DC compensation technique. A generic formula for the niobium surface resistance is taken from [4], a residual resistance of 3 nΩ is assumed.

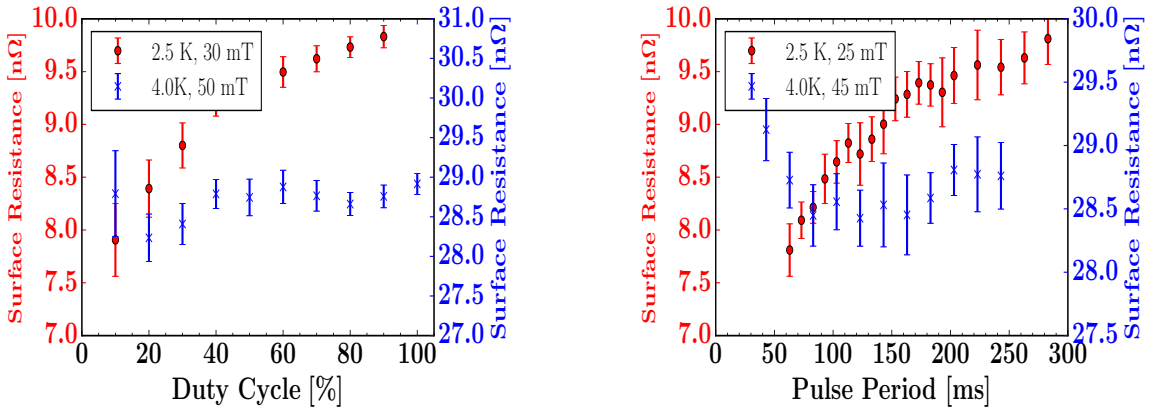

Figure B.10: Surface resistance measured at different duty cycles (left) and for different pulse periods (right). In both cases data was taken for low and high RF losses. For low losses (low temperature and field) a significant systematic error exists, underestimating the true surface resistance at low duty cycles and pulse periods

be found in [104].

In this chapter the measurement capabilities and limitations of the Quadrupole Resonator were studied. The measurement resolution of the system was found to be sufficient for all purposes. Measurement precision can be an issue at low fields. Several sources of

measurement bias were found. The RF power measurement and the uncertainty of the simulation constant give a systematic error of around 10%. Unwanted heating of the normal conducting surface adds several $n\Omega$ to the measured resistance and can thus be a significant error source for high quality samples. Measurement error can also be induced by a too low duty cycle or pulse period when measuring small RF losses.

Appendix C

Geophone

Geophones are devices used to measure low frequency mechanical oscillations. They are mainly used to measure seismic waves, but have also found application for microphonics measurements in RF cavities [70]. A schematic drawing of a geophone is shown in Figure C.1. The measurement principle relies on the relative movement of the coil and the iron yoke inducing a voltage which is subsequently measured. Following [72], we can set up the mechanical equation of the geophone, where we consider x to be the coordinate of the coil and that of the outer case, which is rigidly connected to the object of interest.

$$m\ddot{x} + c(\dot{x} - \dot{w}) + k(x - w) = 0 \tag{C.1}$$

where c is the damping cofficient and k is the spring constant. For the electrical equation we have:

$$L\frac{di}{dt} - T(\dot{x} - \dot{w}) + Ri = 0 \tag{C.2}$$

where $L\frac{di}{dt}$ is the self-inductance of the coil, and T is the coil constant, giving a measure for how much voltage is induced per relative velocity. We would like to calculate the response of this system to a harmonic oscillation $w = A\cos\omega t$ with arbitrary frequency ω. As this is rather difficult in time domain, we transpose both equations to the Laplace domain, using a new coordinate $y = x - w$. An introductory overview of Laplace transformations is given in [105].

$$ms^2Y(s) + csY + kY(s) = ms^2W(s) \tag{C.3}$$

For the electric equation we neglect the self-inductance term and end with:

$$-sTY(s) + RI(s) = 0 \tag{C.4}$$

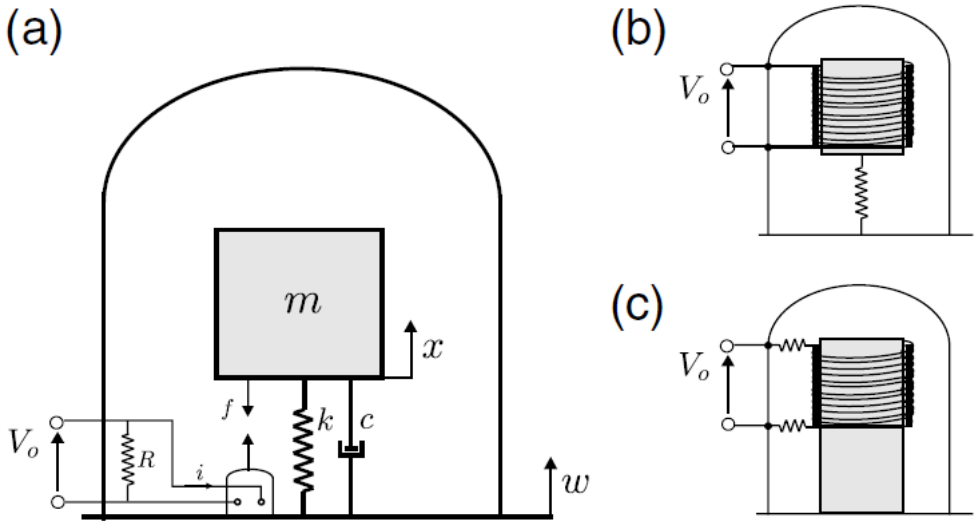

Figure C.1: Schematic drawing of a geophone. The yoke of mass m is connected to the outer casing with the spring constant k and damping coefficient c. Two possible realizations of the geophone are shown: Moving yoke (b) and moving coil topology (c). Figure taken from [72]

.

One can now define the transfer function of the geophone, which is given by the ratio of output signal to the input signal (in our case the $\dot{w}$.

Still in Laplace domain, we have:

$$\begin{aligned} G(s) = \frac{RI}{sW} &= -\frac{sTY}{{}^{s}/_{ms^2}(ms^2 + cs + k) \cdot Y} \\ &= \frac{-Ts^2}{s^2 + 2\zeta\omega_0 s + \omega_0^2} \end{aligned} \tag{C.5}$$

with the resonant frequency $\omega_0 = {}^{k}/_{m}$ and the damping coefficient $\zeta = {}^{c}/_{2m\omega_0}$. To calculate the response of the geophone to our input signal, we still need to transform it to the Laplace domain:

$$sW = \mathcal{L}\{-A \sin \omega t\} = -A\frac{s}{s^2 + \omega^2} \tag{C.6}$$

Our output signal is now simply:

$$U(s) = G(s) \cdot sW(s) = -AT \cdot \frac{s^2}{s^2 + 2\zeta\omega_0 s + \omega_0^2} \cdot \frac{s}{s^2 + \omega^2} \tag{C.7}$$

Equation C.7 can be transformed back to time domain by using a analytical computer code such as mathematica [106]:

$$u(t) = \mathcal{L}^{-1}\{U(s)\} = AT \cdot \frac{w^4 \cos \omega t - 2\zeta\omega_0\omega^3 \sin \omega t - \omega_0^2\omega^2 \cos \omega t}{w^4 + 4\zeta\omega_0^2\omega^2 + \omega_0^4} \tag{C.8}$$

The amplitude of this function was determined numerically as a function of frequency for a resonance frequency $f_0 = 10\,\text{Hz}$ and different values of ζ. The results are plotted in Figure C.2. For low damping, the sensitivity has a pronouced maximum around f_0 and falls of sharply towards lower frequencies. Above f_0, it approaches to a constant level, which is independent of ζ. Knowledge of the sensitivity of the geophone is necessary, as the measured data needs to be corrected for the different voltage signal response at different frequencies. The sensitivity curve of geophone used in section 7.1.2 is plotted in Figure C.3.

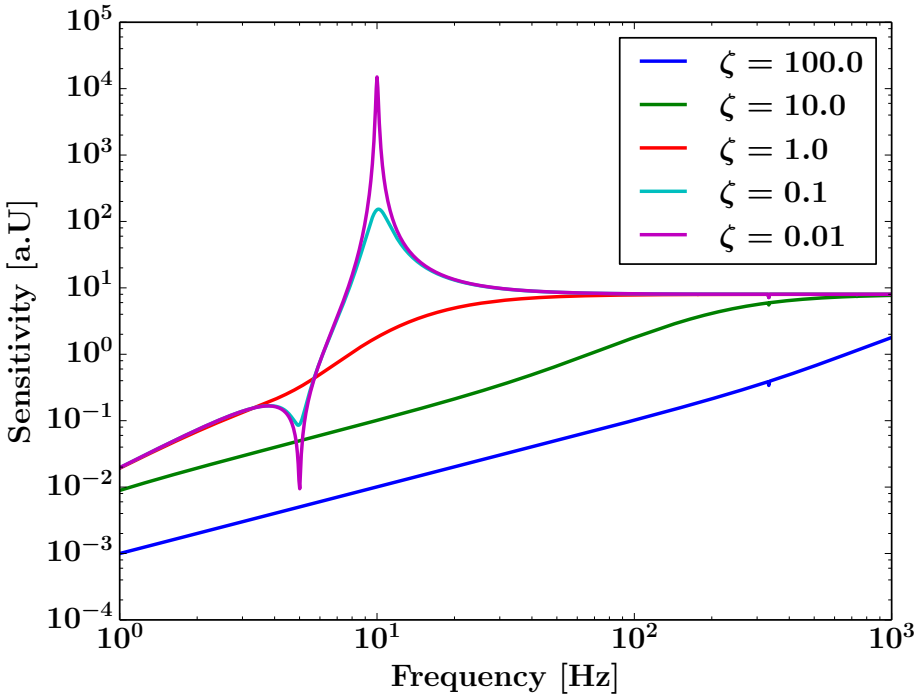

Figure C.2: Sensitivity of the model geophone, for $f_0 = 10\,\text{Hz}$ and different damping coefficients ζ.

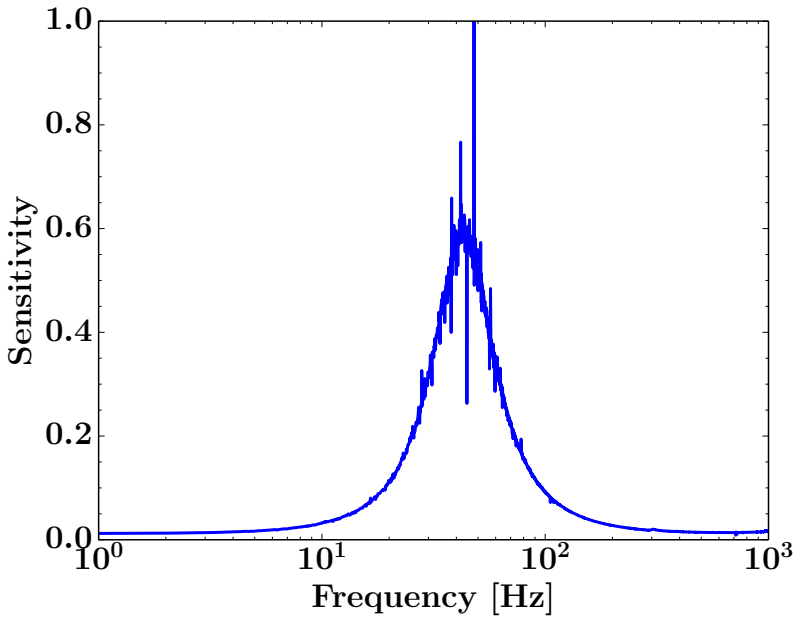

Figure C.3: Sensitivity curve of the geophone . The sensitivity is the response given by the geophone when excited with white noise (constant spectral power density)

Appendix D

Calculating the Power Dissipation for various Cavity Types

In Section 9.1, the approximation error for calculating the surface resistance from a constant quality factor was discussed. In this appendix, we show how to calculate the dissipated power (and thus the quality factor) for different cavity types.

D.1 Elliptical Cavities

Figure D.1 shows the profile of a half cell of a ERL low loss cavity. Next to the profile, the magnetic field, computed with SLANS, is plotted. Due to the cylindrical symmetry of a cavity, we can replace the surface integral in 9.3 with a line integral:

$$P_{Dis} = \frac{1}{2\mu_0^2} \int_{Surf} R_S(B)|B|^2 \cdot dA = \frac{1}{2\mu_0^2} \int_0^L R_S(B(z))|B(z)|^2 \cdot 2\pi r(z) dz \tag{D.1}$$

With this equation we can calculate the dissipated power in the cavity walls, for any arbitrary function of function $R_S(B)$. We can then use equation 9.2 , the computed surface field distribution $B(z)$ and the geometry factor, to extract $R_S^{meas}(B_{pk})$.

D.2 Half wave Resonator

For calculating the power dissipated in a half wave resonator (HWR), we consider a coaxial transmission line of length L, where the inner and outer conductor, of radii A and B are shorted at either ends. The frequency of such a HWR can easily be calcualted by: $L = \frac{\lambda}{2} = \frac{c}{2f}$. The magnetic field in such a structure is given by [107]:

$$H(r, \phi, z, t) = \frac{E_0 A}{4\pi r} \sin(\frac{\pi z}{L}) e^{i\omega t} \tag{D.2}$$

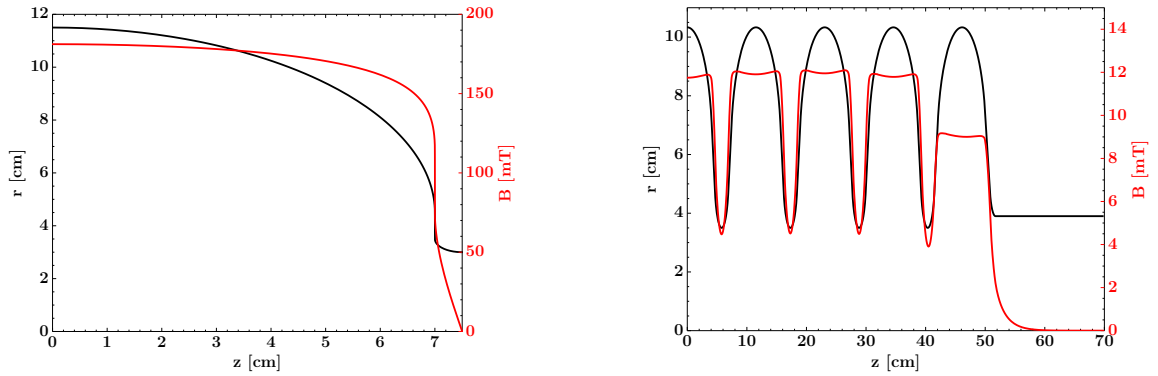

Figure D.1: Profile and surface magnetic field distribution for an ERL type single-cell and a TESLA nine cell

From Equation D.2, one can then calculate the stored energy to be:

$$\begin{aligned} U = \frac{1}{2}\mu_0 \int_V ||H||^2 dV &= \mu_0 \frac{E_0^2 A^2}{8\pi^2} \int_0^{2\pi} d\phi \int_{-L/2}^{L/2} dz \int_A^B \frac{dr}{r} sin^2(\frac{\pi z}{L}) \\ &= \frac{\mu_0 E_0^2 A^2 L}{8\pi} \log(\frac{B}{A}) \end{aligned} \tag{D.3}$$

where E_0 is an arbitrary field constant.The losses in the cavity walls can be calculated in a similar fashion, the expression for the geometry factor is given by:

$$G = \frac{2\omega U}{\int_S ||H||^2 dS} = \frac{\frac{\pi}{8} c\mu_0 \log(\frac{B}{A})}{L(\frac{1}{A} + \frac{1}{B}) + \log(\frac{B}{A})} \tag{D.4}$$

The peak magnetic field occurs at $z = \pm L/2$ and is related to the stored energy by:

$$\frac{B_{pk}}{\sqrt{U}} = \frac{\sqrt{\mu_0}}{A\sqrt{\pi L \log(\frac{B}{A})}} \tag{D.5}$$

With these equations, one can calculate the dissipated power in the coaxial structure for an arbitrary function $R_s(B)$ at a given peak magnetic field.

Bibliography

[1] The ATLAS Collaboration, "Observation of a new particle in the search for the standard model higgs boson with the ATLAS detector at the LHC," *Phys. Lett. B*, vol. 716, pp. 1–29, 2012.

[2] European XFEL Project Group, "The european X-Ray Free-Electron laser technical design report," tech. rep., DESY, 2007.

[3] K. Wille, *The Physics of Particle Accelerators*. Oxford University Press, 2000.

[4] H. Padamsee, J. Knobloch, and T. Hays, *RF Superconductivity for Acceleartors*. Wiley-VCH, 2008.

[5] B. Aune, R. Bandelmann, D. Bloess, B. Bonin, A. Bosotti, M. Champion, C. Crawford, G. Deppe, B. Dwersteg, D. A. Edwards, H. T. Edwards, M. Ferrario, M. Fouaidy, P.-D. Gall, A. Gamp, A. Gössel, J. Graber, D. Hubert, M. Hüning, M. Juillard, T. Junquera, H. Kaiser, G. Kreps, M. Kuchnir, R. Lange, M. Leenen, M. Liepe, L. Lilje, A. Matheisen, W.-D. Möller, A. Mosnier, H. Padamsee, C. Pagani, M. Pekeler, H.-B. Peters, O. Peters, D. Proch, K. Rehlich, D. Reschke, H. Safa, T. Schilcher, P. Schmüser, J. Sekutowicz, S. Simrock, W. Singer, M. Tigner, D. Trines, K. Twarowski, G. Weichert, J. Weisend, J. Wojtkiewicz, S. Wolff, and K. Zapfe, "Superconducting TESLA cavities," *Phys. Rev. ST Accel. Beams*, vol. 3, p. 092001, Sep 2000.

[6] M. Aicheler, "A Multi-TeV linear collider based on CLIC technology : CLIC conceptual design report," tech. rep., 2014.

[7] H. Podlech, "Superconducting versus normal conducting cavities," *CERN Yellow Report*, vol. 1, pp. 151–170, 2013.

[8] K. Onnes, "The resistance of pure mercury at helium temperatures," vol. 12, p. 120, 1911.

[9] C. Buzea and K. Robbie, "Assembling the puzzle of superconducting elements: A review," *Supercond. Sci. Technol.*, vol. 18, 2005.

[10] Coalition of the Commercial Application of Superconductors, "Superconductivity present and future applications," 2009.

[11] C. Gorter and H. Casimir, "The thermodynamics of the superconducting state," *Z. tech. Phys*, vol. 15, pp. 539–542, 1934.

[12] R. Casalbuoni, "Lecture notes on superconductivity: Condensed matter and QCD."

[13] J. Bardeen, L. N. Cooper, and J. R. Schrieffer, "Theory of superconductivity," *Phys. Rev.*, vol. 108, pp. 1175–1204, Dec 1957.

[14] R. F. Gasparovic and W. L. McLean, "Superconducting penetration depth of lead," *Phys. Rev. B*, vol. 2, pp. 2519–2526, 1970.

[15] J. Halbritter, "Comparison between measured and calculated RF losses in the superconducting state," *Zeitschrift fuer Physik*, vol. 238, pp. 466–476, 1970.

[16] P. Kneisel, "Effect of cavity vacuum on performance of superconducting niobium cavities," in *Proceedings of he 7th Workshop on RF Superconductivity, Gif-sur-Yvette, France*, 1995.

[17] J. Knobloch, *Advanced Thermometry Studies of Superconducting Radio-Frequency Cavities*. PhD thesis, Cornell University, 1997.

[18] B. Bonin and R. Roeth, "Q-degradation of niobium cavities due to hydrogen contamination," in *Proceedings of the 5th Workshop on RF Superconductivity*, 1991.

[19] C. Vallet, M. Bolore, B. Bonin, J. Charrier, B. Daillant, J. Gratadour, F. Koechlin, and S. H., "Flux trapping in superconducting cavities," in *Proceedings of the third European Particle Accelerator Conference, Berlin, Germany*, 1992.

[20] J.-M. Vogt, O. Kugeler, and J. Knobloch, "Impact of cool-down conditions at T_c on the superconducting RF cavity quality factor," *Phys. Rev. ST Accel. Beams*, vol. 16, p. 102002, Oct 2013.

[21] T. F. Stromberg, *The superconducting properties of high purity niobium*. PhD thesis, Iowa State University, 1965.

[22] A. Abrikosov, "Magnetic properties of superconductors of the second group," *Sov. Phys -JETP*, vol. 5, 1957.

[23] E. Brandt, "Electrodynamics of superconductors exposed to high frequency fields," 2009.

[24] C. Poole, H. Farach, R. Creswick, and R. Prozorov, *Superconductivity*. 2nd ed., 2007.

[25] T. Hays and H. Padamsee, "Measuring the RF critical field of Pb, Nb, and Nb3Sn," in *Proceedings of the 1997 Particle Accelerator Conference, Vancouver, Canada*, 1997.

[26] F. Furuta, K. Saito, T. Saeki, H. Inoue, Y. Morozumi, Y. Higashi, and T. Higo, "High reliable surface treatment recipe of high gradient single cell SRF cavities at KEK," in *Proceedings of the 13th International Conference on RF Superconductivity, Beijing, China*, 2007.

[27] C. P. Bean and J. D. Livingston, "Surface barrier in Type-II superconductors," *Phys. Rev. Lett.*, vol. 12, pp. 14–16, 1964.

[28] M. K. Transtrum, G. Catelani, and J. P. Sethna, "Superheating field of superconductors within Ginzburg-Landau theory," *Phys. Rev. B*, vol. 83, p. 094505, 2011.

[29] W. Singer, "SRF cavity fabrication and materials," *CERN Yellow Report*, vol. 005, pp. 171–207, 2014.

[30] S. Aderhold, S. Chel, E. Elsen, F. Eozenou, L. L., and R. D., "ILC higrade cavity process," tech. rep., DESY, 2010.

[31] A. Grassellino, A. Romanenko, D. Sergatskov, O. Melnychuk, Y. Trenikhina, A. Crawford, A. Rowe, M. Wong, T. Khabiboulline, and F. Barkov, "Nitrogen and argon doping of niobium for superconducting radio frequency cavities: a pathway to highly efficient accelerating structures," *Superconductor Science and Technology*, vol. 26, no. 10, p. 102001, 2013.

[32] P. P. Dhakal, G. Ciovati, P. Kneisel, and G. Myneni, "Enhancement in quality factor of SRF niobium cavities by material diffusion," *IEEE Transactions on Applied Superconductivity*, vol. 25, 2015.

[33] A. Gurevich, "Reduction of dissipative nonlinear conductivity of superconductors by static and microwave magnetic fields," *Phys. Rev. Lett.*, vol. 113, p. 087001, 2014.

[34] A. Sulimov, P. Borowiec, V. Gubarev, J. Iversen, D. Kostin, G. Kreps, K. Krzysik, A. Matheisen, W. D. Moeller, and D. Reschke, "First RF measurement results for the european XFEL SC cavity production," in *Proceedings of the 26th Linear Accelerator Conference, Tel-Aviv, Israel*, 2012.

[35] C. Benvenuti, B. P., D. Bloess, G. Cavallri, E. Chiaveri, N. Haebel, N. Hilleret, J. Tuckmantel, and W. Weingarten, "Superconducting niobium sputter-coated copper cavity modules for the LEP energy upgrade," in *Proceedings of the 14th IEEE Particle Accelerator Conference, San Francisco, USA*, 1991.

[36] D. Boussard, "Performance of the LEP2 SRF system," in *Proceedings of the 17th IEEE Particle Accelerator Conference, Vancouver, Canada*, 1997.

[37] A. Gurevich, "Enhancement of rf breakdown field of superconductors by multilayer coating," *Applied Physics Letters*, vol. 88, no. 1, 2006.

[38] M. Peiniger, M. Hein, N. Klein, G. Müller, H. Piel, and P. Thüns, "Work on Nb_3Sn cavities at wuppertal," in *Proceedings of the Third Workshop on RF Superconductivity, Argonne National Laboratory, USA*, 1987.

[39] S. Posen, M. Liepe, and D. L. Hall, "Proof-of-principle demonstration of Nb_3Sn superconducting radiofrequency cavities for high Q_0 applications," *Applied Physics Letters*, vol. 106, no. 8, pp. –, 2015.

[40] J. C. Loudon, S. Yazdi, T. Kasama, N. D. Zhigadlo, and J. Karpinski, "Measurement of the penetration depth and coherence length of MgB_2 in all directions using transmission electron microscopy," *Phys. Rev. B*, vol. 91, p. 054505, 2015.

[41] S. Posen, *Understanding and Overcoming Limitation Mechanisms in* Nb_3Sn *Superconducting RF Cavities*. PhD thesis, Cornell University, 2015.

[42] D. E. Oates, A. C. Anderson, C. C. Chin, J. S. Derov, G. Dresselhaus, and M. S. Dresselhaus, "Surface-impedance measurements of superconducting NbN films," *Phys. Rev. B*, vol. 43, pp. 7655–7663, 1991.

[43] A. Valente-Feliciano, "SRF materials other than niobium," in *Proceedings of the 13th International Conference on RF Superconductivity, Beijing, China*, 2007.

[44] A. Valente-Feliciano, J. Spradlin, G. Eremeev, C. E. Reece, M. Burton, and L. R.A., "Growth and characterization of multilayer NbTiN films," in *Proceedings of the 17th International Conference on RF Superconductivity, Whistler, Canada2015*, 2015.

[45] T. Tajima, L. Civale, D. Devlin, R. Schulze, I. Usuv, and G. Martinez, "Status of MgB2 coating studies for SRF applications," in *Proceedings of the 16th International Conference on RF Superconductivity, Paris, France*, 2013.

[46] D. Hall, M. Liepe, D. Gonella, and I. Madjarov, "SRF material performance studies using a sample host cavity," in *Proceedings of the 5th International Particle Accelerator Conference, Dresden, Germany*, 2014.

[47] J. Maniscalco, D. Hall, and M. Liepe, "RF performance studies of thin film superconductors using a sample host cavity," in *Proceedings of the 6th International Particle Accelerator Conference, Richmond, USA*, 2015.

[48] C. Baumier, C. Antoine, F. Fortuna, G. Martinet, and J. Villegier, "Multilayers activities at SACLY/ORSAY," in *Proceedings of the 16th International Conference on RF Superconductivity, Paris, France*, 2013.

[49] H. L. Phillips, G. Davis, J. Delayen, J. Ozelis, and H. Wang, "A sapphire loaded TE011 cavity for surface impedance measurement - design, construction and commissioning status," in *Proceedings of the 12th International Conference on RF Superconductivity, Cornell, USA*, 2005.

[50] B. P. Xiao, C. E. Reece, H. L. Phillips, R. L. Geng, H. Wang, F. Marhauser, and M. J. Kelley, "Note: Radio frequency surface impedance characterization system for superconducting samples at 7.5 GHz," *Rev. Sci. Instrum.*, vol. 82, p. 056104, 2011.

[51] P. Welander, M. Franzi, and S. Tantawi, "Cryogenic RF characterization of superconducting materials at SLAC with hemispherical cavities," in *Proceedings of the 17th International Conference on RF Superconductivity, Whistler, Canada*, 2015.

[52] J. Guo, S. Tantawi, D. Martin, and C. Yoneda, "Cryogenic RF material testing at SLAC," in *Proceedings of the 2011 Particle Accelerator Conference, New York, USA*, 2011.

[53] E. Haebel, E. Brigant, and E. Mahner, "The Quadrupole Resonator, design considerations and layout of a new instrument for the RF characterization of superconducting surface samples," in *Proceedings of the 6th European Particle Acceleartor Conference, Stockholm, Sweden*, 1998.

[54] T. Junginger, *Investigations of the Surface Resistance of Superconducting Materials*. PhD thesis, University of Heidelberg, 2012.

[55] S. Aull, "Sample testing with the Quadrupole Resonator," *Proceedings of the 5th International Workshop on "Thin films applied to Superconducting RF and new ideas for pushing the limits of RF Superconductivity", Newport News, USA*, 2012.

[56] CST - Computer Simulation Technology AG, "Microwave Studio," 2014.

[57] G. Sleijpen and H. Van der Vorst, "A Jacobi-Davidson iteration method for linear eigenvalue problems," *SIAM Rev.*, vol. 42, pp. 267–293, 2000.

[58] C. Boffo, C. Cooper, G. Galasso, and A. Rowe, "Optimization of BCP processing of elliptical nb SRF cavities," in *Proceedings of the 13th International Conference on RF Superconductivity, Beijing, China*, 2007.

[59] J. Knobloch, "The "q disease" in superconducting niobium rf cavities," *AIP Conference Proceedings*, vol. 671, no. 1, pp. 133–150, 2003, http://aip.scitation.org/doi/pdf/10.1063/1.1597364.

[60] J. Mammosser, T. Rothgeb, T. Wang, and A. T. Wu, "Investigation into the effectiveness of the JLab high pressure rinse system," in *Proceedings of the 2003 Particle Accelerator Conference, Portland, USA*, 2003.

[61] G. Ciovati, P. Kneisel, and G. Myneni, "Effect of low temperature baking on niobium cavities," in *Proceedings of the 11th International Conference on RF Superconductivity, Hamburg, Germany*, 2003.

[62] K. Kowalski, A. Bernasik, W. Singer, and J. Camra, "'In Situ' XPS investigation of the baking effect on the surface oxide structure formed on niobium sheets used for superconducting RF cavity production," in *Proceedings of the 11th International Conference on RF Superconductivity, Hamburg, Germany*, 2003.

[63] D. Ford, L. D. Cooley, and D. Seidman, "Suppression of hydride precipitates in niobium superconducting radio-frequency cavities," *Supercond. Sci. Technol.*, vol. 26, 2013.

[64] O. Kugeler, A. Neumann, W. Anders, and J. Knobloch, "Adapting TESLA technology for future cw light sources using HoBiCaT," *Review of Scientific Instruments*, vol. 81, no. 7, 2010.

[65] T. Powers, "Theory and practice of cavity RF test systems," in *U.S Particle Accelerator School 2011*, 2011.

[66] O. Melnychuk, A. Grassellino, and A. Romanenko, "Error analysis for intrinsic quality factor measurement in superconducting radio frequency resonators," *Review of Scientific Instruments*, vol. 85, no. 12, 2014.

[67] S. Keckert, "Optimizing a calorimetry chamber for the RF characterization of superconductors," Master's thesis, University Siegen, 2015.

[68] A. Neumann, *Compensating Microphonics in SRF Cavities to Ensure Beam Stability for Future Free-Electron-Lasers*. PhD thesis, Humboldt- Universitaet zu Berlin, 2008.

[69] J. Delayen, "Ponderomotive instabilities and microphonics," *Proceedings of the 12th International Workshop on RF Superconductivity, Cornell, USA*, 2005.

[70] A. Bertolini, "Vibration diagnostics instrinstrument for ILC," *Measurement Science and Technology*, 2007.

[71] E. Hudson, R. Simmonds, C. Yi Leon, S. Pan, and J. Davis, "A very low temperature vibration isolation system," *Czechoslovak Journal of Physics*, vol. 46, no. 5, pp. 2737–2738, 1996.

[72] C. Collette, S. Janssens, P. Ferandez-Carmona, K. Artoos, M. Guinchard, C. Hauviller, and A. Preumont, "Review: Intertial sensors for low-frequency seismic vibration measurement," *Bulletin of the Seismological Society of America*, 2012.

[73] R. H. Fowler and L. Nordheim, "Electron emission in intense electric fields," *Proceedings of the Royal Society London*, vol. A119, pp. 173–181, 1928.

[74] G. Eremeev and A. D. Palczewski, "Characterization of superconducting radiofrequency breakdown by two-mode excitation," *Journal of Applied Physics*, vol. 115, no. 2, 2014.

[75] R. Calder, G. Dominichini, and N. Hilleret, "Influence of various vacuum surface treatments on the secondary electron yield of niobium," *Nuclear Instruments and Methods in Physics Research Section B: Beam Interactions with Materials and Atoms*, vol. 13, no. 1, pp. 631 – 636, 1986.

[76] R. Parodi, "Multipacting," in *Proceedings of the CAS - CERN Accelerator School: RF for Accelerators, Ebeltoft, Denmark*, vol. 7, pp. 447–458, 2011.

[77] J. Turneaure and I. Weissman, "Microwave surface resistance of superconducting niobium," *J. Appl. Phys*, vol. 39, p. 4417, 1968.

[78] G. Ciovati, G. Myneni, F. Stevie, P. Maheshwari, and D. Griffis, "High field q slope and the baking effect: Review of recent experimental results and new data on nb heat treatments," *Phys. Rev. ST Accel. Beams*, vol. 13, p. 022002, Feb 2010.

[79] H. Thai, F. Mentre, N. Holford, C. Veyrat-Follet, and E. Comets, "A comparison of bootstrap approaches for estimating uncertainty of parameters in linear mixed-effect models," *Pharmaceutical Statistics*, vol. 12, pp. 129–40, 2013.

[80] S. Garbow, K. Hillstrom, and J. More, "Documentation for MINPACK subroutine LMDIF," tech. rep., Argonne National Laboratory, 1980.

[81] J. Slater, *Microwave Electroncs*. Van Nostrand, 1959.

[82] S. Aull, O. Kugeler, and J. Knobloch, "Trapped magnetic flux in superconducting niobium samples," *Phys. Rev. ST Accel. Beams*, vol. 15, p. 062001, Jun 2012.

[83] D. Gonnella, J. Kaufman, and M. Liepe, "Impact of nitrogen doping of niobium superconducting cavities on the sensitivity of surface resistance to trapped magnetic flux," *Journal of Applied Physics*, vol. 119, no. 7, 2016.

[84] A. Gurevich and G. Ciovati, "Effect of vortex hotspots on the radio-frequency surface resistance of superconductors," *Phys. Rev. B*, vol. 87, p. 054502, 2013.

[85] J.-M. Vogt, O. Kugeler, and J. Knobloch, "High-Q operation of superconducting rf cavities: Potential impact of thermocurrents on the rf surface resistance," *Phys. Rev. ST Accel. Beams*, vol. 18, p. 042001, 2015.

[86] J. Halbritter, "RF residual losses, high electric and magnetic RF fields in superconducting cavities," in *Proceedings of the 38th Workshop of the INFN Eloisatron Project, Erice, Italy*, pp. 59–79, 1999.

[87] J. Vines, Y. Xie, and H. Padamsee, "Systematic trends for the medium field q-slope," in *Proceedings of the 13th International Conference on RF Superconductivity, Beijing, China*, 2007.

[88] A. Romanenko, *Surface Characterization of Niobium Cavity sections - Understanding the High Field Q-Slope*. PhD thesis, Cornell University, 2009.

[89] B. Visentin, J. Charrier, and B. Coadou, "Improvement of superconducting cavity performance at high accelerating gradients," in *Proceedings of the 6th European Particle Accelerator Conference, Stockholm, Sweden*, 1998.

[90] P. Kneisel, "Preliminary experience with in-situ baking of niobium cavities," in *Proceedings of the 1999 Workshop on RF superconductivity, Santa Fe, USA*, 1999.

[91] M. Ge, F. Furuta, M. Liepe, and G. Hoffstaetter, "Field-dependent surface resistance of a superconducting RF cavity caused by surface impurity," *ArXiv e-prints*, July 2015, 1507.08704.

[92] T. Hanaguri, Y. Iino, M. Atsutaka, and T. Fukase, "Magnetic-field dependence of the london penetration in type-II supercondctor V_3Si," *Physica C*, vol. 246, pp. 223–227, 1994.

[93] J. P. Turneaure, J. Halbritter, and H. A. Schwettman, "The surface impedance of superconductors and normal conductors: The Mattis-Bardeen theory," *Journal of Superconductivity*, vol. 4, no. 5, pp. 341–355, 1991.

[94] D. C. Mattis and J. Bardeen, "Theory of the anomalous skin effect in normal and superconducting metals," *Phys. Rev.*, vol. 111, pp. 412–417, Jul 1958.

[95] R. Chambers, "The anomalous skin effect," *Proc. R. Soc. London*, vol. 215, no. 1123, pp. 481–497, 1952.

[96] A. Anthore, H. Pothier, and D. Esteve, "Density of states in a superconductor carrying a supercurrent," *Phys. Rev. Lett.*, vol. 90, no. 12, 2003.

[97] A. V. Timofeev, C. P. García, N. B. Kopnin, A. M. Savin, M. Meschke, F. Giazotto, and J. P. Pekola, "Recombination-limited energy relaxation in a Bardeen-Cooper-Schrieffer superconductor," *Phys. Rev. Lett.*, vol. 102, p. 017003, 2009.

[98] P. Dhakal, G. Ciovati, G. R. Myneni, K. E. Gray, N. Groll, P. Maheshwari, D. M. McRae, R. Pike, T. Proslier, F. Stevie, R. P. Walsh, Q. Yang, and J. Zasadzinzki, "Effect of high temperature heat treatments on the quality factor of a large-grain superconducting radio-frequency niobium cavity," *Phys. Rev. ST Accel. Beams*, vol. 16, p. 042001, Apr 2013.

[99] D. Pozar, *Microwave Engineering*. John Wiley & Sons, INC, 1998.

[100] H. London, "The high-frequency resistance of super tin," *Proc. R. Soc. London*, 1940.

[101] M. Merio, "Material properties for engineering analyses of srf cavities," tech. rep., Fermi National Accelerator Laboratory, 2011.

[102] Cryodata Inc., "HEPAK," 1998.

[103] R. Reed and A. Clark, *Materials at Low Temperatures*. Asm Intl, 1983.

[104] R. Kleindienst, A. Burrill, S. Keckert, J. Knobloch, and O. Kugeler, "Commissioning results of the HZB quadrupole resonator," in *Proceedings of the 17th International Conference on RF Superconductivity, Whistler, Canada*, 2015.

[105] A. La Rosa, "Transfer function and the Laplace transform," tech. rep., Portland State University, 2000.

[106] Wolfram Research, Inc., "Mathematica 8.0," 2010.

[107] J. Holzbauer, "Superconducting half wave resonator design and research," in *Proceedings of the U.S. Particle Accelerator School*, 2012.

List of Figures